

Characterisation of glacio-chemical and glacio-meteorological parameters of Amundsenisen, Dronning Maud Land, Antarctica

Fidan Göktas

**Ber. Polarforsch. Meeresforsch. 425 (2002)
ISSN 1618 - 3193**

Fidan Göktas
Alfred-Wegener-Institut
für Polar- und Meeresforschung
D-27568 Bremerhaven

*Dissertation, vorgelegt dem Fachbereich 5
(Geowissenschaften) der Universität Bremen zur Erlangung
des Grades eines Doktors der Naturwissenschaften (Dr. rer.
nat.) im März 2002.*

Contents

Zusammenfassung	5
Summary	7
1 Introduction	9
1.1 Site Selection	10
1.2 Objectives	12
2 Fundamentals	15
2.1 Characteristics of Antarctica	15
2.1.1 Geography	15
2.1.2 Meteorology	15
2.1.3 Glaciology	19
2.2 Nature of aerosol	20
2.2.1 Definition and classification	21
2.2.2 Genesis of aerosol	21
2.2.3 Transportation and deposition mechanisms	22
2.3 Source of aerosol and glacio-chemistry	25
2.4 Concluding remarks	26
3 Ion analyses in ice cores	29
3.1 Abstract	29
3.2 Introduction	30
3.3 Sampling	30
3.4 Analyses	33
3.4.1 Ion chromatography set up	33
3.4.2 Ion chromatography methods	35
3.4.3 Blank samples and blank values	36
3.4.4 Accuracy	37
3.5 Conclusions	41
3.6 Acknowledgements	41

4	Accumulation rates in Dronning Maud Land	43
4.1	Abstract	43
4.2	Introduction	44
4.3	Methods	44
4.3.1	Fieldwork	44
4.3.2	Dating the firn cores	46
4.4	Results and Discussion	52
4.4.1	Accumulation history during the last 700 years.	52
4.4.2	Spatial distribution of accumulation	53
4.4.3	Relationship between temperature and accumulation rates	57
4.4.4	Time series of accumulation rates and climate	58
4.5	Conclusions	60
4.6	Acknowledgements	61
5	High resolution chronology of earth's volcanic history	63
5.1	Abstract	63
5.2	Introduction	64
5.3	Methods	65
5.3.1	Site Selection, Sampling and Analyses	65
5.3.2	Identification of the volcanic signature	68
5.3.3	Calculation of volcanic H ₂ SO ₄ deposition	70
5.3.4	Comparison of peaks in nss-sulphate and DEP	71
5.4	Results and discussion	73
5.4.1	Spatial variability of two recent volcanic signals	73
5.4.2	Annual layer counting	76
5.4.3	Spatial variability of historic volcanic signals	77
5.4.4	Implications for snow accumulation rates and post - deposi- tional processes	83
5.5	Conclusions	87
5.6	Acknowledgements	87
6	Seasonal and Spatial Variation	89
6.1	Abstract	89
6.2	Introduction	90
6.3	Methods	91
6.3.1	Sampling	91
6.3.2	Analysis	93
6.3.3	Dating	95

6.4	Results and discussion	98
6.4.1	Seasonal variation	98
6.4.2	Spatial distribution	100
6.5	Conclusions	104
6.6	Acknowledgements	105
7	Impact of climate parameters on Amundsenisen	107
7.1	Abstract	107
7.2	Introduction	108
7.2.1	Source of biogenic sulphur	109
7.3	Methods	113
7.3.1	Site Selection, sampling, analyses and dating	113
7.3.2	Reanalysis Data	114
7.3.3	Analyses Methods	115
7.4	Results and discussion	117
7.4.1	Sample data	117
7.4.2	Inter-site correlation and spatio-temporal distribution	118
7.4.3	Single site, multiple component EOF analysis	119
7.4.4	Multiple site, single component EOF analysis	121
7.4.5	Potential effect of El Niño on ice core records	123
7.5	Conclusions	136
8	Conclusions and outlook	139
	Bibliography	143
	List of figures	157
	List of tables	160
	Appendix	161
	A Data	162
	B Spatio-temporal distribution of chemical species	167
	Danksagung	171

Zusammenfassung

In dieser Arbeit wurden anhand von aerosolchemischen Zeitreihen aus vier mitteltiefen Eiskernen und 21 Schneeschächten, welche die letzten zwei Jahrtausende überdecken, die glazio-chemischen und glazio-meteorologischen Parameter des Amundsenisen, Dronning Maud Land, Antarktis, untersucht.

Um dieses Ziel zu erreichen, wurden die Ionenkonzentrationen von Methansulphonsäure (MSA), Cl^- , Br^- , NO_3^- , SO_4^{2-} , Na^+ , NH_4^+ , K^+ , Mg^{2+} und Ca^{2+} bestimmt. Die für Br^- , NH_4^+ , K^+ , Mg^{2+} und Ca^{2+} detektierten Konzentrationen waren zu niedrig, um eine realistische Aussage machen zu können, wohingegen der relative Fehler aller anderen Komponenten bei etwa 5% lag.

In der saisonalen Variation von Seesalz zeigte sich ein Maximum im Spätwinter bzw. Frühjahr. Das saisonale Maximum der Komponenten MSA und Nicht-Seesalz-Sulphat konnte für das späte Frühjahr bzw. den späten Sommer detektiert werden, was auf die gleiche marin-biogene Quelle für beide Komponenten hinweist.

Von der räumlichen Verteilung der Seesalz-Komponenten, welche ein einheitliches Depositionsmuster aufweist, konnte auf einen homogenen Transport mariner Luftmassen auf das Plateau geschlossen werden.

Aufgrund post-depositionärer Effekte war es nicht möglich, einen Transport- oder Depositionsmechanismus für MSA bzw. Nitrat zu definieren. Sulphat zeigte ein inverses Verhalten zur Akkumulationsrate. Dies impliziert, dass 75% des deponierten Sulphates auf trockene Deposition zurückzuführen ist.

Auch im Falle der Akkumulationsraten konnte eine einheitliche räumliche Verteilung festgestellt werden. Ein Anstieg der Akkumulationsrate für das 20. Jahrhundert, welcher den Wert, der für den Beginn des 19. Jahrhunderts beobachtet worden ist, nicht übersteigt, ist höchstwahrscheinlich mit natürlichen Temperaturvariationen in Verbindung zu bringen. Für den Zeitraum vor 1000 A.D. konnten an DML07 post-depositionäre Effekte, die mit hoher Wahrscheinlichkeit auf Windverfrachtung zurückzuführen sind, beobachtet werden. Aus diesem Grund wurde das Abzählen der Jahresschichten im Falle von DML07 erschwert. Im Gegensatz dazu konnte für DML05 eine akkurate stratigraphische Datierung über die ganze Kernlänge hinweg durchgeführt werden, wobei die letzten zwei Jahrtausende überdeckt wurden.

Basierend auf den Daten, die aus der Analyse von 13 Schneeschächten hervorgegangen sind, konnte eine räumlich einheitlich verteilte H_2SO_4 -Deposition von $13.4 \pm 3.5 \text{ kg km}^{-2}$ für die Eruption des Pinatubo/Cerro Hudson-Komplexes abgeleitet werden. Diese räumlich einheitliche vulkanische Deposition konnte zur Synchronisation aller Eiskern-Zeitreihen über die letzten 2000 Jahre verwendet werden. Aus der Kombination des letztgenannten Resultates mit dem Abzählen von Jahresschichten konnte eine einzigartige Vulkanchronologie mit einer verbesserten Datierungsgenauigkeit von ± 1 Jahr im oberen Teil bzw. ± 22 Jahren für die ältesten Abschnitte des Eises, abgeleitet werden.

Aus geringen Kreuz-Korrelationskoeffizienten der Ionenzeitreihen ging hervor, dass die Varianz von lokal- oder regionalskaligen Prozessen dominiert wird. Mit Hilfe von EOF-Analysen konnte gezeigt werden, dass der Beitrag aller Probenorte zur Varianz der Komponenten von ähnlichem Wert ist. Aus der Korrelation von principal component 1 (PC1), der zeitlichen Entwicklung der empirisch orthogonalen Funktion 1 (EOF1), des Nicht-Seesalz-Sulphates mit der Oberflächentemperatur des Wassers, welche durch das El Niño-Phänomen beeinflusst ist, konnte der Süd-Atlantische Ozean als Quellgebiet für biogenes Sulphat, das auf dem Amundsenisen deponiert worden ist, bestimmt werden. Dies bedeutet, dass eine zwar geringe jedoch dennoch signifikante Signatur des El Niño-Phänomens in den Eiskernen gefunden werden konnte. Wavelet- und Kohärenzanalysen von PC1 des Nicht-Seesalz-Sulphates zeigten signifikante Perioden von 2.1, 3.3 und 4.3 Jahren, welche ebenfalls für El Niño-Ereignisse beobachtet worden sind.

Summary

This work investigates the glacio-chemical and glacio-meteorological parameters on Amundsenisen, Dronning Maud Land, Antarctica, using aerosol chemistry records from four intermediate deep ice cores and 21 snow pits, covering the past two millennia.

To this end ion concentrations for methanesulfonate (MSA), Cl^- , Br^- , NO_3^- , SO_4^{2-} , Na^+ , NH_4^+ , K^+ , Mg^{2+} and Ca^{2+} were determined. The concentrations of Br^- , NH_4^+ , K^+ , Mg^{2+} and Ca^{2+} were too low to be reliably determined, while the relative error of all other components was on the order of 5%.

The seasonal variation for sea-salt showed a maximum in late winter/spring. The seasonal maximum of the components MSA and nss-sulphate was found in late spring/summer, indicating the same marine biogenic source for both components.

The spatial distribution of the sea-salt components showed an uniform deposition pattern, indicating homogeneous transport of marine air masses onto the plateau. No transport or deposition mechanism could be determined for MSA and nitrate due to post-depositional effects. Sulphate showed an inverse relationship to accumulation rate, implying that 75% of the deposited sulphate can be accounted for by dry deposition.

An uniform spatial distribution pattern was also observed for the accumulation rates. An increase in accumulation rate for the 20th century does not exceed values in the beginning of the 19th century and is most probably linked to natural temperature variations. Post-depositional effects most probably due to wind scouring were observed at DML07 prior to 1000 A.D. While this impeded annual layer counting at DML07, accurate stratigraphic dating could be performed for the whole record at DML05, covering the last two millennia.

Based on data from 13 snow pits, a spatially uniform volcanic H_2SO_4 deposition of $13.4 \pm 3.5 \text{ kg km}^{-2}$ was derived for the recent Pinatubo/Cerro Hudson eruption complex. The spatially uniform volcanic deposition could be used to synchronize all ice core records over the last 2000 years. In combination with the annual layer counting an unique volcano chronology with improved dating accuracy from ± 1 at the top up to ± 22 for the oldest parts of the ice core records could be derived.

Cross-correlation of the ion records showed low coefficients, indicating that processes on local or regional scale dominate the variance. EOF analyses revealed that the contribution of all sampling sites to the variance of the components is of similar size. The correlation of PC1, associated to EOF1, of nss-sulphate and sea-surface temperature, which is influenced by the El Niño phenomenon, points to the Southern Atlantic Ocean as the source region for biogenic sulphur deposited onto Amundsenisen. Therefore, a very small but nevertheless significant signature of the El Niño phenomenon was found in the ice core records. Wavelet and coherence analysis of PC1 of nss-sulphate showed significant periods of 2.1, 3.3 and 4.3 years, which are also observed for El Niño events.

Chapter 1

Introduction

Climate has effected the evolutionary and cultural development of mankind. It is one of the most important forces which determines the wealth and poverty, stability and variability of individuals and societies. Therefore, humanity has put a lot of effort into knowing how the climate system works and how it might develop. In the main focus of the scientific discussion of climate is temperature change and its entailed sea level change, in particular the role of the vast ice sheets at polar sites [Herterich, 1993]. However, the global climate system is inherently complex, variable, and poorly understood. Data of the present and past climate are necessary to understand its mechanisms, though the data are limited in both spatial and temporal domains.

Instrumental observations provide data of the recent climate. Data about the past can be found in several natural archives - sea and lake sediments, tree rings, peat bogs, corals and also in glacier ice [Stauffer, 1999]. These archives help to understand the processes and interactions of the atmosphere, hydrosphere, lithosphere, biosphere and cryosphere [Barry and Chorley, 1992]. The advantage of the icy archive of the cryosphere lies in its capability to provide information about past climate changes as well as about atmosphere composition and circulation.

Most of the frozen water on the world is stored in the polar ice caps of Antarctica (90%) and Greenland (7%). Antarctica is located far from the other continents and around the geographical South Pole. It is surrounded by the Southern Ocean, a stretch of water unbroken by land for some 20,000 km (at 56°S), which characteristic is the Antarctic Circumpolar Convergence with water temperature close to freezing. The atmosphere's most prominent feature is the Antarctic Vortex with a drop of temperature that results in dramatic changes of weather and biology at the meeting of warm and cold water and air masses. This combination of large oceanographic and meteorological changes contributes to the strong cyclo-genesis. Storm systems tend to move southwards onto the ice sheet, and bring warm and humid air masses onto

the Antarctic Plateau effecting energy balance, moisture, and aerosol concentration.

Direct observational and instrumental records are limited to short periods in time and small areas of Antarctica. A continuous instrumental record of air temperature from the south polar region only exists from 1903 at Islas Orcadas [Jones and Limbert, 2001], but this location is on the fringe of Antarctica at 44° 44' W and 60° 44'S. Continuous instrumental observations on the Antarctic continent began during the International Geophysical Year (1957-58), and remain relatively sparse spatially especially when compared to records from more temperate regions of the world.

The combination of the geographical and meteorological attributes and remarkably limited human activities gives Antarctica an important and complex role in the global climate system. It is expected to have the cleanest atmosphere in the world [Legrand and Mayewski, 1997]. Therefore, for studying the role of background aerosols from the bio-geochemical cycle, Antarctica provides an attractive site free from anthropogenic pollution. This valuable information source can be explored by drilling ice cores. A multitude of climate parameters can be studied from ice cores, for example atmospheric trace gases, atmospheric aerosol composition and temperature.

1.1 Site Selection

Valuable information covering a full glacial - interglacial cycle have already been obtained from Antarctica and Greenland. The cores GRIP and GISP2 from Greenland have provided data over the last 250,000 years in high resolution [Dansgaard et al., 1993; Yiou et al., 1997]. Although several ice cores from Antarctica are available (Figure 1.1), studies of the vast East Antarctic plateau have so far been limited to a single deep ice core obtained at Vostok and to a recent drilling project undertaken by a Japanese group at Dome Fuji.

In the framework of the European Project for Ice Coring in Antarctica (EPICA), a joint European Science Foundation/European Union programme in which ten European countries* cooperate, two deep ice core drillings are being carried out. The cores are drilled at Dome Concordia (Dome C) [Wolff et al., 1999] and in the plateau area of Dronning Maud Land (DML), Amundsenisen [Oerter et al., 2000].

Dome C is located on a topographic dome, where horizontal movement of the ice is thought to be negligible and thus, distortions in the layering is expected to be minimal. Furthermore, the deep ice core is expected to reach about 500 000 years

*Belgium, Denmark, France, Germany, Italy, the Netherlands, Norway, Sweden, Switzerland and the United Kingdom

back in time with the accumulation rate of about $36 \text{ kg m}^{-2} \text{ a}^{-1}$ [Petit et al., 1982] and ice thickness at this location of about 3250 m [Tabacco et al., 1998].

The deep ice core from DML will not reach back 500 000 years, but will provide a climate record in a higher resolution. Furthermore, the area of Dome C is expected to be dominantly influenced by air masses originating from the Indian Ocean, where Dronning Maud Land is expected to be dominantly influenced by air masses originating in the Atlantic Ocean. The Atlantic Ocean is considered to be an important link between the Antarctic and Greenland climate records [Stocker, 1998; Stocker, 2000].

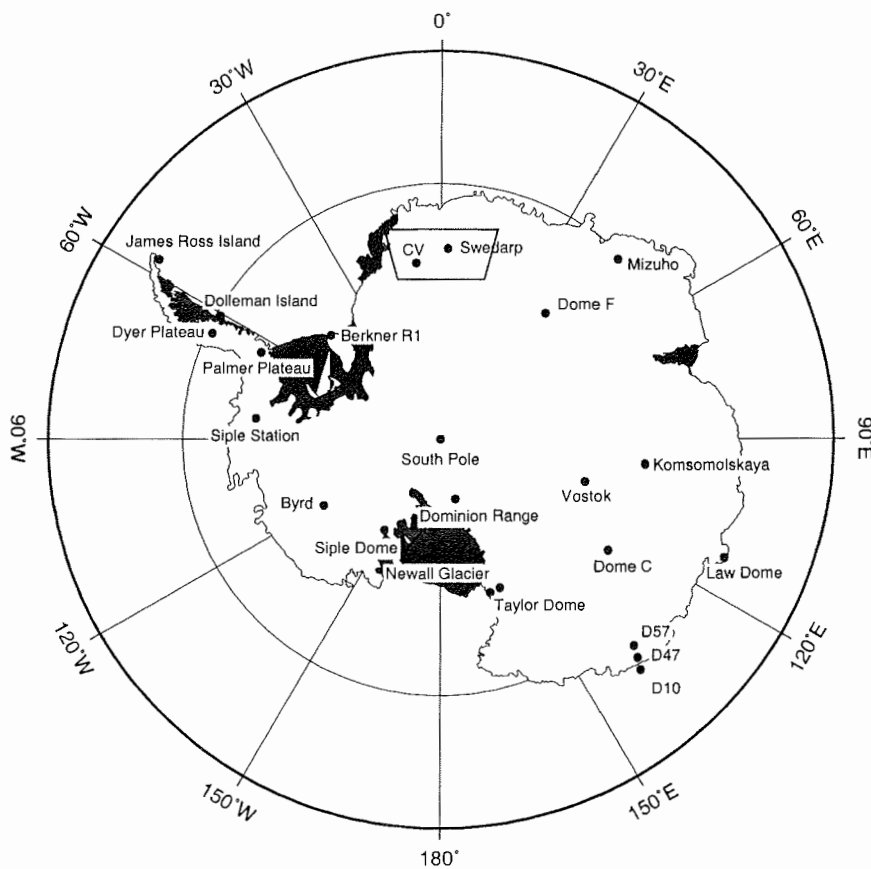


Figure 1.1: Map of Antarctica.

Map of Antarctica showing locations of the most important ice cores. The solid line marks the area under investigation in Dronning Maud Land (DML), Amundsenisen.

These distinctive features of the deep ice cores from DML can help to determine whether some results of earlier ice core studies (GRIP and GISP2) have a global sig-

nificance or whether they are confined chiefly to the Northern Hemisphere. Finally, it could help to solve the principle question of how far global climate is coupled between the two hemispheres.

To find a suitable drilling site for that deep ice core several pre-site surveys were carried out in the field campaigns 1997/1998 and 1999/2000 in DML (Figure 1.2). In this work data from snow pits and intermediate deep ice cores are presented.

Airborne radio-echo sounding [Steinhage, 2000] and accumulation rate studies [Oerter et al., 2000] in Dronning Maud Land have shown that the best location for a deep drilling site in Amundsenisen is at 2 km east of DML05. Therefore, the present deep drilling on Amundsenisen is carried out at $0^{\circ}04.07' E$ and $75^{\circ}00.10' S$. The deep ice core from this site is expected to cover one interglacial-glacial cycle.

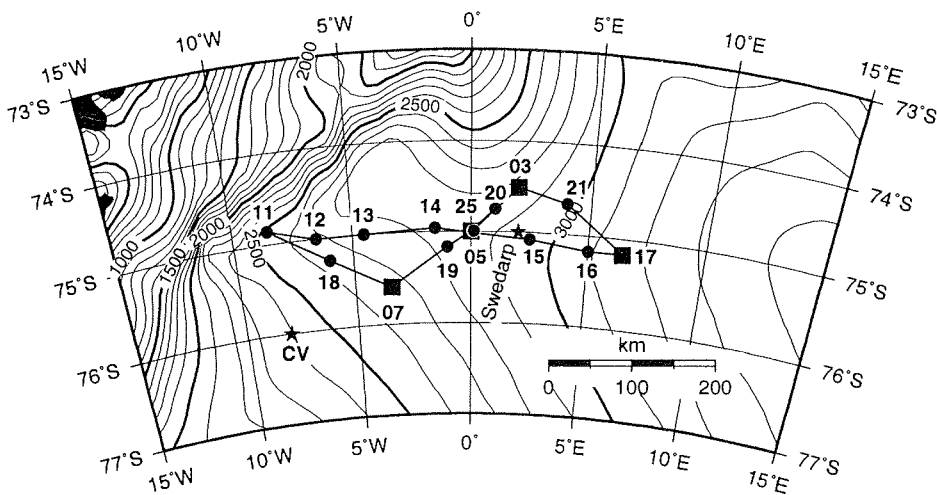


Figure 1.2: EPICA-DML pre-site survey.

Expanded view of Amundsenisen, the plateau area of DML. The traverse line of the pre-site survey and sampling locations are shown. Circles mark locations of snow pits, squares of intermediate deep ice cores, and stars of ice cores at Camp Victoria (CV) [Karlöf et al., 2000] and Swedarp [Isaksson, 1994]. The present deep drilling site is close to DML05, at $0^{\circ}04.07' E$, $75^{\circ}00.10' S$.

1.2 Objectives

This work focuses on the ionic composition of atmospheric aerosol (MSA , Cl^- , Br^- , NO_3^- , SO_4^{2-} , Na^+ , NH_4^+ , K^+ , Mg^{2+} , Ca^{2+}), which is incorporated in the deposited snow, firn and ice. The atmospheric transport pathways, circulation patterns, sea-

sonal timing, sources of ions, and climatic impact on bio-geochemical cycles can be deduced from the ionic composition of the accumulated snow, e.g. sampled in Greenland [Fischer, 1997] and Antarctica [Minikin et al., 1994].

The ionic composition of the snow and ice samples was analysed for all shown sampling sites in Figure 1.2. This work addresses the following questions:

- How should a contamination-free working environment for ice core sample processing be established ?
- How reliable is the icy archive in respect to the ionic components?
- Is there a significant spatial variation at the local or regional scale?
- Will the deep ice core be representative for the whole area under investigation?
- Can seasonal variations of the ionic composition be revealed?
- Can ice cores from DML be dated accurately?
- What are the regional atmospheric circulation patterns relevant for the aerosol transport onto DML?
- Can information about changes in source of aerosol (e.g. marine bio-productivity, storm activity) be derived?
- Can impact of El Niño phenomenon be detected on the ice core records?

Chapter 2 provides background information about the atmospheric, meteorological and glaciological parameters of Antarctica and DML in particular and about the composition, origin, transport, deposition and source of the aerosol. Chapter 3 to Chapter 6 are based on either submitted, accepted or printed publications.

Chapter 3 is a part of a publication, which presents the different analyses methods applied at laboratories around the world and is submitted to Journal of Chromatography. It presents the established working environment to process ice core samples, the handling, sampling and analyses procedure to study the ionic composition of samples from snow pits and ice cores.

Chapter 4 have been published by Oerter et al. [2000]. The accumulation rate pattern over the area under investigation is discussed in this part.

Chapter 5 is submitted to Journal of Geophysical Research. This chapter presents the results of studies on the volcanic history and glacio-chemical implication as revealed in firn and ice cores of DML.

In **Chapter 6** is in press in *Annals of Glaciology* No. 35. [Göktaş et al., 2002]. In this chapter the results on spatial and seasonal variation of the ionic species are discussed.

Chapter 7 is in preparation for publication. The variance in the signal of the ionic components, periodicities, and the impact of climate parameters, like sea surface temperature on the ice core records are discussed.

Chapter 2

Fundamentals

2.1 Characteristics of Antarctica

2.1.1 Geography

Antarctica, including ice shelf areas, encompasses an area of about 13.9 million km² (Figure 2.1) [Drewry et al., 1982], approximately one and a half time the size of Europe. During winter, sea ice develops and in September covers about 22 million km² [SCAR, 2002], which extends the total ice coverage to more than 30 million km². By comparison, a lesser sea ice extent is possible in the Northern Hemisphere, where more continents are located. The mean altitude of East Antarctica is about 2630 m [Drewry et al., 1982] and the maximum known ice thickness of 4776 m was observed in East Antarctica (at Terre Adelie 69°54'S and 135°12'E) [SCAR, 2002].

The area of Dronning Maud Land includes the whole region from the ice shelf areas, e.g. Ekströmisen, to the part of the Antarctic Plateau called Amundsenisen. The plateau region is divided sharply by the mountain ranges Heimefrontfjella and Kirvanveggen from the other areas (Figure 2.2).

The area under investigation on Amundsenisen, DML, is located between 10°W to 10°E and 76°S to 74°S (Figure 1.2). The altitude range is between 2500 m (DML11) and 3160 m (DML17) [Oerter et al., 1999]. The ice thickness varies between 1200 m (DML11) to more than 3100 m (DML07) with an ice thickness of approximately 2750 m at the present deep drilling site adjacent to DML05 [Steinhage, 2000]. In Figure 2.2 cross sections of surface altitude in along 0° E and 75° S are presented in altitude profiles.

2.1.2 Meteorology

Instrumental data records from Antarctica are limited both spatially and temporally. Data from past decades exist mainly from over-winter stations. Most of them are

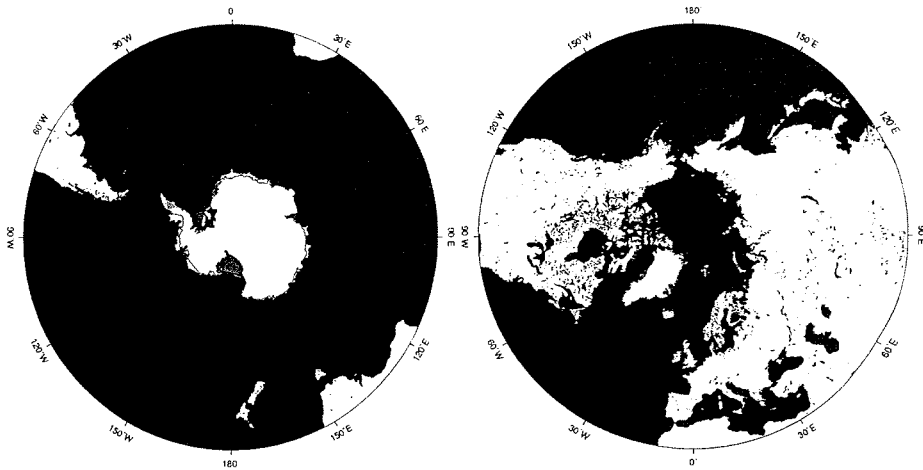


Figure 2.1: Map from the poles to latitude of 30° .

Maps of the Southern and Northern Hemisphere from latitude of 90° to 30° .

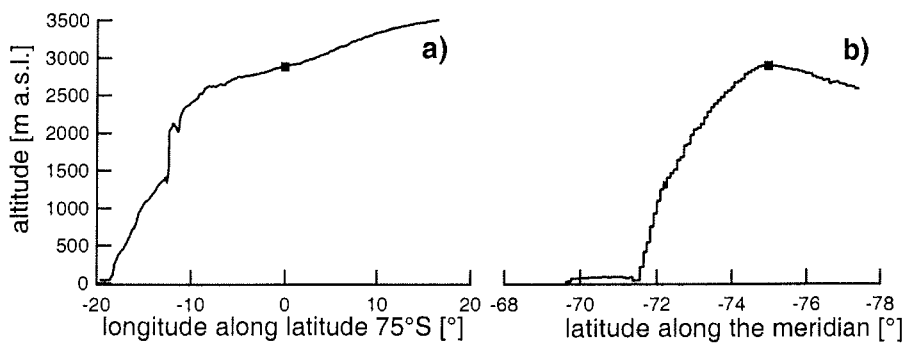


Figure 2.2: Cross sections of the surface altitude in DML.

Cross sections of the DML surface altitude taken at a) latitude of $75^\circ S$ and b) longitude of $0^\circ E$. The square marks the position of DML05.

located at coastal sites, except for South Pole and Vostok station, which provide data of long duration from the Antarctic Plateau. Recently automatic weather stations (AWS) have been installed on the Antarctic Plateau [Allison et al., 1993; Takahashi et al., 1998; Reijmer and van den Broeke, 2001b]. Considering Antarctica is one and a half times the size of Europe, an intensified data collection effort is crucial to understand the meteorology of Antarctica, in particular the temperature distribution and atmospheric circulation patterns.

In December 1997 the University of Utrecht installed three AWS (AWS8, AWS9 and AWS3) on Amundsenisen, Dronning Maud Land [Reijmer and van den Broeke, 2001b], shown in Figure 2.3. The AWS9 is located directly at DML05, 2 km west of the present deep drilling site. The mean annual temperatures for the time period January 1998 to December 2000 recorded at AWS3 is -48.25°C , at AWS8 -37.9°C and at AWS9 -46.1°C (see temperature record from AWS9 in Figure 2.4) [Reijmer and van den Broeke, 2001b]. The next section briefly outlines some of the unique meteorological conditions of Antarctica which are relevant for this study.

- TEMPERATURE

Antarctica is isolated from the Southern Hemispheric circulation by the Antarctic Vortex in the atmosphere and the Antarctic Circumpolar Current in the ocean. The boundary of these phenomena is where air as well as water temperatures drop significantly over a short distance.

On the continent itself there is a drastic difference in temperature. While the mean temperature at coastal sites like at Neumayer Station is -16.1°C [König-Langlo et al., 1998], on the Antarctic Plateau at DML05 the mean temperature, from January 1997 to December 2000, is -46.1°C [Reijmer and van den Broeke, 2001b]. The lowest temperature of -89.2°C was recorded on the Antarctic Plateau at Vostok Station [SCAR, 2002], which is lower than in any other area on the Earth.

- ATMOSPHERIC CIRCULATION

Antarctica is surrounded by a zone of sub-polar lows and strong westerlies. This zone plays an important role in the transfer of energy into Antarctica through cyclo-genesis. Due to the warmer temperature in the north these weather systems are inclined to move on the temperature gradient pole-ward. On the average a polar high is centred on the East Antarctic Plateau, but is disturbed by the described strong cyclo-genesis, which transport marine air masses onto the Antarctic Plateau. The key factor in the penetration of warm and humid air masses and cyclones into the Antarctic interior is the

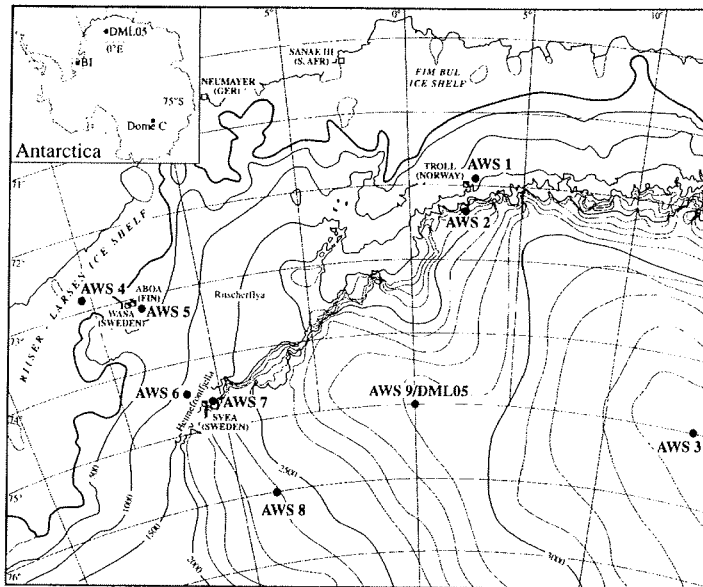


Figure 2.3: Location of automatic weather stations (AWS) on Dronning Maud Land. The AWS9 is located directly at the studied ice core at DML05, and 2 km west of the present deep drilling site in Amundsenisen. Figure is taken from Reijmer and van den Broeke [2001b].

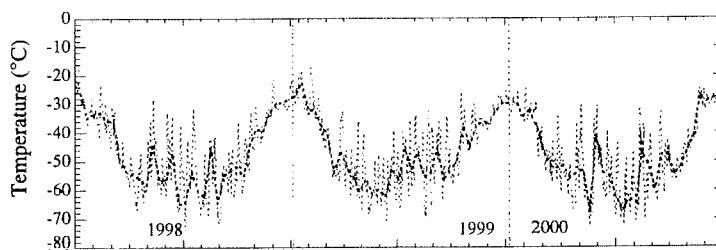


Figure 2.4: Temperature at DML05.

Temperature record from January 1998 until December 2000 at DML05 by the AWS9 [Reijmer and van den Broeke, 2001b]. Mean temperature over the three years at DML05 is -46.13°C [Reijmer and van den Broeke, 2001b].

establishment of warm upper level pressure ridges by strong advection of these humid air masses with anomalously warm temperatures and increased wind velocities [Reijmer and van den Broeke, 2001b].

On Dronning Maud Land average wind speeds vary between 3.7 m/s (AWS3), 5.1 m/s (AWS8) and 4.5 m/s (AWS9). During the advection of the warm and humid air-masses the wind speed increases to 15 m/s as observed by the AWS9 at DML05 [Reijmer et al., 2001c].

These singular events "reach" wind velocities close to the speed of katabatic wind systems. Katabatic winds form in the vicinity of the mountain ranges, when dense cold air-masses flow downhill under the influence of gravity. Katabatic winds were observed close to the mountain ranges of DML but not on the plateau area [Broeke et al., 1999]. All sampled snow pits and intermediate deep ice cores are located mainly on Amundsenisen, the plateau area of DML. In the area under investigation covered by the studies of Broeke et al. [1999], no katabatic winds were observed. Therefore, change in the net accumulation rate due to katabatic winds is not expected, but the net accumulation rate could be effected by the singular storm events.

2.1.3 Glaciology

The imbalance between accumulation rate and ablation rate determines whether an ice sheet builds up or not. As long as more snow is deposited on the ice sheet than the amount lost by calving of icebergs, melting or sublimation the ice sheet will exist.

In the case of Antarctica this glaciation process started 40 million years ago [Schäfer et al., 1999] and led to ice thicknesses of more than 4700 m [SCAR, 2002]. The consecutive precipitation events of individual snow and ice layers are preserved in the ice sheet and open the possibility to investigate this stratified ice archive. To get the climatic history it is necessary to assign an age to a layer, which is not possible if layers are missing, mixed or folded.

Ice domes or summits are locations on the ice sheet where horizontal movement of the snow/ice layers are negligible. Therefore, snow transformed into ice and recovered at these sites originate from the surface of the drill location. Under certain conditions other locations on ice divides can be used as sampling sites where low horizontal ice flow occurs. In this case upstream effects have to be considered. The sampled snow is expected to be deposited in not too wide a vicinity if meteorological conditions and accumulation patterns did not change between deposition and the

recovery.

Over Antarctica precipitation occurs only in the form of snow fall and as clear sky precipitation [Bromwich, 1988]. Accumulation includes all processes contributing to an increase of the mass of the ice sheet. These processes are precipitation, sublimation and transportation of snow by wind drift [Paterson, 1998]. As observed by AWS9 at DML05, accumulation on Amundsenisen is dominated by a few major events (Figure 2.5) [Reijmer et al., 2001c].

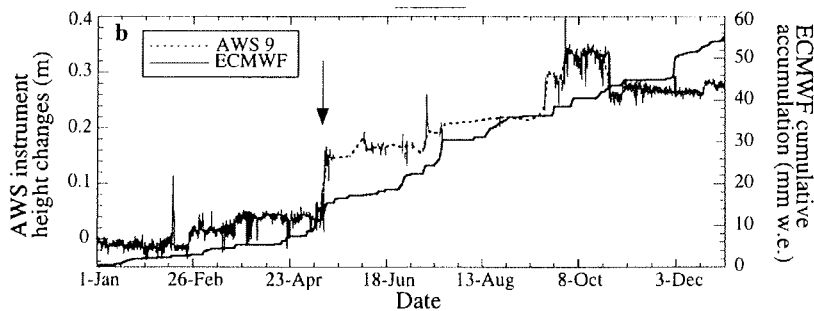


Figure 2.5: Accumulation record from AWS9.

Snow accumulation record recorded by AWS9 [Reijmer and van den Broeke, 2001b] at DML05 in year 1998. The accumulation occurred discontinuously, here in four major events. A special event depositing 10 cm of snow on 12th of May 1998 is marked by an arrow. (Figure is taken from Reijmer and van den Broeke [2001b].)

2.2 Nature of aerosol

Aerosols are one of the main climate-relevant components of the atmosphere. Natural and man-made sources inject aerosols into the atmosphere. In general, they are produced in the low and mid latitudes. The Antarctic continent is a negligible source of aerosols, due to its 99.6% snow and ice coverage [Huybrechts et al., 2000].

The global atmospheric circulation carries the aerosols also to the higher latitudes, where they are deposited on the ice sheets. Determined by geographical and meteorological conditions of the polar sites a unique glacio-chemical archive builds up and allows investigation of the aerosol composition of the past.

2.2.1 Definition and classification

The atmosphere consists of gases, liquid and/or solid particles. But only 0.1% of the atmospheric molecules are mutable and control many important atmospheric processes [Graedel and Crutzen, 1994]. Atmospheric aerosol, referred as aerosol hereafter, is defined as a disperse system containing solid and/or liquid particles suspended in gas [Jaenicke and Schütz, 1988]. It is customary to include in the definition of aerosol all solid and liquid particles except hydro meteors e.g. clouds and raindrops.

The aerosol is classified into the three following categories, depending on the radius r_p of the aerosol particles [Jaenicke and Schütz, 1988]:

Aitken Particles: $10^{-3} \leq r_p < 10^{-1} \mu\text{m}$

Large Particles: $10^{-1} \leq r_p \leq 1 \mu\text{m}$

Giant Particles: $1 \mu\text{m} \leq r_p$

2.2.2 Genesis of aerosol

Aerosol particles are not only emitted directly by natural and man-made sources, but are also formed by physical and chemical reactions in the atmosphere itself [Jaenicke and Schütz, 1988]:

A) Gas-to-particle conversion

Aerosol particles result from condensation or oxidation of gases by homogeneous nucleation or by heterogeneous condensation. An increase of the size of the aerosols occurs in both processes.

- **HOMOGENEOUS NUCLEATION:** By gas phase chemical reaction, new volatile gases are generated which may condense in an over-saturated atmosphere to aerosol particles. In general, these aerosols are of the size of Aitken Particles. An example for homogeneous nucleation is the reaction of SO_3 and H_2O to sulphate aerosol.
- **HETEROGENEOUS CONDENSATION:** Pre-existing aerosols are altered by impact or diffusion of a particle or molecule, or by oxidation. The aerosol size is increased by this process. An example for heterogeneous nucleation is the oxidation of SO_2 to H_2SO_4 by H_2O_2 dissolved on existing aerosol.

B) Bulk-to-particle conversion

In comparison to gas-to-particle conversion bulk-to-particle conversion leads to a decrease in particle size.

- **BUBBLE BURSTING AND TEARING OF WAVE CRESTS BY WIND:** Considering that approximately 70% of the Earth's surface is covered by sea water, dispersion of sea water is a major source for atmospheric aerosol. Wind force associated with wave formation and breaking generates bubble bursting and tearing of waves crests [Guelle et al., 2001]. Bubble bursting is believed to produce film and jet droplets at the sea surface. They are of the size of Large Particles. Tearing of wave crests by wind forms spume droplets, which are of larger size than film and jet droplets. Depending on the ambient humidity, these droplets can evaporate, leaving behind sea-salt aerosol.
- **GRINDING, IMPACTION OR OTHER COMMINUTION PROCESSES:** Dust and mineral particles from continental and soil surfaces are comminuted by physical and chemical processes, so that suspension in the air is possible.

2.2.3 Transportation and deposition mechanisms

In general, atmospheric aerosol is injected into the troposphere, where it spreads out horizontally within the global troposphere. A schematic overview of aerosol transport on the Antarctic continent is given in Figure 2.6. The aerosols are advected to Antarctica by global atmospheric circulation patterns, referred to as large-scale eddy transport, or by stratospheric transport, referred to as global transport [Ito, 1995].

Particles from the mid latitudes of the Southern Hemisphere can reach Antarctica via the free troposphere by strong cyclo-genesis, as mentioned in Section 2.1.2. In this way mainly sea-salt and biogenic sulphur are transported to Antarctica, due to the geographical conditions (Figure 2.1).

Additionally, emissions of strong plinian volcanic eruptions from anywhere on Earth can reach into the stratosphere. Within the stratosphere, they are globally distributed and deposited on the Antarctic ice sheet. Thus, the ice sheet archives information about these volcanic eruptions. Other ionic species, like sea-salt, are expected to have higher contribution to the ionic composition of the ice. This is due to a great stretch of water surrounding Antarctica, which forms an important and large source of marine background aerosols (Figure 2.1).

Ice covers 99.6% of the surface of Antarctica, rocks are exposed only in an area of 128 000 km² [Huybrechts et al., 2000]. Thus, the Antarctic continent itself should not have a significant contribution to mineral dust content in the ice cores from central Antarctica. Therefore, no significant contribution to mineral dust content

in the ice cores from Central Antarctica is expected from the Antarctic continent itself. Furthermore, Antarctica is located far away from other continental sites, which ensures low concentration of mineral dust in samples from the Antarctic Plateau for the recent time period [Genthon, 1992].

Due to the geographic location and icy conditions of Antarctica human activity is limited to individual research stations. In contrary, industrial activity occurs on continents primarily concentrated in the Northern than in the Southern Hemisphere. Thus, sources of anthropogenic emissions are located far from Antarctica and are thought to have a low contribution to the ionic composition of Antarctic ice cores. As a consequence, Greenland is more effected by man-made and continental sources [Fischer and Wagenbach, 1998a] than Antarctica [Isaksson, 1994].

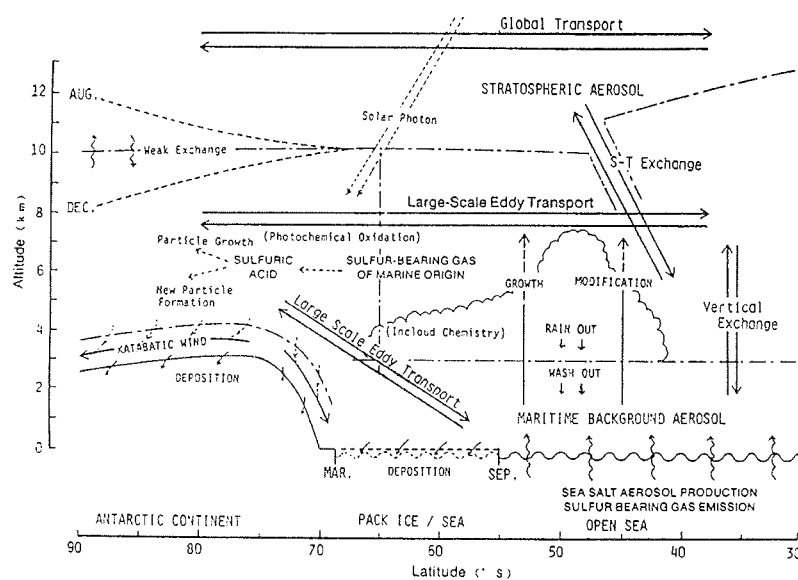


Figure 2.6: Aerosol transport mechanisms to Antarctica.

Global transport and large-scale eddy transport are the relevant mechanisms of aerosol transport to Antarctica, simplified from Ito [1995].

Deposition of atmospheric aerosol on the Antarctic Plateau can occur reversibly for volatile species bound at aerosol particles, e.g. gases like HCl and HNO_3 , and irreversibly for non volatile particles like H_2SO_4 and mineral dust [Davidson et al., 1996]. Deposition associated with precipitation is called wet deposition, and without precipitation dry deposition [Davidson et al., 1996]:

A) Wet deposition

Liquid droplets, ice crystals, raindrops and snow flakes are cloud components. Of these, rain drops and snow flakes are big enough to settle out of a cloud. The other two components tend to remain suspended in the cloud. In Central Antarctica precipitation occurs only in form of snow flakes or ice crystals [Bromwich, 1988]. Wet deposition is characterised by in-cloud process like the nucleation of particles as condensation or ice nuclei (rain out), and by below-cloud process, where particles and gases are removed from the atmosphere (wash-out) [Davidson et al., 1996]:

- **RAIN-OUT PROCESS:** This process is characterised by particle removal by activation as cloud condensation nuclei or by incorporation in already existing cloud droplets.
- **WASH-OUT PROCESS:** Particles and gases get either impacted into the viscous sub layer around a cloud droplet or ice particles or they are collected by falling snowflakes.

B) Dry deposition

Dry deposition occurs continuously compared to the more sporadically wet deposition. According to present knowledge deposition processes are assumed to occur in the following three major steps [Davidson et al., 1996]:

- **AERODYNAMIC TRANSPORT:** Particles and gases are transported by the wind system from the atmosphere down to a layer placed directly over the snow surface. This layer is called viscous sub-layer. For snow the viscous sub-layer is likely to extend a few millimetres or less over the surface.
- **BOUNDARY LAYER TRANSPORT:** The principle mechanism of transport from the viscous sub-layer onto the snow layer occurs for particles by diffusion, interception, impaction and turbulent inertial deposition. Gases are deposited on the snow layer by dissolution of gases within the quasi-liquid-layer and thus, adsorption onto the surface of snow and ice crystals.
- **INTERACTION WITH THE SURFACE:** No general mechanism of this process can be given. Particles and gases experience chemical and physical forces with the surface and are either retrained or released back to the air. For instance, a particle can return to the atmosphere after penetrating the viscous sub-layer or even the snow layer or a soluble gas may dissolve into the liquid layer of an ice crystal and re-evaporate back to the atmosphere.

2.3 Source of aerosol and glacio-chemistry

In respect of today's knowledge atmospheric aerosol is classified into anthropogenic, continental, maritime and background aerosol [Jaenicke and Schütz, 1988]. Each class is characterised by a specific ionic composition. Thus, from the ionic composition one can draw conclusions about the source of the transported aerosol, and about climate-relevant events as storms, marine biogenic and volcanic activity, industrial emissions, biomass burning, etc. [Legrand and Mayewski, 1997].

- **MINERAL DUST:** Erosion of the Earth's surface generates mineral particles. They consist of largely insoluble components like aluminium and iron, but also of partly soluble components like calcium, magnesium, potassium and sodium. Previous studies revealed that the concentration of these ionic species are high during the glacial and low during the interglacial periods [De Angelis et al., 1997]. This can be explained by more exposed continental shelf areas and more uptake of continental and soil particles due to higher wind velocities during glacial periods than interglacial periods. Furthermore, increased concentration of these mineral species can indicate colder time periods of shorter time scales, like the "Little Ice Age" [Kreutz et al., 1997]. Wind speed is also the driving force emitting mineral particles into the atmosphere [Jaenicke and Schütz, 1988].
- **SEA-SALT:** The sea-salt aerosol is generated by wind force over the ocean surface [Jaenicke and Schütz, 1988]. The main sea-salt components chloride and sodium are expected to be a proxy-parameter for storm activity over oceans. Recent studies discuss frost flowers, which are produced during sea ice formation, as an important alternative source for sea-salt aerosol [Rankin et al., 2000], but other studies showed no significant correlation between the sea ice cycle and sea-salt aerosol concentration, e.g. by Wagenbach et al. Wagenbach et al.. Thus, the role of the sea ice extent on sea-salt aerosol concentrations is still a matter of debate.
- **BIOGENIC SULPHUR:** The main biogenic component emitted from algae into the atmosphere is dimethyl-sulphide (DMS), which is oxidised in the atmosphere to methane sulphonate (MSA) and sulphate [Saltzman, 1995]. Whereas the oxidation of DMS is the only source for MSA, for sulphate other sources must be considered.
- **VOLCANOES:** Volcanoes emit large particles (volcanic debris), gases (SO_2 , CO_2 , HF, NO) as well as aerosols [Friend et al., 1982] into the upper tropo-

sphere and stratosphere. In the atmosphere some of the gases (e.g. SO_2) are transformed to aerosols by gas-to-particle-conversion. Large (plinian) eruptions inject these aerosols into the air where they are advected around the globe. The transport time for volcanic aerosols to polar regions is about 1-2 years and depends heavily upon the geographical location of the volcano and the particular dispersion by winds at the time of the eruption [Robock, 2000]. These aerosols of volcanic origin stay in the atmosphere for several years during which time they can significantly alter the radiative balance and albedo of the Earth's atmospheric system [Legrand and Wagenbach, 1999; McCormick et al., 1995; Rampino and Self, 1982; Menon et al., 2002].

The volcanic fallout from those plinian eruptions is preserved in polar ice, where it could be connected to peaks in the electrical property and ionic composition of the ice [Hammer, 1977; Bluth et al., 1993; Legrand and Mayewski, 1997].

- **ANTHROPOGENIC SOURCES:** Man-made aerosols result chiefly from fossil fuel combustion. Besides emitted particles like soot, gases such as SO_2 and NO which are important aerosol precursors, are also injected into the atmosphere [Rohde, 1999; Legrand and Mayewski, 1997].

Effects of man-made aerosol on the atmospheric aerosol composition have been observed at several regions on the Earth, e.g. in Greenland in form of a strong increase in the sulphate concentration since the beginning of the past century [Fischer and Wagenbach, 1998b]. Recent man-made emissions of gaseous sulphur compounds are two to three times larger than those of natural sources [Rohde, 1999]. Up to now, no anthropogenic influence on atmospheric aerosol composition in Antarctica has been observed [Isaksson, 1994; Kirchner and Delmas, 1988].

2.4 Concluding remarks

The geographical, meteorological and glaciological conditions of Antarctica ensure that the Antarctic ice sheet provides an unique archive for climate studies. Sites with low accumulation rates archive around 420 000 years of Earth's climate history [Petit et al., 1999]. Sampling sites with higher accumulation rates cover shorter time period, but enable to study a climate archive in higher resolution [Oerter et al., 1999; Sommer et al., 2000b; Oerter et al., 2000].

The recent atmospheric composition of Antarctica is not effected by anthro-

pogenic emissions [Kirchner and Delmas, 1988; Isaksson, 1994]. Therefore, it still provides the possibility to study the "natural background" of the atmosphere and the interaction between climate and the global bio-geochemistry. By contrast, the composition of the atmospheric aerosol of Greenland is effected since the beginning of the 20th century in its sulphur and nitrogen budget [Fischer and Wagenbach, 1998b].

Amundsenisen is attributed with a homogeneous temperature pattern. The area under investigation is thought not to be significantly effected by katabatic winds as shown by Broeke [2000], and therefore, to provide an unaltered net accumulation rate of the deposited snow and ice crystals. The Atlantic Ocean is expected to be the dominant source for the marine air masses transported onto DML. This provides a link to the ice cores from Greenland and gives the opportunity to study the coupling of the Northern and Southern Hemispheres.

Chapter 3

Ion analyses in ice cores

3.1 Abstract

Natural ice contains soluble impurities. These are from natural or man-made sources, e.g. the ocean, continental sites, anthropogenic emissions or volcanic eruptions. By global atmospheric transport mechanisms these solid or liquid aerosols are transported to the polar regions and deposited on the ice sheets, building an unique archive about the Earth's climate history, which can be recovered by drilling ice cores.

These ice core samples have to be processed in interannual resolution to be able to date the ice core. However, the amount of those soluble impurities in snow and ice samples from the Central Antarctic Plateau are partly lower than in distilled water, which requires clean handling, processing, and analysis conditions.

A contamination-free working environment using an electro-mechanical plane was established. For the analyses, the baseline noise could be limited to $0.0001 \mu\text{S}$, minimising the detection limit to 0.04 ng g^{-1} . Thus, 1 ng g^{-1} of ion species like MSA could be easily detected. The contamination during handling, from sampling until analytical measurements, could be performed with a relative error for the median ion concentration values of about 3%.

This chapter is a part of a submitted publication, which compiles methods for ion analyses in ice cores applied in several laboratories: University of Tasmania, Antarctic CRC and Australian Antarctic Division, British Antarctic Survey, University of Copenhagen, Stockholm University, Paul Scherrer Institute of Switzerland, University of Florence and University of Lapland. This chapter is submitted as the contribution: Göktaş, F., T. Bluszc and R. Weller (submitted). Ion analyses in ice cores: current techniques at the glaciology/air chemistry laboratory of the Alfred Wegener Institute, Germany. *Journal of Ion Chromatography*.

3.2 Introduction

Ionic species such as, MSA, Cl^- , NO_3^- , SO_4^{2-} , Na^+ , NH_4^+ , K^+ , Mg^{2+} , and Ca^{2+} , are incorporated in polar ice. These ions provide useful information about processes in the climate system. To extract this information of the ionic composition from very low concentration samples of snow and ice contamination free handling conditions of the samples are necessary. In this work the sampling procedure and ion chromatography (IC) analysis on snow pit and ice core samples from pre-site surveys, carried out in the frame of the European Project for Ice Coring in Antarctica (EPICA) in 1997/1998 and 1999/2000, are presented.

In comparison to snow pit samples, which are directly filled into pre-cleaned poly-ethylene (PE) beakers, the ice core samples must be processed under clean-room conditions to avoid contamination. For some ion species, the airborne background concentrations of gases and particles are high enough to contaminate the ionic composition of the samples with ammonium, calcium, potassium or chloride. By handling the samples in clean benches (type US class 100) contamination can be avoided. These benches were used in this study. In addition, during handling procedure PE-gloves were worn over the woollen gloves.

For de-contamination of ice core samples various techniques were used [Fischer, 1997; Cole-Dai et al., 1995; Langway et al., 1974]. We established a de-contamination routine using an electro-mechanical plane to de-contaminate ice core samples using the technique described by Fischer [1997]. The ionic composition of the snow pit and ice core samples was analysed using standard ion chromatography. All ion concentrations are given in $\text{ng}_{\text{component}}/\text{g}_{\text{ice}}$ corresponding to the mixing ratios.

3.3 Sampling

Snow pit and ice core samples were collected during several pre-site surveys on Amundsenisen, Dronning Maud Land, Antarctica. The snow pit samples were filled in PE-beakers and the ice cores shrink-wrapped in PE-bags. All samples were transported in frozen condition to the cold laboratory facility of the Alfred Wegener Institute in Bremerhaven, Germany.

Snow pit sampling

The beakers, with a volume of 60 ml, were rinsed with ultra-pure water ($\rho > 18 \text{ M}\Omega \text{ cm}$) until the electrical conductivity of the water in the beakers was less than $0.5 \mu\text{S}/\text{cm}$. The beakers were dried in a vacuum oven with high efficiency par-

ticle filter (HEPA) on the venting valve to avoid contamination. The beakers were sealed in PE-bags for transportation. All snow pits except snow pit SS9908 were sampled by pushing PE-beakers into the snow pit wall. The beakers were placed slightly overlapping the same part of the wall to avoid gaps in sampling. For snow pit SS9908 snow in 2 cm increments was collected into pre-cleaned 250 ml PE-beakers using a pre-cleaned spatula. All beakers were closed carefully and sealed in PE-bags.

Ice core sampling

The ice cores were drilled with a electro-mechanical drill and sealed in PE-bags, which were shrink-wrapped immediately in the field. The PE-bags for the ice cores were not pre-cleaned, because the ice cores were subsequently de-contaminated during the core processing in our cold laboratory.

The ice core samples were thoroughly de-contaminated under clean-room conditions in the cold laboratory using a contamination free electro-mechanical plane Figure 3.1, as described by Fischer [1997]. For the processing table a poly-carbonate (PC or POM) was used, because it does not emit chloride or other species of interest, and can withstand the low temperatures in the laboratory (-25°C). PC is suitable down to -120°C , while other synthetic material, e.g. poly-acryl, is brittle at temperatures lower than 0°C .

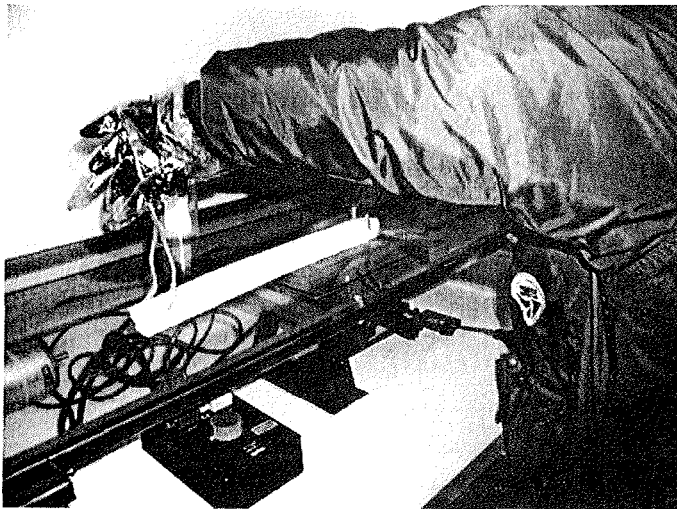


Figure 3.1: Cold laboratory set up.

De-contamination routine set up in the AWI cold laboratory facility. The electro-mechanical plane was placed in a clean bench and its rotational speed can be adjusted to the density of firn and ice.

The beams and the screws on the plane were made of high-grade stainless steel (Figure 3.1). Where it was not possible to use screws, the resin "Acrifix 192" was used as kit, a emission-free mixture of acryl-polymers with methyl-methacrylate.

For the ion analyses the centre part of the ice core was used, as shown in Figure 3.2. The other parts of the ice core were used for archive material, isotope measurements, texture and fabric studies etc. The used part of the ice core was split into high and low resolution samples. The whole white coloured part of Figure 3.2 was dedicated for high resolution samples to verify measurements done with other techniques and for comparison with meteorological data, e.g. NCEP reanalysis data, over the last 50 years in seasonal resolution. Low resolution samples (vertically striped part) were employed to reconstruct the long-term records in annual resolution.

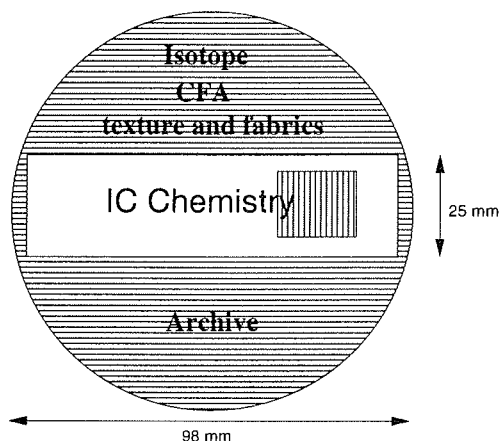


Figure 3.2: Core cutting scheme.

The white coloured centre part of the core was used for high resolution samples, and the part with vertical pattern for low resolution samples. Remaining parts (horizontal lines) were used for other analyses, e.g. CFA, or as archive material.

At least 3 mm of all surfaces of the samples were removed in the de-contamination process. In general, the de-contamination was performed by the electro-mechanical plane, except for the first 3 meters, where samples were too fragile to be held by the steel pair of tongs (Figure 3.1). Those samples were de-contaminated with a pre-cleaned ceramic knife.

The de-contaminated ice core samples were packed in pre-cleaned PE-bags, which were rinsed with ultra-pure water ($\sigma > 18 \text{ M}\Omega \text{ cm}$) until the electrical conductivity of the water inside was less than $0.5 \mu\text{S}/\text{cm}$. To check contamination during handling, ultra-pure water samples (called process blanks hereafter) were prepared, frozen and

processed like the ice cores in the processing routine.

The contamination during the ion chromatographic measurements was checked by filling pre-cleaned IC vials with ultra pure water. These vials were then treated like vials containing melted samples.

The snow pit samples were melted directly in the PE-beakers and the ice core samples in the PE-bags. Volumes of 2 ml of each sample were transferred by a graduated pipette into the IC vials under a clean bench (type US class 100) and subsequently analysed for anion and cation composition.

3.4 Analyses

All snow pit and all high resolution core samples were analysed for the major ions MSA, Cl^- , Br^- , NO_3^- , SO_4^{2-} , Na^+ , NH_4^+ , K^+ , Mg^{2+} , and Ca^{2+} . The low resolution ice core samples were measured only for anions, because for those the sodium concentrations taken from continuous flow analyses (CFA) performed by the University of Bern [Sommer et al., 2000b]. The concentrations of the other cations were so low, that they could not be used for interpretation. Reasons for this are given in detail in Section 3.4.4.

3.4.1 Ion chromatography set up

Standard ion chromatography was used to perform the analyses. This method is described in detail in the literature [Weiss, 1985] and will be discussed here only for the performed modifications (a schematic plot of the IC setup is shown in Figure 3.3).

A Dionex 500 ion chromatograph was used to perform anion and cation analyses. The High Performance Ion Chromatography (HPIC) is based on separation of the species by ion exchange between a mobile and a stationary phase. For that, ultra pure water was pumped into the eluent generation chamber (EG40). This module mixes the pumped water with the pure eluent in the chamber to the requested eluent concentration. Eluent concentrations between 0 and 100 mM can be generated. Potassium-hydroxide (KOH) eluent is used for anion and methane sulphonate (MSA) for cation analyses. Due to different retention time on the column for each ion species, the individual ion peaks reach the conductivity cell at specific retention times (one after the other). The retention time difference is determined by the eluent concentration, which can be adjusted using a known test solution. The separation is highly dependent on the eluent and the column material used. In this case a Dionex AS12 column was used for anion and a Dionex CS11 for cation analyses.

To detect low response signals in the presence of the high concentration eluent

it is necessary to reduce the background conductivity of the HPIC. Several methods are offered [DIONEX, 1997], whereas the auto-suppression mode has been applied in the AWI laboratory for the past 6 years for anion and cation analysis. In this commonly used mode, the solution passes the suppressor on the way from the column to the conductivity cell. The suppressor removes efficiently the eluting ion in the eluent solution and decreases the background conductivity [DIONEX, 1997]. To increase the signal to noise ratio an external water supply for the suppression unit is introduced.

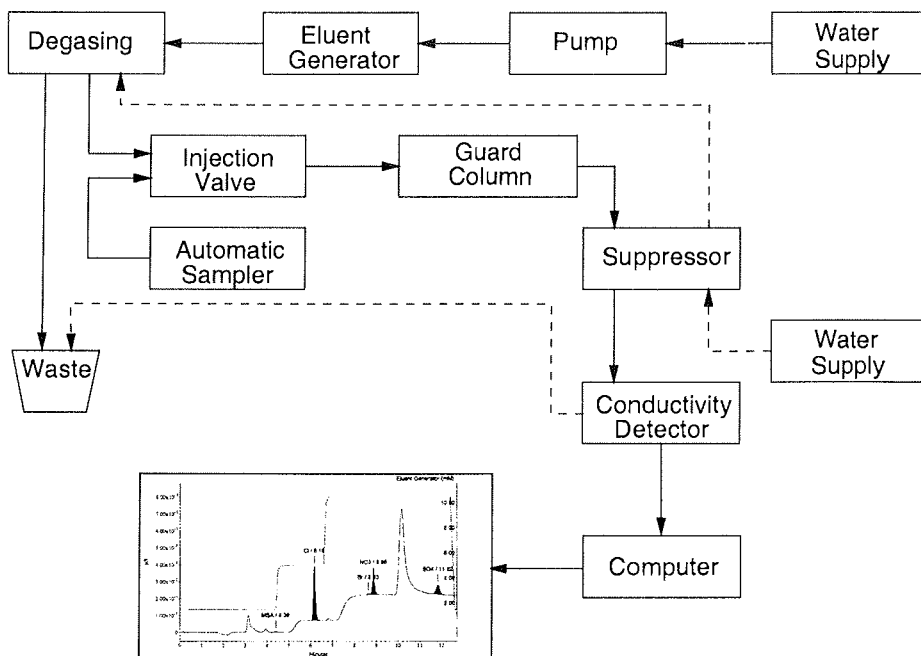


Figure 3.3: Setup for IC measurement.

A schematic plot of the HPIC set up. The samples are injected by an automatic sampler into the system. The dashed lines mark the modification of the previous system.

3.4.2 Ion chromatography methods

The analyses of the anions were performed by a gradient method (Figure 3.4). This means that the concentration of the eluent is not constant over time. As mentioned before, each ion is characterised by its certain retention time for the specific column. The use of a gradient method allows shortening of the measurement time without degrading the analytical resolution. Typically, the anion analyses lasted between 15 and 25 minutes, depending on the wear of the used column.

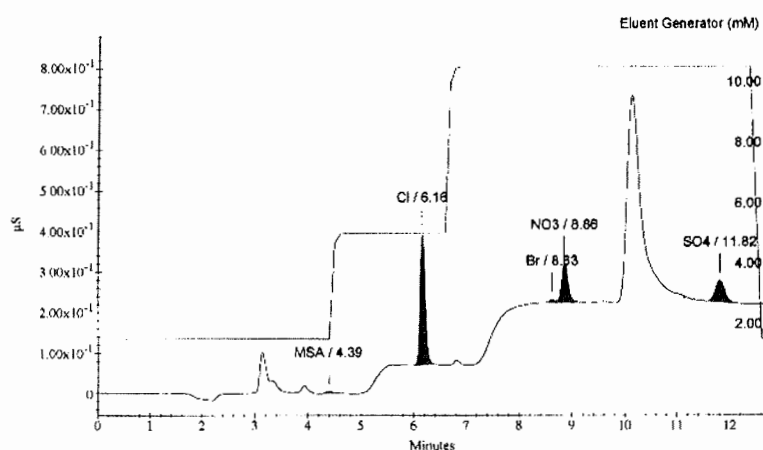


Figure 3.4: Anion method for IC measurements.

Example for an IC chromatogram for an anion calibration standard with lowest concentration level, e.g. 1 ng g^{-1} MSA and 5 ng g^{-1} SO_4^{2-} . For this measurement the eluent concentration increases in two step gradient from 0.5 mM to 10.5 mM.

The analyses of the cations were carried out using an isocratic gradient (Figure 3.5), i.e. with constant eluent concentration during the measurement. The duration of the cation analyses could have been shorter, but was adjusted to be the same as that of the anions in order to avoid confusion.

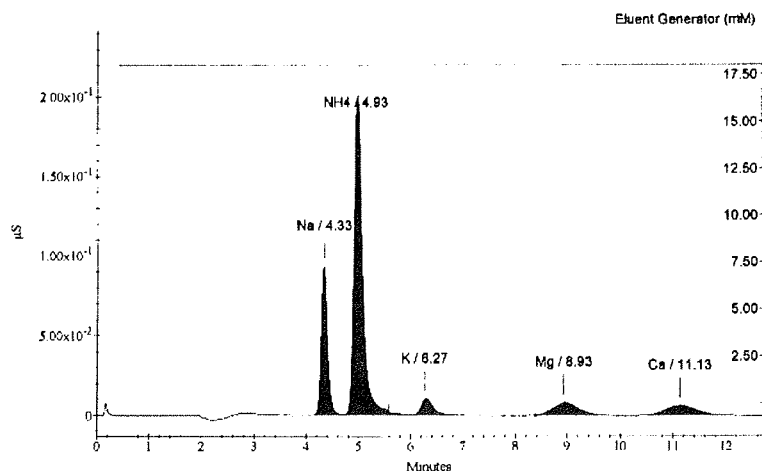


Figure 3.5: Cation method for IC measurements.

Example for an IC chromatogram for a cation calibration standard with lowest concentration level, e.g. $5 \text{ ng g}^{-1} \text{ Na}^+$ and $1 \text{ ng g}^{-1} \text{ Ca}^{2+}$. For this measurement the eluent concentration was kept constant at 18 mM for the whole run.

3.4.3 Blank samples and blank values

To check possible contamination during handling, ultra-pure water samples were prepared, frozen and processed as the ice cores. They were sealed in the same pre-cleaned PE bags like the ice core samples. To check the contamination of the analyses routine vials were filled with ultra-pure water (further on called vial blanks) and handled in the same way as all other samples. In Table 3.4.3 the average process (398 samples) and vial blank (659 samples) concentrations together with corresponding 2 times the standard deviation (2σ), median, minimum and maximum concentration values from all samples (6553 samples) are presented.

By application of this handling and analyses procedure, it is possible to distinguish, if contamination was caused by the analyses routine or by the sampling routine. The "analytical detection limit" is defined by the signal to noise ratio, but the "effective detection limit" by the blank concentrations. The lower the blank concentrations the better is the "effective detection limit".

Table 3.1: Process and vial blank concentrations.

Mean concentrations of process and vial blank values (PB and VB, respectively) together with corresponding 2 times standard deviation (2σ). Presented as well are the median, minimum and maximum concentration values; n is the number of samples

Component	VB mean	VB 2σ	PB mean	PB 2σ	sample median	sample minimum	sample maximum
	[ng g ⁻¹]						
no. samples	n=398		n=659		n=6553	n=6553	n=6553
MSA	0.00	0.00	0.00	0.00	5.79	0.24	65.64
Cl ⁻	2.53	3.32	2.42	2.74	41.64	1.10	915.69
Br ⁻	0.00	0.00	0.00	0.00	0.00	0.00	0.00
NO ₃ ⁻	2.68	5.53	2.12	4.46	50.90	0.85	266.52
SO ₄ ²⁻	1.69	3.54	1.96	5.65	65.34	1.85	789.76
Na ⁺	0.74	2.60	0.36	0.84	18.61	0.40	258.40
NH ₄ ⁺	1.68	1.98	2.03	1.23	3.84	0.22	214.37
K ⁺	0.75	1.71	0.63	1.00	1.755	0.14	128.79
Mg ²⁺	0.54	2.33	0.21	0.23	1.775	0.10	42.17
Ca ²⁺	1.30	2.78	0.84	0.87	2.26	0.18	155.64

3.4.4 Accuracy

The signal to noise ratio, the quality of calibration and the reproducibility of the response determine the accuracy of the ion chromatographic measurements.

- **SIGNAL TO NOISE RATIO:** Several reasons lead to a baseline noise, e.g. air bubbles in the system or dry parts of the suppressor membrane. The requirement to the system is that the response of the lowest concentration with the lowest peak area or peak height is still detectable. Therefore, the higher the signal to noise ratio, the more accurate the component concentration can be determined.

To reduce the baseline noise an external water supply for the suppressor was installed. Furthermore, cleaning the system was carried out once per week by running a high eluent concentration (for anion about 30 mM KOH and for cation 30 mM MSA). The baseline led to an analytical detection limit of about 0.04 ng g⁻¹ for MSA, the component most effected by the signal to noise ratio. The baseline noise was mostly around 0.0001 μ S (Figure 3.6).

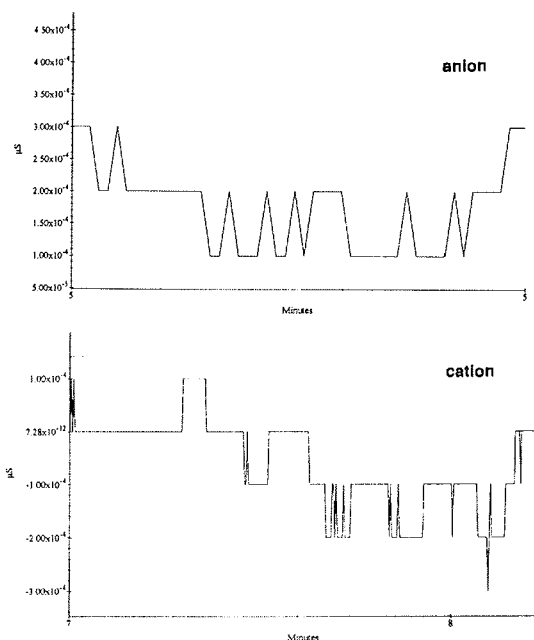


Figure 3.6: Baseline of anion and cation system.

The baseline of the anion and cation systems show noise of $0.0001 \mu\text{S}$. By comparison, the response signal of 1 ng g^{-1} concentration of MSA is $0.0074 \mu\text{S}$.

- **QUALITY OF THE CALIBRATION:** The response of the ion concentration is given by the peak area or peak height. To assign a certain species concentration with a peak area or peak height a seven point calibration with external standards was performed. These standards were analysed in between the samples and at minimum 3 standard sets were analysed per day. The concentration range of the seven standards cover the ion concentrations for all samples. Thus, the concentration ranges never reached or exceeded the highest standard concentrations.

For most of the samples the calibration was carried out by averaging four seven point standard sets. Performing a regression analysis on the calibration standards the coefficient of determination was $R^2 > 0.99$ confirming the linear dependence between species concentration and peak area or peak height. This coefficient could be reached for all components except for NH_4^+ , which will not be considered here.

- **REPRODUCIBILITY:** Carrying out IC analyses for all samples ($n_{\text{total}} = 6553$,

with 5637 ice core and 916 snow pit samples) in one would take close to 4 months. Over such a long time period the response of the system can be influenced, e.g. temperature in the laboratory, wear of the column, etc. Also, the system pressure was different between day and night. The long-term trends were covered by application of external standardisation.

The short-term system variations and blank variability determine the reproducibility. The blank variability was covered by producing process blanks every day of sampling and measuring vial blanks of every bag of vials used. The short-term trends were checked by four standard sets per day and by measuring standard sets continuously over three days. The response of peak area or peak height with the corresponding relative error was determined. The concentration range and median values of the samples, and the relative error of the measurements for each standard concentration level are presented in Figure 3.7. The inserts show the 2σ together with the standard concentrations.

The median values of the sample concentrations is 2 ng g^{-1} for Ca^{2+} , 2 ng g^{-1} for Mg^{2+} , 2 ng g^{-1} for K^+ and 4 ng g^{-1} for NH_4^+ . The concentrations of the blank samples are in the range of 3 ng g^{-1} (Ca^{2+}), 2 ng g^{-1} (Mg^{2+}), 2 ng g^{-1} (K^+) and 2 ng g^{-1} (NH_4^+). Thus, it is not possible to separate between sample and blank concentrations for these components. Therefore, these ion species are not further discussed in this work. Bromide was not detected at all, except in case of two very strong sea-salt events around the year 1970, where concentrations of about 3 ng g^{-1} were observed. Due to this fact, bromide is also not further discussed in this work. For all remaining components (MSA , Cl^- , NO_3^- , SO_4^{2-} , Na^+) the lowest detected concentrations are higher, or at least comparable to the lowest standard concentrations, which were significantly higher than the blank concentrations (Table 3.4.3).

The highest relative error was observed for NO_3^- with $\pm 22\%$ for a concentration of 5 ng g^{-1} . For typical concentrations the mean relative error of the components is lower than 10%. Considering the median values of the samples the mean relative error is lower than 3%.

Comparison of sample and blank concentrations indicate that contamination during the handling and analyses procedure is negligible and no further precautions have to be taken. Due to the low blank concentration values and relative errors no corresponding blank correction was performed for the presented ion concentrations.

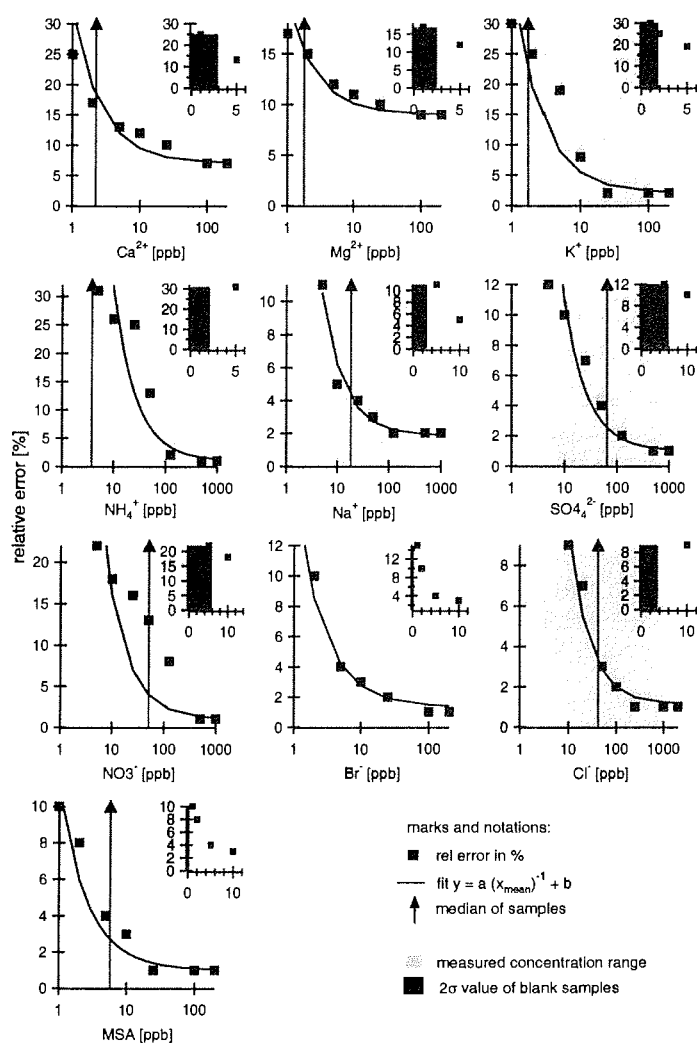


Figure 3.7: Accuracy of IC measurements.

Accuracy of the IC measurements. The solid line with squares presents the relative error of the calibration standards. The arrow marks the median value. The range from minimum to maximum sample concentrations is represented by the bright grey shaded area. In the inserts the 2 σ area of the blank concentrations are indicated by the dark grey shaded area. The corresponding relative errors are plotted versus the calibration standards by square markers. In general, the 2 σ area of the blanks is lower than the lowest standard and sample concentration level.

3.5 Conclusions

The set up for the de-contamination routine could be used to process a relatively large amount of ice core samples with negligible contamination. Accordingly, the 2σ area of the blank concentration was lower than the lowest standard, allowing the determination of low sample concentrations i.e. 1 ng g^{-1} MSA.

Hence, the low ion concentrations in Antarctic ice were neither affected by contamination during handling nor the relative error of the analyses procedure. The relative error for the median values is about 3%.

Very low baseline noise of $0.0001\ \mu\text{S}$ allowed a analytical detection limit as low as 0.04 ng g^{-1} . Therefore, a 1 ng g^{-1} MSA concentration, with typically amplitude of $0.0074\ \mu\text{S}$, could be detected unambiguously.

3.6 Acknowledgements

This work is a contribution to the "European Project for Ice Coring in Antarctica" (EPICA), a joint ESF (European Science Foundation)/EC scientific programme, funded by the European Commission and by national contributions from Belgium, Denmark, France, Germany, Italy, the Netherlands, Norway, Sweden, Switzerland and the United Kingdom. This is EPICA publication no. X. Financial support by Deutsche Forschungsgemeinschaft (project OE 130/3) is gratefully acknowledged.

We thank Prof. Dr. Heinz Miller and Prof. Dr. Otto Schrems for use of the laboratory facilities, Dr. Hans Oerter and Dr. Hubertus Fischer for fruitful discussions and helpful comments, and Dr. Christopher Zweck for improvements on the language. Thanks go for excellent assistance to Andrea Jaeschke in the cold-room and to Michaela Lelke and Thomas Max in the IC laboratory.

Chapter 4

Accumulation rates in Dronning Maud Land

4.1 Abstract

The European Project for Ice Coring in Antarctica (EPICA) includes a comprehensive pre-site survey on the inland ice plateau of Dronning Maud Land. The German glaciological programme during the 1997/1998 field season was carried out along a 1200 km traverse line on Amundsenisen and involved the sampling of the snow cover in snow pits and by shallow firn cores. This paper focus on accumulation studies. The cores were dated by profiles resulting from Dielectric Profiling and Continuous Flow Analysis. Distinct volcanogenic peaks and seasonal signals in the profiles served to establish a depth time scale. The eruption of the volcanoes Krakatoa, Tambora, an unknown one, Kuwae and El Chichon are well documented in the ice. Variations of the accumulation rates over different times were inferred from the depth time scales. A composite record of accumulation rates for the last 200 years was produced by stacking 12 annually resolved records. According to this record the accumulation rates decreased in the 19th century and increased in the 20th century. The recent values are by no means extraordinary, as they do not exceed the values at the beginning of the 19th century. The variation of the accumulation rates are most probably linked to temperature variations indicated in $\delta^{18}\text{O}$ records from Amundsenisen.

This chapter is published by: Oerter, H., F. Wilhelms, F. Jung-Rothenhäusler, F. Göktaş, H. Miller, W. Graf and S. Sommer (2000). Accumulation rates in Dronning Maud Land, Antarctica, as revealed by dielectric-profiling measurements of shallow firn cores. *Ann. Glaciol.* (30) p. 27-34.

4.2 Introduction

The European Project for Ice Coring in Antarctica (EPICA) focuses on two deep ice-core drillings in two regions within Antarctica, the Dome Concordia (Dome C) area in the Indian/Pacific sector and Dronning Maud Land (DML) in the Atlantic sector of Antarctica. The inland ice of DML is still a rather unexplored part of the Antarctic ice sheet. Therefore an intensive pre-site survey programme was set up, comprising ice-thickness measurements by airborne radio-echo-sounding surveys, ice-flow measurements by global positioning system (GPS) survey and glaciological investigations on shallow firn cores and 100 m ice cores.

The core studies will reveal the accumulation distribution across Amundsenisen and the accumulation and climate history during the last millennium. Norway, Sweden, The Netherlands, UK and Germany [Oerter et al., 1999] have been engaged with traverse work and airborne surveys since the 1995/96 field season. This paper describes the German traverse work in 1997/98 starting at Neumayer station at the coast and leading across Amundsenisen to the plateau of the inland ice.

4.3 Methods

4.3.1 Fieldwork

The area for the EPICA pre-site survey in Dronning Maud Land is Amundsenisen, East Antarctica (Figure 4.1). It includes the region between 72°S and 78°S, and between 15°W and 20°E. In the 1997/98 field season a ground traverse was carried out in the period 5 December 1997 through 2 February 1998, from Neumayer, the German wintering-over base, across Ritscherflya and up to the inland ice plateau east of Heimefrontfjella. The traverse route on Amundsenisen was approximately 1200 km. All measuring sites were identified as DMLxx (DML for Dronning Maud Land) with xx being a running number for the sites visited since the 1995/96 season (Figure 4.1, Table 4.1).

The sites DML11-DML23 were first visited in 1997/98. The traverse programme in 1997/98 included the drilling of 15 firn cores at 12 locations to a depth of 30-42 m, and of three ice cores 115-150 m deep. The aim of the drilling work was to reach at least the AD1810 layer which is strongly marked by the eruption of an unknown volcano in 1809 and provides, together with the eruption of Tambora in 1815, a common time marker for the dating of the cores.

The drilling work was complemented by snow-pit sampling to ensure proper representation of the near surface layers, because core quality is usually reduced

in the uppermost 2 m. The firn cores were logged and packed at the drilling sites and then flown to Neumayer Station. The cores were labelled FB98xx with xx being a running number from 03 to 17 for the cores on Amundsenisen, and 01 and 02 for a core adjacent to Neumayer station and one at the old Kottas field camp, respectively (Table 4.1). A field laboratory was established at Neumayer, using an old ventilation tunnel connected to the base approximately 5 m under the snow surface. The mean air temperature in the tunnel was $-10 \pm 2^\circ\text{C}$. Measuring devices were set up for the combined dielectric profiling (DEP) of the cores [Wilhelms et al., 1998] and density measurements by gamma-ray attenuation [Gerland et al., 1999] as well as for electrical conductivity measurements (ECM; [Hammer, 1980]).

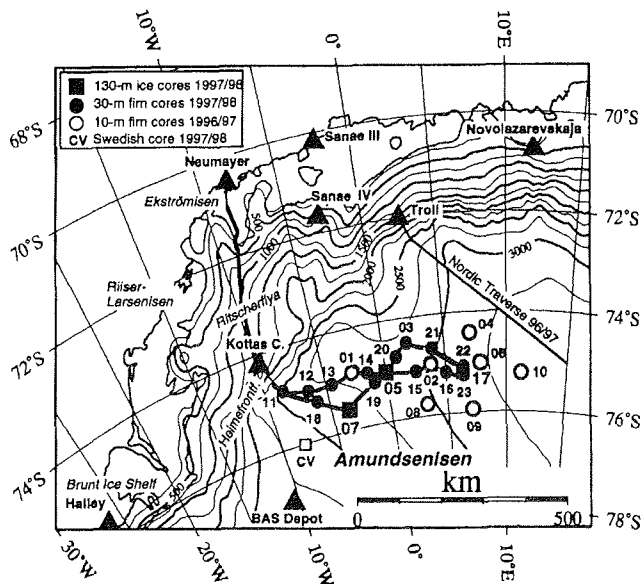


Figure 4.1: Map of Dronning Maud Land.

Dronning Maud Land showing the AWI traverse route 1997/1998 and drill locations. Elevation data based on ERS-1 altimetry (courtesy of J. Bamber, University of Bristol).

Facilities for cutting the cores and sub-sampling for further analysis were also available. Another small lab on the surface contained facilities for Continuous Flow Analysis (CFA, [Sigg et al., 1994]). During the field season all firn cores were analysed with respect to dielectric properties (DEP) and density, 10 cores were measured by ECM and 7 cores, including the 3 long ones, by CFA. The cores and cutted samples were shipped back at the end of the field season to the cold storage of Alfred Wegener Institute (AWI) at Bremerhaven.

Table 4.1: Coordinates for drill locations..

Coordinates for drill locations on Ekströmisen, Ritscherflya and Amundsenisen during the 1997/98 field season (Figure 4.1). The WGS84 coordinates were converted with the OSU91A model to orthometric heights (<http://gibs.leipzig.ifag.de>). Also shown are firn temperatures measured in the bore-holes at 10 m depth.

Locality	Core label	Date	Latitude	Longitude	Elevation	Elevation	10-m temp.
					WGS84	orthom.	
					[m]	[m a.s.l.]	[°C]
Pegelfeld Süd	FB9801	04.12.1997	70° 42.40'S	8° 25.06'W		45	-17.0
Kottas Camp	FB9802	11.-12.12.1997	74° 12.30'S	9° 44.50'W	1451	1439	-25.2
DML02	DML9602	01.02.1996	74° 58.10'S	3° 55.12'W	3027	3014	-44.4
DML03	FB9809	02.01.1997	74° 29.95'S	1° 57.65'E	2855	2843	-42.2
DML05	B32	25.-29.12.1997	75° 00.14'S	0° 00.42'E	2892	2882	-44.5
DML05, 500 m E	FB9806	29.12.1997	75° 00.16'S	0° 01.36'E		2880	
DML05, 1000m NE	FB9807	30.12.1997	74° 59.82'S	0° 02.17'E		2880	
DML07	B31	19.-21.12.1997	75° 34.89'S	3° 25.82'W	2680	2669	-44.3
DML11	FB9803	15.12.1997	74° 51.28'S	8° 29.82'W		2600	-37.1
DML12	FB9817	21.01.1998	75° 00.04'S	6° 29.90'W		2680	-40.2
DML13	FB9816	19.01.1998	75° 00.00'S	4° 29.78'W		2740	-42.3
DML14	FB9815	17.01.1998	74° 56.95'S	1° 29.67'W		2840	
DML15	FB9814	14.01.1998	75° 05.02'S	2° 30.06'E		2970	-45.0
DML16	FB9813	12.01.1998	75° 10.04'S	5° 00.20'E		3100	-45.5
DML17	B33	7.-10.1.1998	75° 10.02'S	6° 29.91'E		3160	-46.1
DML18	FB9804	17.12.1997	75° 15.02'S	6° 00.00'W		2630	-40.5
DML19	FB9805	23.12.1997	75° 10.04'S	0° 59.70'W		2840	-43.4
DML20	FB9808	31.12.1997	74° 45.04'S	0° 59.99'E		2860	-43.1
DML21	FB9810	04.01.1998	74° 40.03'S	4° 00.10'E		2980	-44.0
DML22	FB9811	06.01.1998	75° 05.04'S	6° 30.00'E		3160	
DML23	FB9812	11.01.1998	75° 15.05'S	6° 30.10'E		3160	-45.8

4.3.2 Dating the firn cores

The dating of the firn cores was done by means of the DEP and CFA data. The DEP method was described by Moore and Paren [1987] and Wilhelms et al. [1998]. The DEP data presented here were taken at a frequency of 250 kHz, in 5 mm increments with a 10 mm long measuring electrode. To account for density variations in the upper firn section the DEP data were corrected with a complex continuation of the Looyenga [1965] mixing model as suggested by Glen and Paren [1975].

The concentration of sodium, calcium, ammonium, hydrogen peroxide and the electrolytical conductivity have been measured with a Continuous Flow Analysis

(CFA) technique [Sigg et al., 1994]. For dating at a first step some very distinct peaks displayed in the DEP profiles (Figure 4.2) were assigned to volcanic events described in the literature to get the long-term accumulation value in this region before going into the details of the last 200 years. The most prominent peaks found in all 3 deeper cores are compiled in Table 4.2. Unfortunately, no nss-sulfate concentrations are determined up to now, which could finally prove the volcanic origin of the DEP peaks.

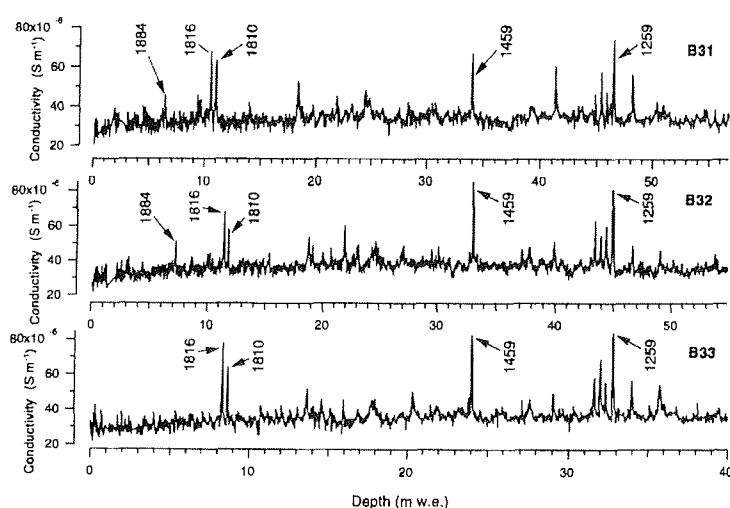


Figure 4.2: DEP conductivity profiles of ice cores B31, B32 and B33.

DEP conductivity profiles of ice cores B31, B32 and B33. The conductivity was corrected for density fluctuations using Looyenga's [1965] mixing model. The main peaks used for dating the cores are marked (Table 4.1). The depth axes are given in m. w.e. and are scaled so that the 1259 peaks correspond graphically for the three cores.

Two periods are very significant for dating purposes, namely the period 1810 to 1816 with the twin peak of an unknown volcano and Tambora, and the period 1259 through 1287 with a pattern of 4 peaks. Another event occurs in all three cores between these two periods in comparable depths. In the following the horizons used for dating are described in more detail.

The deepest and largest peak in the group of the four peaks marks according to Langway et al. [1988] the horizon of the year 1259. Delmas et al. [1992] assumed that this peak is connected with an early eruption of El Chichon (Mexico) based on the work of Palais et al. [1990]. This assumption is confirmed by Palais et al. [1992].

The pattern with 4 peaks is described by Delmas et al. [1992] and Langway et al. [1994],[1995] who dated peaks in cores from Byrd station and South Pole nearly equal to the years 1259/1259, 1270/1269, 1278/1277 and 1287/1285, respectively. Moore et al. [1991] show a DEP conductivity profile of a core from Mizuho plateau with only one distinct peak assigned to the year 1259. At Dome F also 4 peaks are reported [DomeF, 1998].

Table 4.2: Volcanic events identified in the ice cores.

Volcano name, date of eruption, and depth of horizons at our ice cores.

volcano	date of eruption/ deposition	depth horizon at DML07 (core B31) [m w.e.]	depth horizon at DML05 (core B32) [m w.e.]	depth horizon at DML17 (core B33) [m w.e.]
Krakatoa	1883/84	6.47	7.22	5.44
Tambora	1815/16	10.62	11.46	8.36
Kuwae	1458/59	34.01	33.04	24.00
El Chichon	1258/59	46.53	45.00	32.8

The single event documented in the 3 cores at comparable relative depths to the 1259 peak was assigned to the year 1459. This event is not as well documented in the literature as the 1259 event. Cole-Dai et al. [1997] described a similar peak in a core from Siple station to the eruption of Kuwae. Delmas et al. [1992] mention a volcano horizon for the year 1450 at South Pole, Langway et al. [1995] for the year 1464 at Byrd station and for the year 1450 at South Pole, but they conclude that the deposition year most probably may be 1459 as revealed by a Greenland ice core at Crete. The DomeF [1998] do not mention a peak in this period and Moore et al. [1991] follow Legrand and Kirchner [1990] and assign the corresponding peak to 1460 AD.

The twin peaks from 1810 and 1816 are displayed in all cores from Amundsenisen. These peaks are well dated for Antarctic ice cores and reported by Langway et al. [1995] for Byrd station and South Pole, Delmas et al. [1992] for South Pole, Cole-Dai et al. [1997] for Siple station and Moore et al. [1991] for Mizuho plateau. These twin peaks were identified without doubt for the ice cores B31, B32 and B33 as well as for the firn cores FB9804 to FB9817. The firn cores FB9801 (Neumayer station, Pegelfeld Süd), FB9802 (Kottas Camp) and FB9803 (DML11) do not reach this time due to higher accumulation rates there. How well these are represented in the different DEP profiles can be seen from Figure 4.3.

The whole set of DEP profiles in the period since 1810 is displayed in Figure 4.3. There are several other signals in the DEP profiles which helped to synchronise the

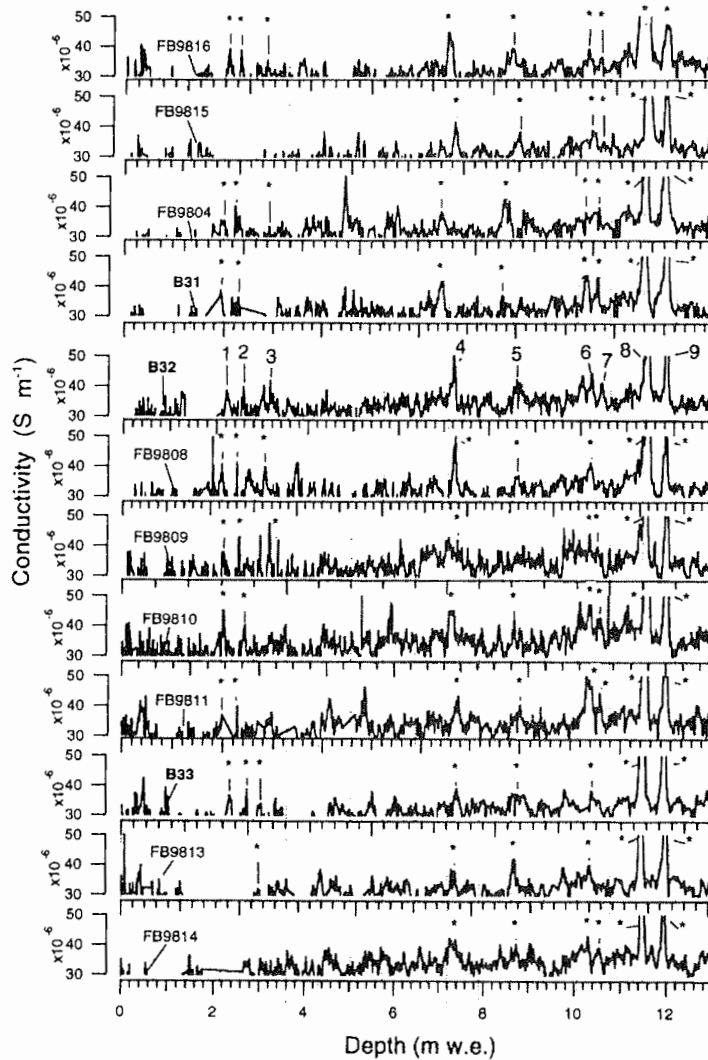


Figure 4.3: DEP profiles of firn cores from DML.

DEP profiles of firn cores from DML. The depth axes are given in m. w.e. and are scaled so that the 1810 peaks correspond graphically for the 12 cores. Nine peaks are labelled at core B32 (1-9) and are detectable also in the other cores (marked by asterisks).

dating of the cores. However, they are not as evident as the 1816 and 1810 peaks. Nine peaks were selected at core B32 (Figure 4.3; no. 1-9) which can be correlated to peaks in the other cores (marked by a asterisks).

In the time period between 1832 and 1836 two peaks are displayed (no. 6 and 7) at core B32 and in several of the other cores. One of them could correspond to a peak present in the snow cover at Byrd station [Langway et al., 1995], at South Pole [Langway et al., 1995; Delmas et al., 1992], at Dyer plateau [Cole-Dai et al., 1997], at Siple station [Cole-Dai et al., 1997] and at Mizuho plateau [Moore et al., 1991]. Delmas et al. [1992] dated this peak in the nss-sulfate profile to the year 1836 and assigned it to the eruption of Coseguina in 1835 in Nicaragua. It is very likely that peak no 6 corresponds to this eruption.

The eruptions of Krakatoa in 1883 and Tarawera in 1886 [Newhall and Self, 1982] belong after the eruption of Tambora in 1815 and of the unknown volcano in 1809 to the strongest during the past 200 years. The Krakatoa eruption was detected in the 1884 layer of nss-sulfate profiles at Byrd station [Langway et al., 1995], at South Pole [Langway et al., 1995; Delmas et al., 1992] and at Mizuho plateau [Moore et al., 1991]. [Isaksson et al., 1996; Isaksson et al., 1999] used this time marker for dating firn cores in Dronning Maud Land. Also in our cores a corresponding peak was found (peak no 4 at B32); it is pronounced in most of the cores, but very weak at core FB9809 and FB9804.

The eruption of Agung in 1963 (peak no. 1 at B32) was not detectable without doubt in each of the cores, in some cores due to bad core quality in this depth interval. There are two more peaks (no. 2 and 3) which coincide with the years 1959 \pm 1 and 1952 \pm 1 in the dated cores. The source of these peaks is unclear.

Annual layer counting

The profiles of sodium, calcium and ammonium concentration as well as the DEP profiles show very regular annual fluctuations (for DEP see Figure 4.4). While enhanced sea salt concentrations during winter [Wagenbach et al., 1998] cause the sodium and calcium peak, the seasonality in the ammonium record is not yet understood. The variations in the DEP profiles seem to be due to higher ion concentrations during the summer months [Wilhelms, 1996].

As DEP measurements are, in contrast to the CFA results, available for all cores, these profiles were used in this work for year-to-year dating with the common reference horizons of 1816 and 1810 AD. The peaks in the DEP profiles (the summer horizons) were used for defining annual layers. Thus the peaks mark the beginning or the end of a calendar year. DEP values from pieces with core-catchers damage

or around breaks were rigorously removed from the data-sets. Sometimes missing DEP data could be supplemented with ECM data. For some small, damaged core pieces neither DEP nor ECM data are available. In such cases, annual layers were introduced by linear interpolation using the mean accumulation rates since 1810.

Annually resolved depth-time scales, with the 1810 horizon as a common fixed point, were established for all cores and were used to calculate chronologies of annual accumulation rates and annual $\delta^{18}\text{O}$ values (five cores only so far). Examples of the annual variation of the electric conductivity determined by DEP and the deduced annual layers are shown in Figure 4.4. The counting of annual layers is not possible without some ambiguities, and can only be improved by using known reference horizons.

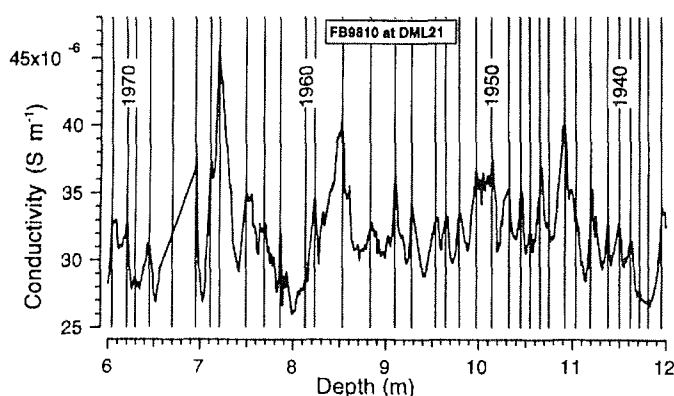


Figure 4.4: DEP profile of firn core FB9810.

DEP profile of firn core FB9810 with density correction after Looyenga [1965] and deduced annual layering.

The seven DEP peaks since 1816, marked in the profile of core B32 (Figure 4.4) and not used for the dating, appear in the cores at slightly different dates. This time shift can be used as a measure for dating error. Deposition dates and their uncertainties are: 1965 ± 1.2 , 1959 ± 1.1 , 1952 ± 1.1 , 1884 ± 1.0 , 1862 ± 2.1 , 1835 ± 1.3 , 1832 ± 1.7 . Thus we assume that the annual layer dating from 1810 to 1998 is accurate within ± 2 years.

4.4 Results and Discussion

Accumulation rates were calculated using the dating described above and the firn or ice density from gamma-ray attenuation profiles (see Gerland et al. [1999] and Wilhelms [1996] for the method used), which were also determined already in the field. Four data sets of accumulation rates are now available. The snow-pit data contain the most recent accumulation rates during the last ten years, the 10 m firn cores from the 1995-97 seasons, dated mainly by means of tritium and DEP [Oerter et al., 1999], covered a period of up to 100 years, the 30 m firn cores from 1997/98 season a period of 200 years and the three ice cores to medium depths revealed the accumulation history back to 1259 AD. (Table 4.3).

Table 4.3: Long-term accumulation rates.

Long-term accumulation rates on Amundsenisen deduced from volcanic events in the ice cores (see Table 4.2).

time interval	DML07 [kg m ⁻² a ⁻¹]	DML05 [kg m ⁻² a ⁻¹]	DML17 [kg m ⁻² a ⁻¹]
1259-1459	62.6	59.8	44.0
1459-1816	65.5	60.4	43.8
1816-1997	58.4	63.0	45.9

4.4.1 Accumulation history during the last 700 years.

1259 to present

Mean values of the accumulation rates in different time spans can directly be derived from the depth of the volcanic horizons given in Table 4.2. The accuracy of these values is limited by the uncertainty of the dating (± 1 year), by the accuracy of the depth scale and by the error of the density values which is in the order of 1%. For example, the accuracy of the 100 year mean accumulation rates is in the order of 2%.

For the periods 1259 to 1997 the mean accumulation rates at DML07 (ice core B31), DML05 (core B32) and DML17 (core B33) are $63.0 \text{ kg m}^{-2} \text{ a}^{-1}$, $60.9 \text{ kg m}^{-2} \text{ a}^{-1}$, and $44.4 \text{ kg m}^{-2} \text{ a}^{-1}$, respectively. For the period 1459 to 1997 the mean values are less than 1% different from these values. However, in the interval from 1816 to 1997, after a 550 years period of nearly constant values at the three sites (Table 4.3), the accumulation history was different. At DML07, on the southwestern slope, the accumulation rate decreased by about 10%. In contrast, along the ice divide (running from east-west), at both sites, DML17 and DML05, the mean values increased by

about 5%.

1800 to present

The annually resolved accumulation rates calculated for the last two centuries at 10 sites are shown in Figure 4.5. The inter-annual variability of the accumulation rate is high. It is given in Table 4.4 as standard deviation of the annual mean values for 1801-1997 corresponding to a percentage between 32% and 36% (except at DML07). An even higher variability of 40%, is found at DML07 (B31) in the south-western part of the investigation area.

The time series were smoothed by a Gaussian low-pass filter over 11 years to account for the high-frequency deposition noise (thick line in Figure 4.5). The individual time series were stacked to produce a composite record of accumulation rates for Amundsenisen. The smoothed time series reveal for the sites DML03 (core FB9809), DML20 (core FB9808), DML05 (core B32) and DML15 (core FB9814), a statistically significant increase, for the site DML18 (core FB9804) a negative trend over the 200-year period since 1800. All other cores do not show a trend over the 200-year period. Changes of accumulation rates of regional relevance for Amundsenisen can be expected from the stacked series.

According to the stacked series, the accumulation rate, A , decreased in the 19th and increased in 20th century, with a turn of the trend around the year 1905. Linear regression analysis results in $dA/dt = -0.124 \pm 0.021 \text{ kg m}^{-2} \text{ a}^{-1}$ ($r=-0.50$) and $0.068 \pm 0.024 \text{ kg m}^{-2} \text{ a}^{-2}$ ($r=0.20$), respectively. The 20th century started with minimum accumulation rates and ends with values not higher than at the beginning of 19th century. Similar trends are found for the stable isotopes, as will be shown later (Figure 4.7).

4.4.2 Spatial distribution of accumulation

The local variability of the snow cover and of the accumulation rates can be assessed by comparing the results of cores recovered close together. At DML03, DML05, and DML07 accumulation rates were determined using different cores and pits (Table 4.4). Here, we compare only the means over the period 1960-1996 not the fluctuations in the time series. This period was selected, because the cores taken in 1997 were dated by tritium profiles back to 1960. At all locations the values agree well: at DML03, the location with the highest accumulation rate, the values from the two cores DML9703 ($89.5 \text{ kg m}^{-2} \text{ a}^{-1}$) and FB9809 ($90 \text{ kg m}^{-2} \text{ a}^{-1}$) are within the accuracy limit. At DML05 the accumulation rate determined with core DML9705 ($70.1 \text{ kg m}^{-2} \text{ a}^{-1}$) and core B32 ($69.8 \text{ kg m}^{-2} \text{ a}^{-1}$) equal each other. Fi-

Table 4.4: Firn cores and snow pits sampled in 1997/1998.

The table shows mean accumulation rates and the scatter (1σ) of the annual values for the given periods. Dating of the cores from 1997/1998 is based on DEP profiles, the snow pits were dated using stable isotopes. For DML02, DML03, DML05, and DML07 the results of older cores [Oerter et al., 1999] have also been shown.

locality	core/pit label	depth to [m]	time interval	accumulation rate [kg m ⁻² a ⁻¹]
Neumayer, Pegelfeld Süd	FB9801	27.02	1948-1997	317 ± 107
Kottas	FB9802	26.43	1881-1997	129±38
Kottas	FBK9601	10.66	1962-1995	125±16
DML02	DML9602	10.79	1919-1995	57±14
DML02	SS9813	0.47	1995-1997	51±17
DML03	DML9703	11.56	1941-1996	91±29
DML03	FB9809	33.01	1801-1997	89±29
DML03	SS9807	1.00	1994-1997	89±25
DML05	B32	25.44	1801-1997	62±21
DML05	DML9705	11.16	1930-1996	71±21
DML05	SS9805	2.68	1985-1997	71±19
500 m E DML05	FB9806	23.80	1816-1997	62
1000 m NE DML05	FB9807	24.20	1816-1997	67
DML07	B31	24.92	1801-1997	59±24
DML07	DML9707	12.13	1908-1996	57±16
DML07	SS9803	2.46	1985-1997	62±19
DML11	SS9801	2.04	1989-1997	76±18
DML12	FB9817	23.00	1816-1998	62
DML12	SS9818	1.85	1989-1997	68±17
DML13	FB9816	19.73	1800-1997	47±17
DML13	SS9817	1.77	1991-1997	80±20
DML14	FB9815	25.77	1801-1997	53±19
DML14	SS9815	1.95	1990-1997	81±37
DML15	FB9814	25.77	1801-1997	64±21
DML15	SS9814	2.07	1988-1997	71±18
DML16	FB9813	19.30	1816-1997	48
DML16	SS9812	2.01	1988-1997	70±22
DML17	B33	19.57	1801-1997	47±16
DML17	SS9810	1.72	1989-1997	63±17
DML18	FB9804	20.57	1801-1997	50±16
DML18	SS9802	1.77	1988-1997	55±15
DML19	FB9805	18.40	1810-1997	44
DML19	SS9804	2.25	1988-1997	78±24
DML20	FB9808	26.77	1801-1997	68±22
DML20	SS9806	1.71	1992-1997	97±19
DML21	FB9810	32.18	1801-1997	86±29
DML21	SS9808	1.88	1990-1997	83±23
DML22	FB9811	23.45	1801-1997	58±16
DML22	SS9809	0.86	1994-1997	74±17
DML23	FB9812	16.30	1816-1997	38

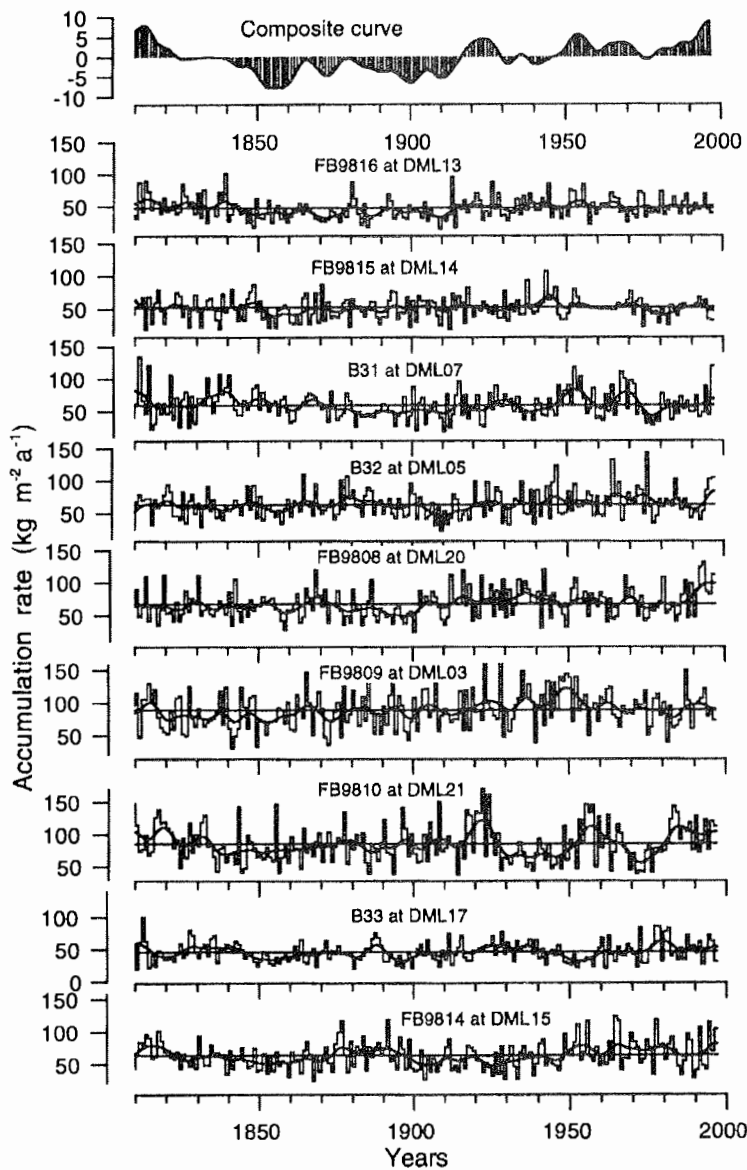


Figure 4.5: Time series of accumulation rates.

Annually resolved time series of accumulation rates at nine locations on Amundsenisen. The thick line was created by smoothing the records with a Gaussian low-pass filter over 11 years. The composite record is shown on top as deviations from the mean value (it includes also the records from cores FB9804, FB9811, and FB9813, which are not shown).

nally, also at DML07 the two cores from different campaigns agree: DML9707 from 1997 ($59.3 \text{ kg m}^{-2} \text{ a}^{-1}$) and B31 from 1998 ($59.8 \text{ kg m}^{-2} \text{ a}^{-1}$). These findings show that the small-scale variability of the accumulation rates is compensated within a period of 35 years.

This first compilation of the spatial distribution of the accumulation rates is based on 7 tritium-dated 10 m cores [Oerter et al., 1999] and on 17 DEP- or CFA-dated 30 m firn cores, described in this paper, which gave means for the periods 1960-1996 and 1810-1997, respectively (Table 4.4). To mix both data sets with different time spans seems to be justified for this first approach. According to the stacked record, the 200 year mean equals the mean which results from the tritium dating over the last 35 years, within 5%. The alternative, to take only the mean values over the last 35 years from all cores, would have reduced the number of accumulation values available (five cores are not dated yet on an annual basis) and the accuracy of the accumulation rates, because the Agung eruption is not clearly visible in all DEP profiles.

For compiling the contour map, the data-set was complemented by accumulation values from the Nordic traverse in 1996/97 [Isaksson et al., 1999] to improve the eastern boundary conditions. In addition, south of point DML09 the accumulation values of the South Pole-Queen Maud Land Traverse (SPQMLT) in 1964-68 [Picciotto et al., 1971] were used, and between DML02 and DML05 the accumulation value of $77 \text{ kg m}^{-2} \text{ a}^{-1}$ reported by Isaksson et al. [1996] was included. The spatial interpolation was calculated with a thin plate spline function [Barrodale et al., 1993], an interpolation tool included in the EASI/PACE software package (all points got the same weight). The generated accumulation distribution is shown in Figure 4.6.

West, as well as east, of the studied area spots with accumulation rates less than $45 \text{ kg m}^{-2} \text{ a}^{-1}$ were found. In the middle, mainly eastwards of point DML05, along the ice divide the accumulation rates are 45 and $65 \text{ kg m}^{-2} \text{ a}^{-1}$. Towards the north, the accumulation rates increase to around $90 \text{ kg m}^{-2} \text{ a}^{-1}$, as determined at DML03. The accumulation rate reported by Isaksson et al. [1996] causes a southwards-bounded tongue in the pattern. This means that for this location this value is higher than expected from the AWI firn cores alone. How the accumulation rates develop further to the Southwest will be revealed by the results of the Swedish/Norwegian work as well as of the British Antarctic Survey work in the 1997/98 field season. Both groups recovered each a 130 m core (locations CV and BAS depot in Figure 4.1) and shallow firn cores.

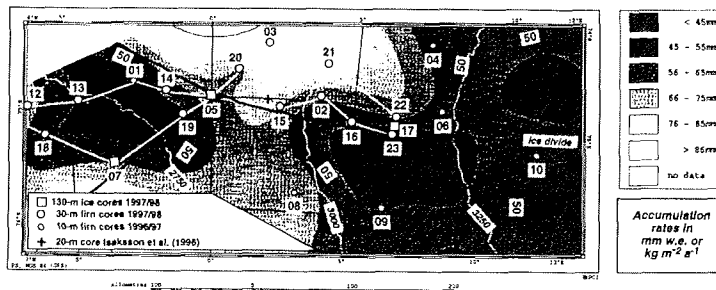


Figure 4.6: Map of accumulation rates.

Accumulation rates on Amundsenisen in the area covered by the firn cores (numbered points, cf Figure 4.1) drilled by AWI between 1995 and 1998. The thick white line shows the German traverse route in 1997/1998. The cross marks the location of a 20 m firn core by Isaksson et al. [1996]. The white lines are contour lines (cf Figure 4.1), the thin black line is the isoline for an accumulation rate of $50 \text{ kg m}^{-2} \text{ a}^{-1}$. The ice divides crossing the area under investigation are also indicated.

4.4.3 Relationship between temperature and accumulation rates

The spatial distribution of accumulation rates may reflect the precipitation field and should then be governed by the temperature field. To test, if the accumulation rates and the air temperature are correlated, we used the 10-m firn temperature (Table 4.1) at the sample sites. This firn temperature stands for the mean annual air temperature over the last few years and is not representative for the last 200 years, but for the correlation only the temperature differences are of interest. Figure 4.7 displays the accumulation rate and temperature data-sets.

At a first step the accumulation rates and the 10 m firn temperature in Dronning Maud Land were correlated linearly. The relationship becomes significant if the values of the six sites DML01, DML12, DML13, DML18, DML19 and DML23 are omitted (Figure 4.7). All these points (except of DML23) gather in the west of the plateau. Without them a gradient of $6.4 \text{ kg m}^{-2} \text{ a}^{-1} \text{ K}^{-1}$ results. With the same accuracy, the data can be approximated by a function which is proportional to the derivative of the mixing ratio (Figure 4.7). That means, the accumulation rates on the plateau of Dronning Maud Land are strongly correlated to the loss of water vapour from a cooling air mass.

With a similar equation, which regards the decrease of the water content with

temperature and the temperature gradient, the accumulation rates on the Ronne ice shelf could be calculated [Graf et al., 1999]. The low accumulation rates at some of the sites in the western part may be due to the trajectories of the moist air masses, which reach the plateau from the north-east [Noone et al., 1999] or may be caused by katabatic winds, which are stronger in the West than in the central part of Amundsenisen, as indicated by surface roughness.

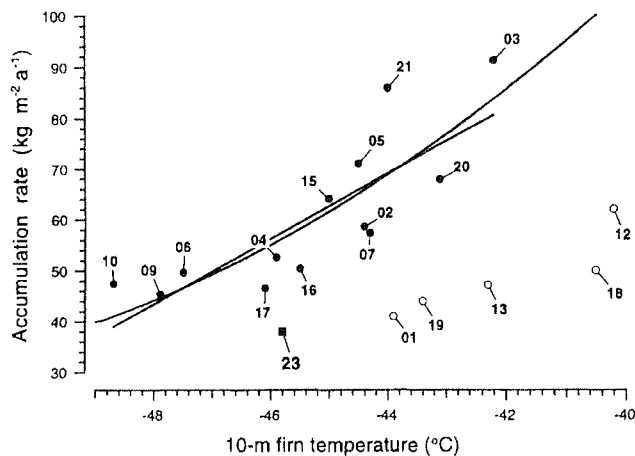


Figure 4.7: Accumulation rate versus 10 m firn temperature.

Relationship between accumulation rate and 10 m firn temperature. The straight line gives the regression line through the data points. The curve represents the fit of a function, which is proportional to the temperature derivative of the mixing ratio, to the data points. The accumulation rates are proportional to the water-vapour loss from a cooling air mass. The data from sites marked by open symbols were omitted in the fitting procedures.

4.4.4 Time series of accumulation rates and climate

Oerter et al. [1999] investigated ten firn cores recovered in the 1995-1997 field season. In the meanwhile the first stable-isotope data from the 1997/98 cores have also become available. These data include five time series of ^{18}O contents extending to the beginning of the 19th century; the cores are from DML05 (core B32), DML17 (core B33), DML18 (core FB9804), DML15 (core FB9814), and at DML14 (core FB9815). The individual series were stacked to a composite record to enhance the signal-to-noise ratio. According to the composite record, the $\delta^{18}\text{O}$ content decreased in the 19th and increased in 20th century. The increase of the $\delta^{18}\text{O}$ content in the 20th century (1905-1997: $0.0078 \delta^{18}\text{O a}^{-1}$) is lower than the decrease during the 19th century (1801-1905: $-0.0128 \delta^{18}\text{O a}^{-1}$).

Figure 4.8 shows the composite record of the accumulation rates and that of the ^{18}O content for the same time interval. In the following only the long-term trend of the composite time series is considered. Visual inspection already shows the similarity of both composite time series. The analysis reveals a positive correlation between ^{18}O contents and accumulation rates with $r=0.20$ for the unsmoothed records. The correlation becomes better by smoothing the series with a Gaussian low pass filter over 11 years, which yields a correlation coefficient of $r=0.33$. This positive cross-correlation is remarkable and makes it probable that the variation of both of the accumulation rate and the isotope content are caused by temperature fluctuations.

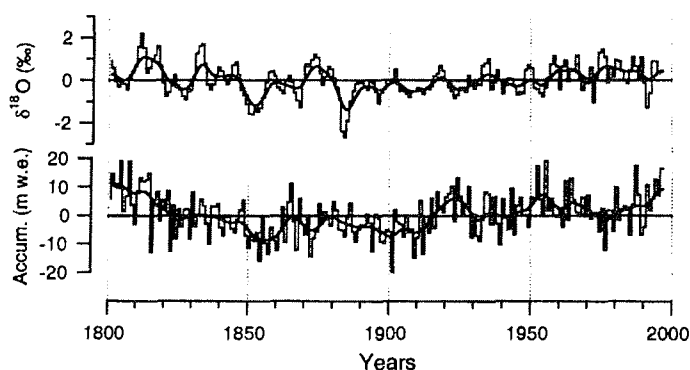


Figure 4.8: Time series of $\delta^{18}\text{O}$.

Composite annually resolved time series of $\delta^{18}\text{O}$ values (above) and accumulation rates (below). Shown are the deviations of annual values from the 1800-1997 means. The smoothed curve was calculated using a Gaussian low-pass filter over 11 years.

The data are consistent: using the temperature-isotope relationship determined for the region of Amundsenisen 5.5 ± 0.3 (2H K^{-1} [Oerter et al., 1999], which corresponds to 0.69 ± 0.04 $\delta^{18}\text{O K}^{-1}$, the composite ^{18}O record infers a temperature increase of 1.04-1.2 K in the 20th century and a temperature decrease of 1.93-2.26 K in the 19th century. The variation of the accumulation rates is nearly exactly what is expected from these temperature variations. With the empirical relationship between 10 m temperature and accumulation rate on Amundsenisen given above (6.4 ± 1.5 $\text{kg m}^{-2} \text{a}^{-1} \text{K}^{-1}$), the temperature variations would indicate an increase of the accumulation rates since 1905 of 6.7-7.7 $\text{kg m}^{-2} \text{a}^{-1}$ and a decrease from 1801 through 1905 of 12.3-14.5 $\text{kg m}^{-2} \text{a}^{-1}$. From the accumulation rate gradients discussed above nearly the same values follow, for the 20th century an increase of

6.3-7.4 kg m⁻² a⁻¹ and for the 19th century a decrease of 12.9-13.5 kg m⁻² a⁻¹. This consistency of the accumulation and isotope data supports the interpretation that temperature changes have caused the variations of the stable isotope content and of the accumulation rates over the last two centuries.

4.5 Conclusions

The dating of the firn cores was done by means of data from the DEP and CFA of chemical constituents. Very distinct peaks displayed in the DEP and CFA profiles can be assigned to volcanic events and serve as time markers to establish a depth time scale; this was refined by the seasonal signals in the measuring profiles. The eruption of the following volcanoes are well recorded across Amundsenisen in the firn layers: Krakatoa (1883), Tambora (1815), an unknown volcano (1809), Kuwae (1458) and El Chichon (1258). The volcanic origin of the peaks is very probable but not proven yet by sulphate measurements. The dating is accurate within one year close to the time markers and may fluctuate between these markers by ± 2 years. A dating without known reference horizons only by stratigraphic means leaves the time series with high ambiguities.

Comparison of the DEP profiles showed that during the past 200 years the relative changes in the accumulation rate were the same at almost all locations. This is also supported by the cross-correlation analysis between the individual and the composite records. Most pronounced are the different trends in the 19th and 20th century. These trends correspond to those in the composite record of the ¹⁸O contents. A climatic cause for these trends seems very probable. Both trends can be explained by the same temperature variations. The observed variations of the accumulation rates are within the natural variability. The values at the end of the 20th century are not higher than at the beginning of the 19th century.

The mean accumulation rates were used to calculate the distribution of the accumulation rates. The resulting pattern is reasonable. The mean accumulation rates can partly be explained by the temperature field.

The DEP profiles and the annual variations within these profiles indicate that the annual layering in the investigated part of Amundsenisen is very regular and that the precipitation of all seasons is comparable well conserved in the snow cover. From this point of view the investigated area of Amundsenisen seems to be favourable for a drill location.

4.6 Acknowledgements

We thank Alexandra Ebbeler (AWI) for doing the ECM measurements, Heinrich Ruffli (University of Berne) and W.-D. Hermichen, Andrea Jaeschke and Fernando Valero-Delgado (AWI) for assistance in the field lab and cold lab at AWI. Anna Olfmann and Petra Seibel (GSF) as well as Günther Meyer and Eva Viehoff (AWI) for doing isotope measurements. Thanks go to all members of the German EPICA traverse in 1997/98 for assisting the field work. Financial support by Deutsche Forschungsgemeinschaft (Projects Re762/2 and Oe130/3) is gratefully acknowledged. This work is a contribution to the "European Project for Ice Coring in Antarctica" (EPICA), a joint ESF (European Science Foundation)/EC scientific programme, funded by the European Commission under the Environment and Climate Programme (1994-1998) contract ENV4-CT95-0074 and by national contributions from Belgium, Denmark, France, Germany, Italy, the Netherlands, Norway, Sweden, Switzerland and the United Kingdom. This is EPICA Publication no. 6 and AWI publication no. 1664.

Chapter 5

High resolution chronology of earth's volcanic history

5.1 Abstract

In the framework of the European Project for Ice Coring in Antarctica (EPICA) the Alfred Wegener Institute carried out comprehensive pre-site surveys on Amundsenisen, Dronning Maud Land, Antarctica in the past decade. From the pre-site surveys in 1997/1998 and 1999/2000 four intermediate deep ice cores and 15 snow pits were analysed for ionic composition by ion chromatography (IC) and Dielectric Profiling (DEP). It could be shown that 75% of the peaks in the DEP record have their origin in high nss-sulphate concentrations. Furthermore, with a combination of annual layer counting, nss-sulphate records and identified volcanic H₂SO₄ deposition a chronology of volcanic eruptions from 165 to 1997 A.D. is provided. The 48 identified volcanic eruptions between 165 and 1997 A.D. were identified with an uncertainty of ± 1 years between 1600 to 1997 A.D., linearly increasing to ± 5 years at 1259 A.D., and ± 22 at 165 A.D. Moreover, evidence about the uniform spatial distribution pattern of the volcanic H₂SO₄ deposition of the eruptions Mt. Pinatubo and Cerro Hudson in year 1991, studied in 13 snow pits, could be derived.

This chapter is based on: Göktaş, F., H. Oerter, H. Fischer, W. Graf, H. Miller and R. Weller. High resolution chronology of earth's volcanic history: implications for changes in small scale climate condition. Submitted to JGR

5.2 Introduction

Extraordinary efforts have been put into establishing a chronology of volcanic eruptions, over the last 10,000 years [Simkin and Siebert, 1993]. The chronology is well established for the past 500 years and dating of individual eruptions considerably more accurate for the Northern than for the Southern Hemisphere. In particular before 1600 A.D., the documentation of volcanic eruptions from the Southern Hemisphere, especially from South America and the South-West Pacific region, is incomplete and eruption dates highly uncertain [Simkin and Siebert, 1993].

In general, plinian volcanic eruptions inject megatons of debris and gases into the atmosphere. Apart from volcanic ashes, CO_2 and water vapour, the reactive gaseous compounds SO_2 , HCl and partly HF are the most important atmospheric entries after prominent plinian eruptions. These violent eruptions form a volcanic plume which can reach the stratosphere due to its kinetic energy and the inherent convective buoyancy [Schminke, 1993]. Sulphur dioxide, which is subsequently transformed into $\text{H}_2\text{SO}_4/\text{H}_2\text{O}$ aerosol causes the largest aerosol perturbation in the stratosphere [McCormick et al., 1995]. The highly water soluble HCl is largely scavenged and removed by condensed water within the eruption plume so that only a small fraction of the originally exhaled HCl will reach the stratosphere [Tabazadeh and Turco, 1993]. Due to the long stratospheric residence time of about one year [Raisbeck et al., 1981], atmospheric injections caused by large plinian eruptions are globally distributed and deposited. Unfortunately, due to the fact that the fraction of sulphur gases injected into the atmosphere is highly variable for different volcanoes, only the impact on the atmospheric sulphate aerosol burden can be estimated from sulphate signals in ice cores, not the eruptive strength of the volcanic eruption. However, it has been shown that the atmospheric perturbations caused by sulphate aerosols are more persistent than volcanic ash injections [Carey and Sigurdsson, 1982; McCormick et al., 1995]. Thus, the impact of volcanic eruptions on the atmospheric aerosol burden can be assessed by the sulphate signal archived in ice cores. Several ice cores from Antarctica and Greenland have been analysed with this purpose e.g. by Karlöf et al. [2000], Palmer et al. [2001], Delmas et al. [1992], Legrand and Delmas [1987], Cole-Dai et al. [1997], Langway et al. [1994], Moore et al. [1991], Zielinski et al. [1997], Hammer [1977]. In these studies for example prominent but unknown eruptions could be assigned to the years 1809, 1259, 1269 and 1279 A.D. within ± 10 years [Simkin and Siebert, 1993]. Some of the previous studied ice cores were drilled at sites with relatively high accumulation rates, so that the time of a volcanic eruption could be specified with an accuracy of ± 1 year, but these records do not reach far back in time [Palmer et al., 2001]. Other ice cores

reach further back in time, but the accumulation rate or sampling resolution is too low for annual layer counting [Legrand and Delmas, 1987]. Glacio-chemical studies on volcanic chronology from the Antarctica Plateau covering more than 150 years in high resolution are limited to ice cores from South Pole, Dome Concordia (Dome C), Byrd and Siple Station. Here, we present a detailed investigation of several ice cores drilled on Amundsenisen, Dronning Maud Land (DML) with the aim to provide an accurate and unique volcanic chronology over the last two millenia.

Amundsenisen, Dronning Maud Land (Figure 5.1), is located on the Antarctic Plateau far away from continental sites and human activities. Therefore, ice core records from Amundsenisen are expected to provide undisturbed information about the variation of the background aerosol composition by volcanic eruptions [Legrand and Mayewski, 1997; Delmas, 1982]. The combination of a sufficiently high accumulation rate of $62 \text{ kg m}^{-2} \text{ a}^{-1}$ at DML05, a sodium profile in 1 cm resolution and an annually resolved nss-sulphate record allowed us to count annual layers. We further introduce a sensitive peak detection algorithm, applied on the non-sea-salt(nss)-sulphate record and data from Dielectric Profiling (DEP). Because we additionally consider two other volcanic chronologies from the Atlantic sector of East Antarctica (Camp Victoria and Mizuho) based on DEP measurements, we specify the main ionic component causing the detected peaks in the DEP signal. We further discuss the representativeness of the imprint of volcanic eruptions from 15 snow pits and four intermediate deep ice cores representing the time period 1800 to 1997 A.D.

5.3 Methods

5.3.1 Site Selection, Sampling and Analyses

Site Selection

In the framework of the European Project for Ice Coring in Antarctica (EPICA) several comprehensive pre-site surveys have been carried out in DML [Oerter et al., 1999; Oerter et al., 2000]. Data from fifteen of the snow pits and four of the intermediate deep ice cores recovered during the field campaigns 1997/1998 and 1999/2000 (Figure 5.1) are presented here. The location, altitude, accumulation rate, studied time period and number of samples of each sampling site are presented in Table 5.1.

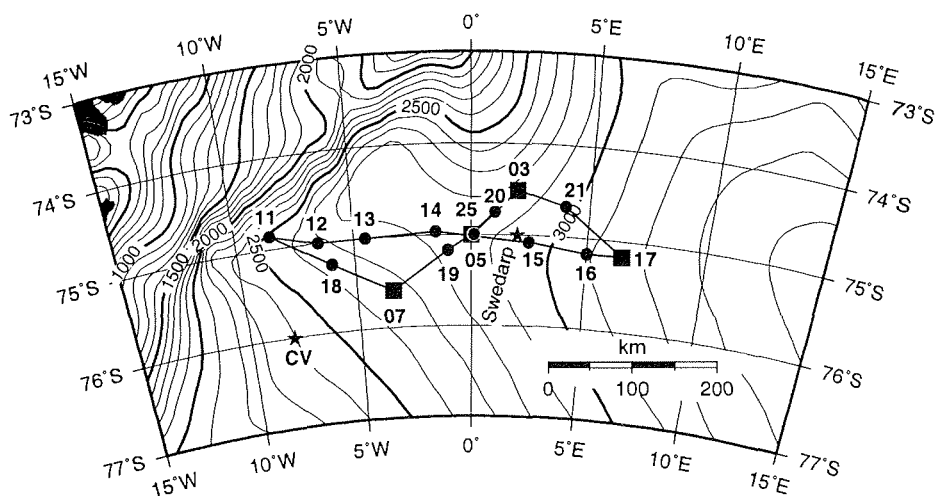


Figure 5.1: Area under investigation in DML.

Location of ice core (squares) and snow pit (dots) sampling sites. The stars mark two other ice cores studied in this area, Camp Victoria (located 130 km to DML07, and about 250 km to DML05) [Karlöf et al., 2000], and Swedarp [Isaksson, 1994]. The present EPICA deep drilling site is located at $0^{\circ}04.07'E, 75^{\circ}00.10'S$.

Sampling

The four intermediate deep ice cores at DML03, DML05, DML07 and DML17 (Table 5.1), were drilled with an electro-mechanical drill and the recovered core pieces were sealed in poly-ethylene (PE) bags, which were sealed immediately in the field. All snow pit samples (except SS9908) were filled in pre-cleaned PE-beakers. These beakers were rinsed with ultra-pure water, until the conductivity of the water was less than $0.5 \mu\text{S cm}^{-1}$. After cleaning, the beakers were dried in a contamination free vacuum oven and directly sealed in PE-bags until usage in the snow pit. The PE-beakers were pushed in the snow pit wall slightly overlapping the same snow layer. After sampling the beakers were sealed for transportation. All ice core and snow pit samples were transported in frozen state to the cold room facility of the Alfred Wegener Institute at Bremerhaven, Germany.

Table 5.1: Overview of sampling sites.

The geographic position, altitude, accumulation rate, investigated time period and number of samples of each sampling site are presented. FB9809, B31, B32 and B33 are ice cores and SSxxxx denote snow pits. All ice cores and snow pits starts in December 1997 and cover the number of years back in time, except for snow pit SS9908, which starts on December 1999.

Sample Label	Sample Site	Latitude	Longitude	altitude [m. a.s.l.]	accum. rate [kg m ⁻² a ⁻¹]	no. of years	no. of samples
FB9809	DML03	74°51'S	1°97'E	2843	89	200	570
B31	DML07	75°59'S	3°44'W	2669	59	1533	1886
B32	DML05	75°00'S	0°01'E	2882	62	1833	2216
B33	DML17	75°17'S	6°51'E	3160	47	200	390
SS9801	DML11	74°86'S	8°51'W	2600	76	9	40
SS9802	DML18	75°25'S	6°00'W	2630	55	10	40
SS9803	DML07	74°51'S	1°97'W	2669	62	10	47
SS9804	DML19	75°17'S	1°00'W	2840	78	11	52
SS9805	DML05	75°00'S	0°01'E	2882	71	10	70
SS9806	DML20	74°75'S	1°01'E	2860	97	8	40
SS9807	DML03	75°59'S	3°44'E	2843	89	4	24
SS9808	DML21	74°67'S	4°00'E	2980	83	9	40
SS9810	DML17	75°17'S	6°51'E	3160	63	14	40
SS9812	DML16	75°17'S	5°00'E	3100	70	7	29
SS9814	DML15	75°08'S	2°50'E	2970	71	8	38
SS9815	DML14	74°96'S	1°50'E	2840	81	9	42
SS9817	DML13	75°00'S	4°51'E	2740	80	10	42
SS9818	DML12	75°00'S	6°51'E	2680	68	9	42
SS9908	DML25	75°00'S	0°01'E	2882	72	9	112

Analyses

In general, all snow pit samples were analysed for methane sulphonate (MSA), Cl⁻, NO₃⁻, SO₄²⁻, Na⁺, NH₄⁺, K⁺, Mg²⁺, and Ca²⁺ by ion chromatography (IC). The sampling procedure of the ice cores, the used decontamination routine, the used IC set up, accuracy and detection limit are described in detail by Göktaş [2002]. Ice core samples between 1950 and 1997 were analysed for all anion and cation species. On ice core samples assigned to years prior to 1950 only anions were analysed. The uncertainty for the measured sulphate concentrations discussed in this study is approximately 3%. In addition, continuous flow analyses (CFA) had been already carried out for all four ice cores during the field campaign 1997/1998 [Sommer et al., 2000b]. The nss-conductivity and the ions Na⁺, NH₄⁺, Ca²⁺ were measured by CFA, providing seasonal resolved records for annual layer counting. The samples of the ice cores corresponding to the time period 1950 to 1997 were sampled in 2 cm

resolution, and for these samples anion and cation analyses were performed using IC. To date the upper metres of the ice cores and the snow pit samples annual markers were set at the falling flank of the Na^+ profile and the rising flank of the non sea-salt (nss)-sulphate record, indicating the spring season [Göktaş, 2002]. Only the snow pit SS9908, which was sampled both for ion and isotope analyses in 2 cm resolution, dating was carried out by marking the summer maximum in δD for each year [Göktaş, 2002].

Prior to the year 1950, the ice cores were sampled in annual resolution, according to the stratigraphic dating of Sommer et al. [2000a]. These samples were analysed for anions while the sodium concentrations were taken from the CFA measurements. This could be done because of the good agreement between IC and CFA sodium measurements [Göktaş et al., 2002].

The value for nss-sulphate concentration ($[\text{nssSO}_4^{2-}]$) is calculated by subtracting the concentration of the sea-salt derived sulphate from the total sulphate concentration ($[\text{SO}_4^{2-}]$), using Na^+ as sea-salt reference species and the sulphate to sodium ratio in bulk sea water of 0.252, i.e.:

$$[\text{nssSO}_4^{2-}] = [\text{SO}_4^{2-}] - 0.252 \cdot [\text{Na}^+] \quad (5.1)$$

5.3.2 Identification of the volcanic signature

Numerous studies have been carried out to identify volcanic events in ice core time series [Delmas et al., 1985; Legrand and Delmas, 1987; Langway et al., 1988; Palais et al., 1990; Delmas et al., 1992; Langway et al., 1995; Karlöf et al., 2000]. For example, Langway et al. [1994] assigned distinct nss-sulphate peaks to volcanic events, without giving a measure for the background concentration. Delmas et al. [1992] and Karlöf et al. [2000] used the median value $\text{med}[\text{nssSO}_4^{2-}]$ plus 2 times the standard deviation (2σ) of the whole nss-sulphate record as threshold value expressed by:

$$y_{(lit)} = \text{med}[\text{nssSO}_4^{2-}] + 2\sigma \quad (5.2)$$

All nss-sulphate concentrations higher than $y_{(lit)}$ were taken as volcanic peaks and assigned to known, unknown (a volcanic eruption is documented but could not be named) or unidentified (eruption is not documented and is either seen the first time in the ice core record or has been seen already in other ice core records) volcanic eruptions in the corresponding time period covered by the ice core sample.

The disadvantage of these methods is that the standard deviation is not a robust measure of variability in the presence of volcanic peaks and longterm variation in the atmospheric background sulphate loading is not considered. Thus, even strong and

violent volcanic eruptions may not be detectable using these methods as demonstrated in Figure 5.2. For example, using $y_{(lit)}$ as threshold value, the signal in nss-sulphate of the eruption of Billy Mitchell (Bougainville) around 1030 A.D., classified with VEI 5+ and located in the South-West Pacific region [Simkin and Siebert, 1993], would be ignored.

Therefore, a more sensitive identification procedure is applied here which uses a robust measure of variability and takes long-term variation in the background concentration into account [Fischer, 1997]. We use the running median run_{med} to calculate background concentrations and the median of absolute deviation ($MAD = median|x_i - median(x_i)|$ for $i = 1, \dots, n$ and $n =$ window width). Peaks were detected if nss-sulphate concentrations exceeded the running threshold value y_r defined by:

$$y_r = run_{med} + k \cdot MAD \quad (5.3)$$

The parameter k adjusts the threshold, and $k=4$ was selected empirically in this study which seems to be most suited for peak detection in nss-sulphate records of ice cores from Antarctica as well as from Greenland [Fischer, 1997]. The run_{med} and MAD values for each year were calculated using a window width n of 30 years. In comparison, employing y_r instead of $y_{(lit)}$ as threshold on the whole time period, 80 peaks in the nss-sulphate record of ice core DML05 were detected, compared to 29 peaks using $y_{(lit)}$ (Figure 5.2).

Karlöf et al. [2000] identified 29 volcanic events in the time period 540 to 1997 A.D. in an ice core recovered at Camp Victoria (CV) in DML by using $y_{(lit)}$ as threshold value. An application of this method on ice core B31 at DML07 (located 130 km away from CV) produces 29 peaks and on ice core B32 at DML05 (located 250 km away from CV) 24 peaks for the same time period. In comparison, using y_r as threshold value 45 peaks in the ice core B31 and 67 peaks in the ice core B32 were detected for the time period 540 to 1997 A.D. Altogether, 40 peaks could be observed coincidentally in both ice core records. All peaks occurring in only one record but not in the other one have been disregarded. Finally, from 40 nss-sulphate peaks coinciding in both ice cores 34 could be assigned to known volcanic events and 6 are unidentified events, i.e. they could not be assigned to a documented volcanic eruption.

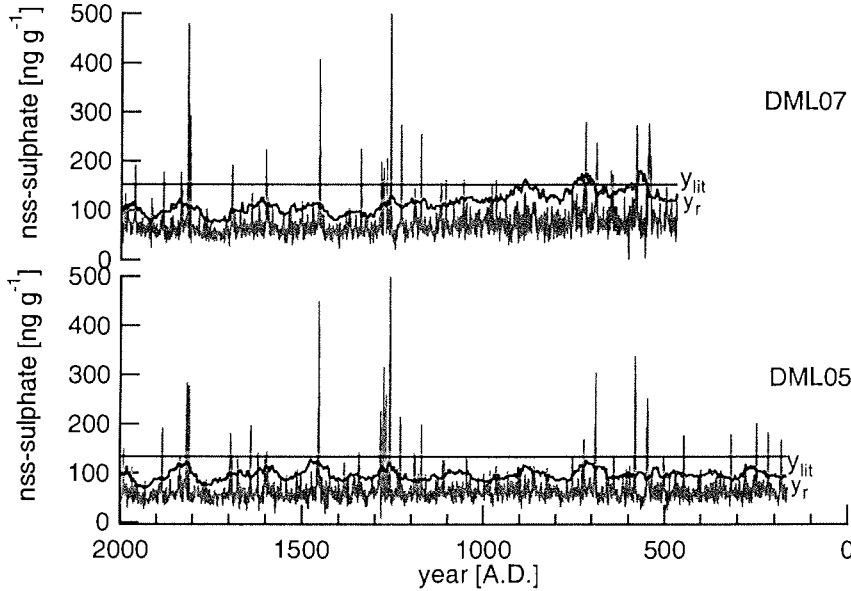


Figure 5.2: Identification of nss-sulphate peaks as volcanic events.

The nss-sulphate record (grey line), running median (lowest black line), y (mid black line), and y_{lit} (upper black line) versus assigned time scale of the ice core at DML05. The number of identified peaks using y_{lit} is less than that using y as threshold value.

5.3.3 Calculation of volcanic H_2SO_4 deposition

The total volcanic H_2SO_4 deposition ($(H_2SO_4)_{Depos.}$) of a volcanic eruption on the ice sheet was calculated according to:

$$(H_2SO_4)_{Depos.} = \sum_{i=1}^n ([nssSO_4^{2-}]_i - [nssSO_4^{2-}]_{mean}^{red}) \cdot \Delta z_i [kg km^{-2}] \quad (5.4)$$

by integration the part of a volcanic nss-sulphate peak above the running mean $[nssSO_4^{2-}]_{mean}^{red}$ where all identified volcanic peaks had been removed from the data set, with $[nssSO_4^{2-}]_i$ the total nss-sulphate concentration, and Δz_i the depth interval (in the unit m w.eq) of the volcanic influenced sample i .

The deposition value is strongly dependent on the chosen background value $[nssSO_4^{2-}]_{mean}^{red}$. Therefore, the following approach was taken to determine the uncertainty for volcanic H_2SO_4 deposition values. In addition to the running mean (window width $n=30$) the corresponding running standard deviation (σ_i) values were computed for the volcano reduced data set. The uncertainty of the deposition

values was determined according to:

$$\Delta(H_2SO_4)_{Depos.} = 2 \sum_{i=1}^n \sigma_i \cdot \Delta z_i [kg km^{-2}] \quad (5.5)$$

where 95% of all background concentration values are within two times the standard deviation σ_i ; multiplication of the depth interval (unit m w.eq.) by the concentration of 2σ value.

This method could not be applied on the data from the snow pits, due to the small number of years, disabling calculating representative mean values and standard deviations. As a approximation of the deposition values presented for the snow pits the uncertainties of known volcanic events observed in four ice cores were split into two groups representing the values found in the snow pit (group one: H_2SO_4 deposition higher $20 kg km^{-2}$, group two: between 10 and $20 kg km^{-2}$, and group three: values below $10 kg km^{-2}$). A relative mean error for group one was about 15%, group two about 50%, and group three about 75%, and in single cases even higher.

Altogether, the uncertainty for deposition values higher than $10 kg km^{-2}$ is 50% and less, but for deposition values below $10 kg km^{-2}$ an uncertainty of about 75%, in single cases even 100%, has to be taken into account. In summary this shows that volcanic events with depositions larger than about $10 kg km^{-2}$ can be reliably determined in DML and in return such volcanic deposition events are expected to be of comparable size all over the DML region.

5.3.4 Comparison of peaks in nss-sulphate and DEP

Soluble impurities effect also the electrical and dielectrical properties of ice cores [Looyenga, 1965; Gross et al., 1978]. In order to study the relationship between the abundance of ionic species and the electrical and dielectric properties of ice cores two stratigraphic electrical techniques have been developed. The electrical conductivity measurement (ECM) Hammer [1980] and the dielectric profiling (DEP) [Moore and Paren, 1987; Moore et al., 1992; Moore and Fujita, 1993; Wilhelms et al., 1998]. While the electrical conductivity depends on the acidic part of the solute [Hammer, 1980], the dielectric property is strongly dependent on the concentration of soluble impurities [Gross et al., 1978], however unambiguous transfer functions of impurity concentrations and DEP signal have not been established.

For preliminary dating striking peaks in the DEP record were assigned to volcanic events [Oerter et al., 2000], but the question remains whether all DEP peaks really indicate high nss-sulphate concentrations or might be related to high concentration

of other non-volcanic ion species. Comparison of the DEP data set with the nss-sulphate record clarifies this question. The nss-sulphate record shows 79 peaks at DML05 (47 peaks at DML07) by using y_r as threshold value while in the DEP signal only 53 peaks at DML05 (44 peaks at DML07) could be identified. Note, that due to reduced core quality data are missing in the DEP signal in certain intervals for the deeper parts (Figure 5.3). Therefore, 13 peaks (4 peaks at DML07) in the nss-sulphate record could not have a counterpart in the DEP signal.

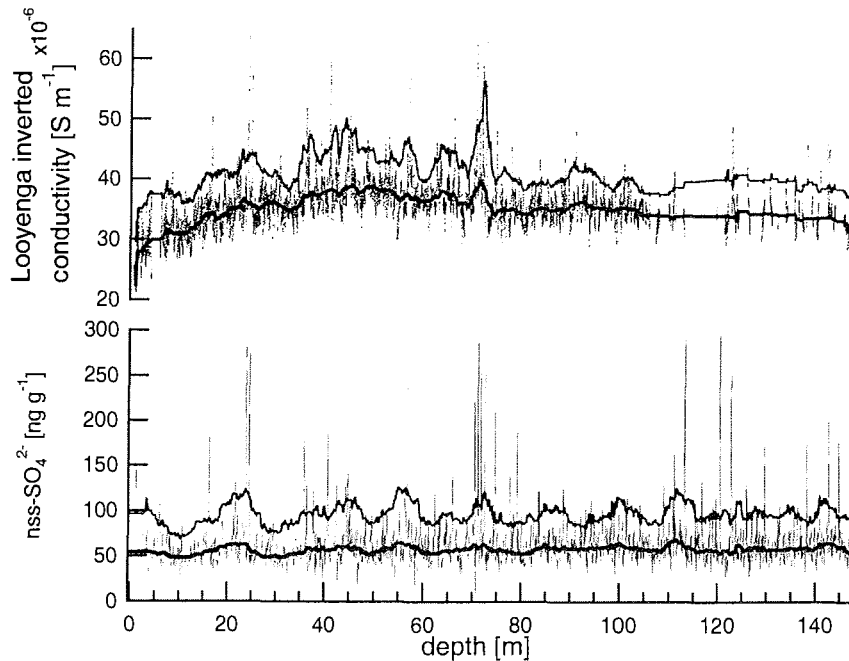


Figure 5.3: Comparison of DEP with nss-sulphate record.

Looyenga inverted conductivity [Oerter et al., 2000] and nss-sulphate record of ice core B32 at DML05, with corresponding running median and threshold values y_r .

For the part of the ice cores B32 at DML05 and B31 at DML07, where data were available from both DEP and IC measurements, 25 (11 at DML07) peaks in the nss-sulphate record caused no striking DEP signal. In these cases, the other anionic species and sodium did not provide a plausible explanation for the absence of the nss-sulphate peaks in the DEP signal. Concurrently with 40 peaks in the nss-sulphate record at DML05 (31 at DML07) a striking DEP signal was observed. This means that 75% of the peaks in the DEP record at DML05 and 70% at DML07 are caused by high nss-sulphate concentrations. We conclude that peaks in the DEP record have their origin dominantly in high concentration of the nss-sulphate component.

Thus, moderate and strong volcanic events are most probably well detected by DEP measurements in combination with a sensitive peak detection algorithm, however not all DEP peaks (about 25%) are necessarily of volcanic origin.

5.4 Results and discussion

5.4.1 Spatial variability of two recent volcanic signals

To assess the spatial variability of two recent volcanic signals within the area under investigation samples from 15 snow pits were studied. These samples enabled us to study the signal of the two well known volcanic eruptions in 1991, i.e. the Mt. Pinatubo eruption at June 15th, located on the Philippines, and the Cerro Hudson at August 8th, located in Chile. The eruption of Mt. Pinatubo was the strongest recorded in the past century, assigned to a VEI of 6, while that of Cerro Hudson was classified with a VEI of 5 [Simkin and Siebert, 1993]. Unfortunately, the snow pits excavated at DML03 and DML11 were too shallow to provide information about years prior to 1994. All other snow pits covered up to 14 years back in time ending at year 1999 (for DML25) or 1997 (remaining sites), respectively.

The nss-sulphate records of all snow pits are plotted versus depth in Figure 5.4. In all snow pits nss-sulphate concentrations increased at the end of 1991. Typically, elevated nss-sulphate concentrations persisting up to three years after major volcanic eruptions could be observed in other ice cores [Langway et al., 1994; Legrand and Wagenbach, 1999]. The mean nss-sulphate concentrations from 1992 to 1993 are plotted against the inverse accumulation rate for each snow pit (Figure 5.5), in order to distinguish the nss-sulphate contribution by dry deposition [Fischer and Wagenbach, 1998a]. In general, nss-sulphate concentrations increased with decreasing accumulation rates. For DML18, DML07 and DML19 the accumulation rate increases with altitude but it decreases for all other sites (Table 5.1). This finding supports the results presented in Göktaş et al. [2002] that sulphate is mainly removed by dry deposition from the atmosphere in DML. Linear regression between nss-sulphate concentration in [ng g^{-1}] and accumulation rate in [$\text{kg m}^{-2} \text{a}^{-1}$] results in:

$$[nssSO_4^{2-}] = (36 \pm 30) + (7031 \pm 2130) * accu^{-1} \quad \text{with} \quad r^2 = 0.705 \quad (5.6)$$

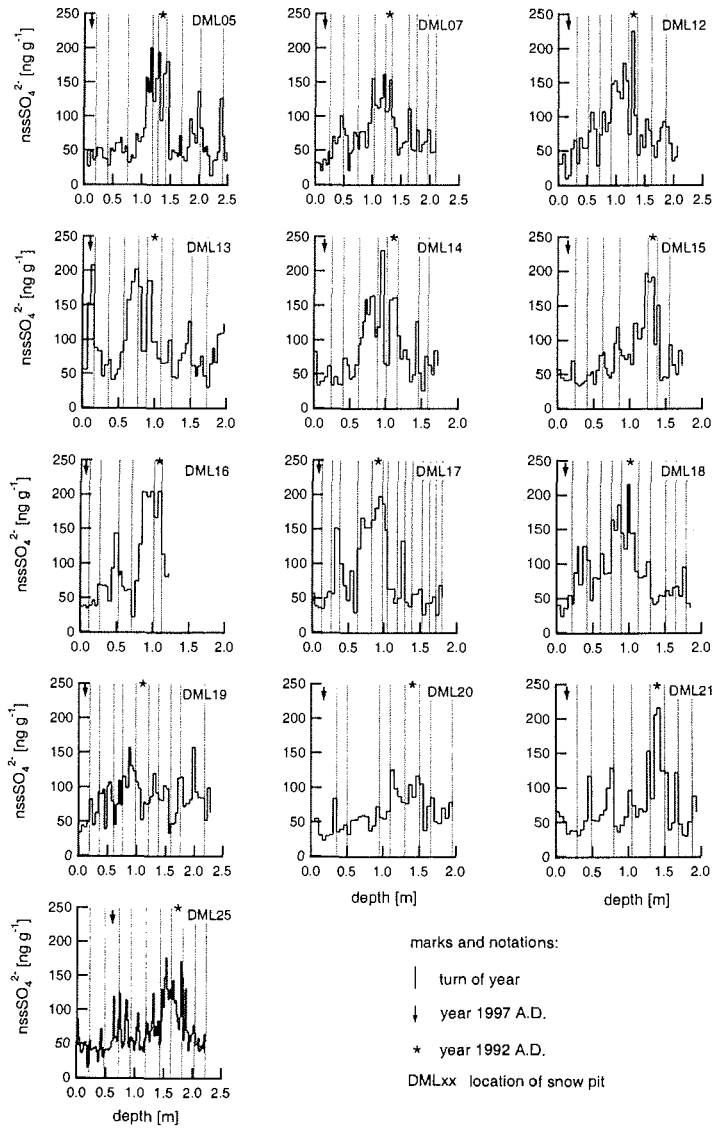


Figure 5.4: Fingerprint of volcanic eruption.

Record of nss-sulphate from all snow pits (table 5.1). The increase of concentrations is assigned to the eruptions of Mt. Pinatubo (June 15th, 1991) and Cerro Hudson (August 8th, 1991).

This relationship indicates that about 71% of the recent nss-sulphate removal is due to dry deposition and the correlation coefficient implies that about 70% of the spatial variability can be explained by the change in snow accumulation.

All deposition values are in the range between 8.2 kg km^{-2} (at DML18) and 18.4 kg km^{-2} (at DML17), except for the snow pits at DML19 (2.8 kg km^{-2}) and at DML20 (4.0 kg km^{-2}). These low values could be explained by local effects e.g. wind erosion removing a part of the snow deposited during 1992 and 1993. Considering the uncertainty for low deposition values with about 75% and even higher, deposition values in the range of the other snow pits could be reached easily at DML19 and DML20.

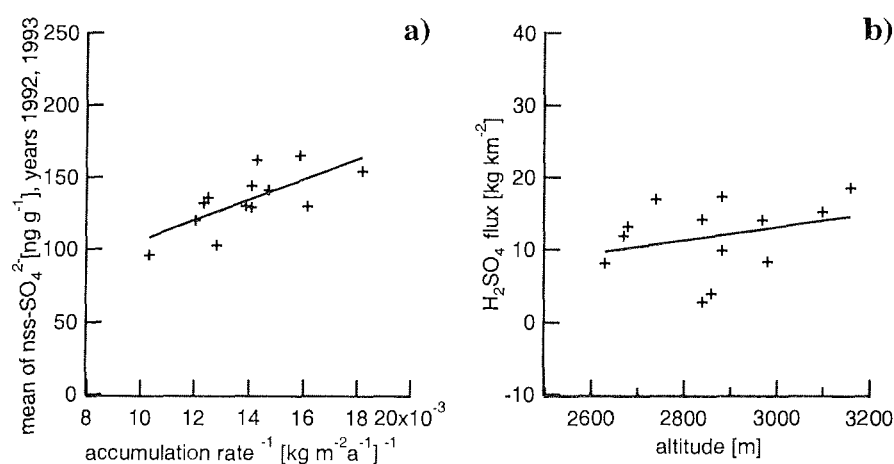


Figure 5.5: Spatial distribution of volcanic signal.

The mean nss-sulphate concentrations of the years 1992 and 1993 plotted versus inverse accumulation rate (a). The volcanic H₂SO₄ deposition is presented versus altitude (b).

Excluding DML19 and DML20 from further evaluation, for the remaining sampling sites the average H₂SO₄ deposition caused by the eruptions of Mt. Pinatubo and Cerro Hudson is about $13.4 \pm 3.5 \text{ kg km}^{-2}$ on Amundsenisen, DML. For South Pole, a site of similar altitude (2835 m [SCAR, 2002]) and only slightly higher mean accumulation rate ($80 \text{ kg m}^{-2} \text{ a}^{-1}$ [Delmas et al., 1992]), a comparable H₂SO₄ deposition of $14.15 \pm 1.65 \text{ kg km}^{-2}$ was determined for these two volcanic eruptions [Cole-Dai et al., 1997]. The almost uniform geographical distribution of the H₂SO₄ deposition, caused by the eruptions of Mt. Pinatubo and Cerro Hudson on Amundsenisen, verifies that any eruption of similar size should be well documented in the snow pack of the area under investigation. Accordingly, the volcanic chronology

at different sites can be cross-checked by comparing the calculated volcanic H_2SO_4 deposition at different sites.

5.4.2 Annual layer counting

[Oerter et al., 2000] carried out a preliminary dating based on DEP on all ice cores from Amundsenisen, using the striking volcanic horizon of Tambora as a marker for the year 1816 A.D. Dating based on radioactive horizons of nuclear weapon tests in the 1950s and 1960s, as used in an earlier study in this area [Oerter et al., 1999], was not performed. Stratigraphic dating was accomplished by Sommer et al. [2000a] using a combination of annual layer counting in the CFA records and identification of the most prominent historic volcanic horizons Tambora (1815), Kuwae (1452) and unknown volcanic events (1279, 1269, 1259) in the nss-conductivity profile [Sommer et al., 2000a]. As shown above, the latter are mainly related to high concentrations of sulphuric acid in the respective snow layers. In general, this dating method was adopted throughout this study. Only slight corrections of this dating were made according to our high resolution ionic profiles for the last 50 years [Göktaş et al., 2002]. This multi-parameter (sodium, calcium, ammonium, hydrogen peroxide and nss-conductivity) stratigraphic annual layer counting was performed for the first 900 years, from 1100 to 1997 A.D. However, beyond 1100 A.D. [Sommer et al., 2000a] used a combination of a dynamic model for firn densification and prominent peaks in the nss-conductivity in the years 687, 578, and 544 A.D. also observed in the DEP record at Dome C.

Here we extended the annual layer counting for the ice cores B32 (DML05) and B31 (DML07) beyond 1259 A.D. based on the high resolution CFA measurements of sodium [Sommer et al., 2000a]. To quantify the stochastic error of the counting procedure we repeated the counting four times in the two depth intervals from 105 m to 110 m, and from 135 m to 140 m. We found that counted years did not differ by more than ± 5 years for these 5 m intervals. In addition, annual layer counting was carried out four times beyond 1600 A.D. to the end of the ice core record where finally 165 ± 22 A.D. was obtained. Thus, the unknown eruption at 1259 is given with an uncertainty of ± 5 years in our record. Our stochastic error in annual layer counting increased linearly from ± 1 year at 1600 A.D. and ± 5 years at 1259 A.D., to ± 22 years at 165 A.D. A possible systematic dating error, e.g. by missing years, was estimated by annual layer counting between well defined volcanic reference horizons in the younger part of the core (1884-1815, 1815-1762, and 1762-1600 A.D.). Within these reference horizons, counting has been performed ten times. We found that our counting procedure led to no systematic error compared to the absolute number of

years between these historic eruptions. In conclusion, the assignment of the volcanic eruptions between 1600 and 1997 is within ± 1 year, between 1259 and 1600 A.D. about ± 5 years and from 165 to 1259 A.D. around ± 5 years at 1259 A.D. increasing linearly to ± 22 years to the end of the core.

Annual layer counting could not be performed on the complete record at DML07, due to the decreasing accumulation rate from $59 \text{ kg m}^{-2} \text{ a}^{-1}$ to $38 \text{ kg m}^{-2} \text{ a}^{-1}$ prior to 1000 A.D. The dating at DML07 was verified by using the synchronisation in the volcanic H_2SO_4 deposition values.

5.4.3 Spatial variability of historic volcanic signals

The study of the snow pit data showed that a certain volcanic event is well represented by distinct nss-sulphate concentration peaks and comparable volcanic sulphate deposition at all sampling sites on Amundsenisen. In the following we present a high resolution chronology of historic volcanic events archived in four intermediate ice cores (FB9809 at DML03, B32 at DML05, B31 at DML07 and B33 at DML17) covering the period from 1997 back to 165 A.D. The assignment of the volcanic events will be discussed along with identified volcanic impacts in other ice cores from Antarctica as well as from Greenland (Table 5.2).

Table 5.2: List of ice cores.

ice core	evaluated time period	method	reference
CV	540 to 1997 A.D.	ECM, DEP	[Karlöf et al., 2000]
Law Dome	1807 to 1995 A.D.	nss-sulphate	[Palmer et al., 2001]
South Pole	970 to 1984 A.D.	nss-sulphate	[Delmas et al., 1992]
Dome C	1800 to 1978 A.D.	nss-sulphate	[Legrand and Delmas, 1987]
Siple	1400 to 1986 A.D.	nss-sulphate	[Cole-Dai et al., 1997]
Dyer Plateau	1590 to 1990 A.D.	nss-sulphate	[Cole-Dai et al., 1997]
Byrd	850 to 1968 A.D.	nss-sulphate	[Langway et al., 1994]
Mizuho	1200 to 1984 A.D.	DEP	[Moore et al., 1991]
GISP2	5000 B.C. to 1993 A.D.	nss-sulphate	[Zielinski et al., 1997]
Crête	1770 to 1972 A.D.	spec. conductivity	[Hammer, 1977]

The time period 1800 to 1997 A.D.

In this period six volcanic signals in FB9809, nine in B32, ten in B31 and B33 are discussed Table 5.3. The mean accumulation rates for these sites decrease from $89 \text{ kg m}^{-2} \text{ a}^{-1}$ at DML03 to $47 \text{ kg m}^{-2} \text{ a}^{-1}$ at DML17 (see Table 5.1), what might cause dilution of the nss-sulphate signal at DML03 compared to DML17. For the same

time period seven peaks were observed in the ice core from CV [Karlöf et al., 2000] using $y_{(tit)}$ (eq. 5.2) as threshold value.

The imprint of the eruptions from Mt. Pinatubo and Cerro Hudson (peak 1) was discussed in detail in the previous section. About 30%-40% of the volcanic sulphate in the atmosphere between 1991 and 1993 can be attributed to the weaker but closer located eruption of Cerro Hudson as revealed by studies at Neumayer Station and Dumont d'Urville [Legrand and Wagenbach, 1999]. That indicates that most probably the eruption of Cerro Hudson (assigned to VEI 5) had a relatively stronger influence on Amundsenisen than the eruption of Mt. Pinatubo (assigned to VEI 6).

Table 5.3: Volcanic H_2SO_4 deposition and assigned eruptions from 1997 to 1800. Also given are the identification of the events in an ice core recovered at Camp Victoria (CV) by Karlöf et al. [2000] (nd - no sample available, no - no peak detected, x - peak detected, unid - unidentified peaks). Name, location and VEI of volcanic eruptions taken from Simkin and Siebert [1993].

no.	year of erupt. [A.D.]	volcano	VEI	year of depos. [A.D.]	DML05 [kg km ⁻²]	DML07 [kg km ⁻²]	DML17 [kg km ⁻²]	DML03 [kg km ⁻²]	CV
1	1991	Cerro Hudson, Chile	5	1992	17.3±7.9	11.9±2.5	19.1±5.9	nd	x
		Mt. Pinatubo, Phil.	6	1992					
2	1982	El Chicon, Mex.	4	no	3.4±4.9	2.2±2.4	2.8±3.5	2.4±4.5	no
3	1970	Deception Is., Ant.	3	1969	5.1±3.4	no	1.6±2.3	1.6±2.5	x
4	1963	Agung, Indon.	4	no	no	10.7±2.9	9.6±3.7	5.1±7.3	no
5	1932	Cerro Azul, Chile	5	1932	2.3±1.2	0.6±3.3	1.6±2.9	2.8±3.4	x
6	1889	Colima Volc., Mex.	4	1889	1.5±1.5	1.8±1.3	1.8±2.9	1.4±1.2	no
7	1886	Tarawera, New Zeal.	5	1886	4.5±2.3	3.5±1.7	2.4±0.8	4.9±2.0	no
8	1883	Krakatau, Indon.	6	1884	9.7±2.5	12.4±2.7	5.5±1.9	5.6±2.9	x
9	1835	Coseguina, Nic.	5	1835	5.4±4.3	11.1±3.6	4.3±3.7	7.8±5.6	unid.
10	1815	Tambora, Indon.	7	1816	32.5±7.0	54.6±5.5	49.8±7.1	47.3±7.7	x
11	1809±2	unknown		1809	15.4±8.3	27.5±3.4	24.6±3.2	35.8±7.0	x

We assign peak 2 to the eruption of El Chicon, in 1982, which is missing in the nss-sulphate records at the sites DML03 and DML05. The calculated volcanic H_2SO_4 deposition varied between 2.1 kg km⁻² and 3.7 kg km⁻² (Table 5.3). This indicates that at DML03 and DML05 a locally increased accumulation rate could have diluted the nss-sulphate beyond detectability. Interestingly this eruption was not reported in other studies on Antarctic ice cores (Table 5.2, except Law Dome [Palmer et al., 2001]), indicating a comparably lower impact on the sulphate budget of the global atmosphere.

Concurrently with peak 3, in all four ice cores maxima in the MSA concentration were detected. Although the MSA peaks were very high, the nss-sulphate concentration peaks could hardly be detected even with our sensitive algorithm. In comparison, in none of the other glacio-chemical studies of Antarctic ice cores a significant nss-sulphate peak could be found, while ECM and DEP records from CV and Mizuho revealed a distinct peak in the corresponding year. We conclude that most probably high biogenic MSA and nss-sulphate concentrations caused the respecting ECM and DEP peaks and not a volcanic event.

The eruption of Agung in 1963 (peak 4) is well detected in the glacio-chemical records of the ice cores from the sites DML07 and DML17, and by using $k = 3$ it was also possible to identify this peak at DML03. Although this eruption was not detected in the ice core from CV, it is well represented at Siple Station (33 kg km^{-2}), Dyer Plateau (13 kg km^{-2}), Byrd (7 kg km^{-2}), South Pole (9.1 kg km^{-2}), Dome Concordia, Law Dome, and Mizuho. Oerter et al. [2000] could discern this event by ECM and DEP in seven out of twelve intermediate deep ice cores from Amundsenisen. We assigned peak 5 to the eruption of Cerro Azul in 1932 A.D., which is absent in all the other Antarctic ice core records listed in Table 5.2, except in the core from CV. The calculated volcanic H_2SO_4 deposition was quite low, indicating that this eruption is probably over-classified with a VEI of 5. The eruption of the Colima Volcano Complex in 1889 A.D. (peak 6) is only discernible by using $k = 3$ but is also found in the record from Byrd.

Peaks 7-11 are well represented in our and in all ice cores from Antarctica and Greenland listed in Table 5.2. However, peak 7 and 9, assigned to the eruption of Tarawera (in 1886) and Coseguina (in 1835) were not found at CV. At least one reason for the absence of peak 7 could be a super-imposition by the strong volcanic eruption of Krakatau in 1883 in combination with a less sensitive peak detection algorithm. The mean sulphate deposition caused by the Krakatau eruption (peak 8) was 9.6 kg km^{-2} on Amundsenisen and is in good agreement with values determined in ice cores from South Pole (8.2 kg km^{-2} and 9.4 kg km^{-2}), Byrd (14 kg km^{-2}), and Siple (12 kg km^{-2}). A striking horizon for all ice cores is the eruption of Tambora in the year 1815 (peak 10) and that of an unknown volcano in 1809 (peak 11). The volcanic H_2SO_4 deposition due to the Tambora eruption at Amundsenisen (45.6 kg km^{-2}), South Pole (72.3 kg km^{-2} and 67.6 kg km^{-2}), Byrd (24 kg km^{-2}), Siple (133 kg km^{-2}), and Dyer Plateau (90 kg km^{-2}) reflect the enormous strength of this eruption. The nss-sulphate deposition caused by the eruption in 1809 was about 55 kg km^{-2} at Amundsenisen, 29.8 to 32 kg km^{-2} at South Pole, 11 kg km^{-2} at Byrd, 54 kg km^{-2} at Siple and Dyer Plateau and thus significantly lower.

The time period 1600 to 1800 A.D.

While peak 12 could clearly be assigned to the eruption of the volcano Planchon-Peteroa in year 1691 A.D. (located in Chile), two volcanic eruptions, that of Teon (Indonesia) and Cotopaxi (Ecuador), may have caused peak 13 in 1695 A.D. Both volcanoes are located in the tropics close to the equator and classified with VEI 3. The signal in the ice cores is most probably caused by the impact of both eruptions. The mean volcanic H_2SO_4 deposition at Amundsenisen (25.5 kg km^{-2}) and the dating of the peak (this work: 1695/98 A.D.) is in good agreement with that from Siple (43 kg km^{-2} , 1695/96 A.D.), Dyer Plateau (24 kg km^{-2} , 1696/97 A.D.), and Law Dome (1695 A.D.). Accordingly, the classified VEIs seem to be too low compared to the VEIs of other eruption with similar deposition values or extraordinarily high sulphur injections into the stratosphere took place.

The distinct peaks 14 and 15 could be unambiguously assigned to the eruption of Reventador (Ecuador) and Gamkonora (Indonesia), respectively. A combination of violent eruptions (peaks 13, 16, and 17) observed in this century and a less sensitive peak detection algorithm may have impeded the identification of these events in other Antarctic ice core records. Peaks 16 and 17 were again generally detected in the Antarctic and Greenland ice core records listed in Table 5.2. Both, the eruptions of Awu (with VEI 5 and located at $12^\circ 50' \text{E } 3^\circ 67' \text{N}$) or Llaima (with VEI 4 and located at $71^\circ 73' \text{W } 38^\circ 69' \text{S}$) could have contributed to peak 16.

The time period 165 to 1600 A.D.

The significant peak 17, assigned to the eruption of Huyanaputina (Peru) in 1600 A.D., is the last known eruption with exact known date. Beyond 1600 a more accurate dating of the volcanic eruptions is performed by the applied annual layer counting. The mentioned years are the dates assigned in the ice core DML05 and are listed with the corresponding uncertainties in Table 5.4.

Peaks 18 - 20 were identified in all ice cores, except in the cores from Byrd Station and Siple Station, where the eruption of Ruiz (VEI 4) and Arenal (VEI 4), respectively, are missing. These volcanoes are located between 6°N and 10°N , so it is not obvious which eruption is not archived in the corresponding core. On the other hand, the much stronger eruption of Kuwae (peak 20) is a striking dating horizon in ice cores from Antarctica and Greenland. Peak 21 was also found in the Byrd ice core record, but could not be assigned to a known volcanic eruption. A far located prominent eruption should be detectable in other ice cores as well. Considering the volcanic H_2SO_4 deposition on Amundsenisen (4.4 kg km^{-2} in ice core B32 at DML05 and 2.3 kg km^{-2} in B31 at DML07) it seems that a local volcanic eruption like Deception Island, Bristol Island or Mt. Erebus might be responsible for this

peak.

Table 5.4: Volcano chronology and H₂SO₄ deposition from 1800 to 165
 Also given are the identification of the events at Camp Victoria (CV) by Karlöf et al. [2000]
 (nd - no sample available, no - no peak detected, x - peak detected, unid - unidentified peaks).
 Name, location and VEI of volcanic eruptions taken from Simkin and Siebert [1993].

no.	year of erupt. A.D.	volcano	Location	VEI	DML05 year of depos.	DML05 flux [kg km ⁻²]	DML07 flux [kg km ⁻²]	CV
12	Dec. 1762	Planchon-P.	Chile	4	1762±1	4.1±4.9	7.0±3.6	x
13	1698 ?	Cotopaxi	Ecuador	3	1695±1	24.0±9.7	28.2±6.9	unid.
14	1691 ?	Reventador	Ecuador	3	1691±1	5.6±3.2	1.8±1.0	no
15	May 1673	Gamkonora	Indonesia	5?	1676±1	7.4±5.2	3.5±1.9	x
	1660±20	Long Island	New Guinea	6				
16	Jan. 1641	Awu	Indonesia	5	1640±1	15.1±3.9	12.1±6.6	x
	1641±20	Deception Is.	sub. Ant.	?				
	Feb. 1640	Llaima	Chile	4				
17	Feb. 1600	Huyanaputina	Peru	6?	1601±1	11.5±9.0	24.8±6.8	x
18	March 1595	Ruiz	Colombia	4	1596±1	14.2±6.4	10.7±6.6	no
19	1525±20	Arenal	Costa R.	4	1542±2	6.7±7.7	4.4±3.7	x
20	1452±10	Kuwae	SW Pacific	6	1453±3	47.0±7.5	38.1±6.8	x
21		unid.			1376±3	4.3±2.8	3.8±2.8	no
22	1325±75	Cerro Bravo	Colombia	4	1343±4	13.1±4.2	20.8±4.9	x
23		unid.			1285±5	24.3±4.9	12.3±5.7	x
24	1279±10	unknown			1278±5	24.9±3.7	9.2±3.5	x
25	1269±10	unknown			1269±5	18.1±4.7	13.4±6.4	x
26	1259±10	unknown			1258±5	74.3±6.0	58.5±10.3	x
27		unid.			1229±5	18.4±4.2	23.7±5.7	x
28	1180±20	Tarawera	New Zeal.	5	1189±6	16.4±4.8	13.5±5.6	unid.
29	1176±16	unknown			1171±6	16.9±3.0	17.8±4.2	x
30		unid.			1111±7	6.8±2.8	5.6±2.5	no
31		unid.			1108±7	5.2±2.7	5.5±1.7	no
32	1050±25	Cerro Bravo	Colombia	4	1046±8	8.6±3.3	9.7±5.7	no
33	1030±150	Billy Mitch.	SW Pacific	5+	981±9	5.7±2.4	3.2±1.5	no
34	950 ?	Ceboruco	Mexico	5	965±10	5.7±2.5	3.7±1.6	no
35	750±150	Cerro Bravo	Colombia	4	721±13	8.1±3.8	11.1±4.1	no
36		unid.			688±14	35.9±8.7	21.6±7.6	no
37		unid.			652±14	2.3±1.6	5.9±2.7	no
38	639±25	unknown			638±15	9.1±3.4	4.2±1.6	x
39		unid.			581±16	37.5±7.0	27.4±10.6	no
40	540±100	Rabaul	SW Pacific	6	546±17	29.2±6.3	43.9±15.6	x
41		unid.			500±17	12.3±5.5	8.1±5.9	nd
42		unid.			399±18	3.9±2.7	nd	nd
43		unid.			345±19	4.6±3.6	nd	nd
44		unid.			317±20	9.5±3.1	nd	nd
45	280±20	Pelee	W Indies	4	278±21	7.4±5.3	nd	nd
46	260±100	Ilopango	Ecuador	6	247±22	16.7±4.7	nd	nd
47		unid.			216±22	14.0±2.9	nd	nd
48	180 ?	Taupo	New Zeal.	6+	181±22	16.0±4.1	nd	nd

Peaks 22-27 were detected in our ice core records, CV and Byrd. At South Pole the peaks 23 (1285 A.D.) and 27 (1229 A.D.), were most probably masked by three strong volcanic events in this century. The volcanic H_2SO_4 deposition derived from peak 26 is among the largest observed at this age with about 73.4 kg km^{-2} at DML05, 57.3 kg km^{-2} at DML07, 135.7 kg km^{-2} at South Pole, and 54 kg km^{-2} at Byrd Station. Among peaks 28-31 peak 29, exhibiting the highest sulphate deposition, was also detected in the records from CV, South Pole and Byrd Station. The other peaks could be exclusively detected in our ice cores and in that from South Pole showing comparable nss-sulphate deposition values. The eruptions of Cerro Bravo and Billy Mitchell are the only plausible candidates responsible for peaks 32 and 33. Delmas et al. [1992] identified these peaks in an ice core from South Pole. However, Langway et al. [1994] detected one peak at Byrd dated in 865 A.D., which is not observed in our records. Peaks 34-38 could be assigned to volcanoes located between 20°N and 40°S with VEI of 4 or higher. Simkin and Siebert [1993] reported two eruptions, that of Ceboruco and Cerro Bravo at this time period. Amongst peaks 39-41 only peak 40 could be assigned to the strong volcanic eruption of Rabaul, located in Papua New Guinea. Peaks 42-48 correspond to nss-sulphate depositions between 3 kg km^{-2} and 16.7 kg km^{-2} indicating volcanic events. Considering the correlation between the volcanic events and ice core dating the eruptions of Pelee (West Indies), Ilopango (Ecuador) and Taupo (New Zealand) could be assigned to the detected peaks.

5.4.4 Implications for snow accumulation rates and post - depositional processes

Supported by the accuracy in dating achieved for our ice cores, the dating of our ice cores implies a significant temporal change in accumulation rate at DML07 prior to 1000 A.D. (Figure 5.6), as already suggested by Sommer et al. [2000a]. Such a change, however, is neither observed at DML05 nor at Camp Victoria (CV), assuming that the dating by Karlöf et al. [2000] is correct. Considering that DML07 is located between DML05 (distance: 120 km) and CV (distance: 130 km), and on the same side of the ice divide as CV, the change in snow accumulation at DML07 appears to be a local phenomenon. Any systematic dating errors for the ice cores at DML05 and DML07 can be ruled out due to the precise synchronisation of our volcanic H_2SO_4 deposition values.

In addition, most pronounced changes prior to 1000 A.D. are not only observed for accumulation rate at DML07, but as presented in Figure 5.7 and Figure 5.8 also for $\delta^{18}\text{O}$, the deuterium excess ($d = \delta D - 8 \cdot \delta^{18}\text{O}$), as well as MSA and nss-sulphate

records, which are not sensitive to the dating.

The apparent increase in $\delta^{18}\text{O}$ prior to 1000 A.D. can be either due to a net increase in mean annual temperature or a lack of winter snow. A net warming only confined to DML07 but not encountered at DML05 or CV is, however, rather unlikely. Instead, a lack of winter snow could readily explain the isotope variations, leading to lower net accumulation rates, higher precipitation weighted mean stable isotope contents and lower deuterium excess values (Unpublished data from a snow pit at DML25 (close to DML05) show for the uppermost annual layers an anti-correlation of the $\delta^{18}\text{O}$ content and deuterium excess).

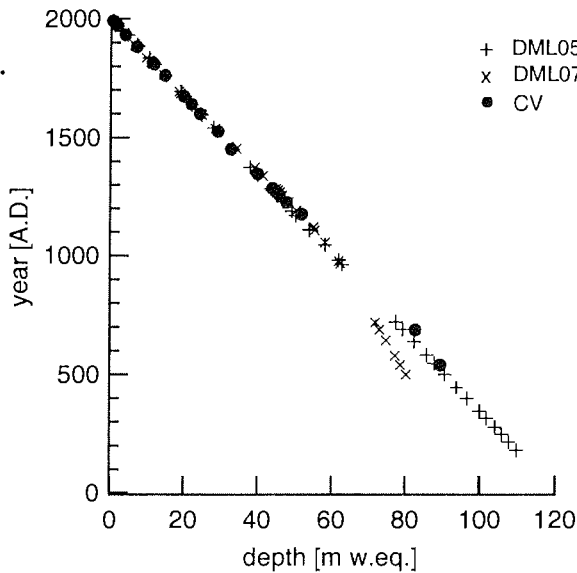


Figure 5.6: Age to depth relation for DML05, DML07, and CV.

The presentation is based on our volcano chronology. For the ice core from CV the assignment proposed by Karlöf et al. [2000] was adopted.

In addition, such a loss of winter snow results in higher mean annual nss-sulphate concentration. We observed an increase of 33% in nss-sulphate concentration in the time interval 540 and 688 (accumulation rate $38 \text{ kg m}^{-2} \text{ a}^{-1}$) compared to the time period 1000 to 1997 A.D. (accumulation rate $59 \text{ kg m}^{-2} \text{ a}^{-1}$). The accumulation effect itself would cause an increase of already 42 % in the nss-sulphate concentration as shown above. In case of MSA, post-depositional effects which are more pronounced at sites with lower accumulation rates [Wagnon et al., 1999] may have led to the observed net loss. A lack of winter snow could be provoked by a net

change in the seasonality of precipitation or wind scouring of winter snow layers.

An absolute proof of this process can not be definitely given here and is also beyond the scope of this work. However, the similar depth versus age relation for the sites DML05 and CV (Figure 5.6) supports local wind scouring effects at DML07. Nevertheless, a re-evaluation of the dating and an additional glacio-chemical investigation of the ice core from CV would be insightful. In this context it should be noted that Karlöf et al. [2000] have assigned the second last striking peak in their DEP record to the year 639 A.D. However, this horizon shows in our ice cores relatively low nss-sulphate and sulphate deposition values. Considering the fact that striking peaks in our DEP signal could be clearly attributed to high concentration of nss-sulphate and high sulphate deposition values, we recommend a revision of the dating of the ice core from CV and would assign that peak to year 688 A.D. Such a re-assignment would entail a corresponding decrease in accumulation rate from 68 to 46 kg m⁻² a⁻¹ at CV, which would be in agreement with the value verified at DML07.

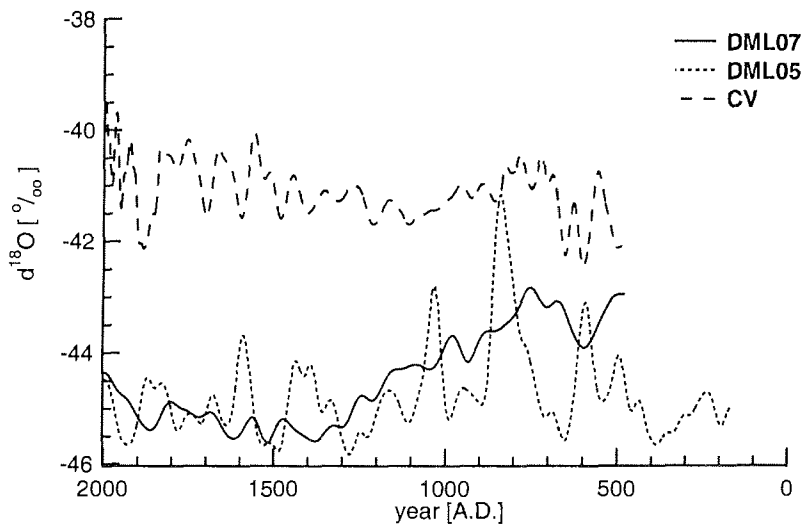


Figure 5.7: $\delta^{18}\text{O}$ profiles from DML05, DML07 and CV.

The Gaussian mean $\delta^{18}\text{O}$ values over 30 years are presented. DML07, which is located between DML05 and CV shows an increase in the $\delta^{18}\text{O}$ content beyond 1300. Results from CV are presented with the dating of Karlöf et al. [2000].

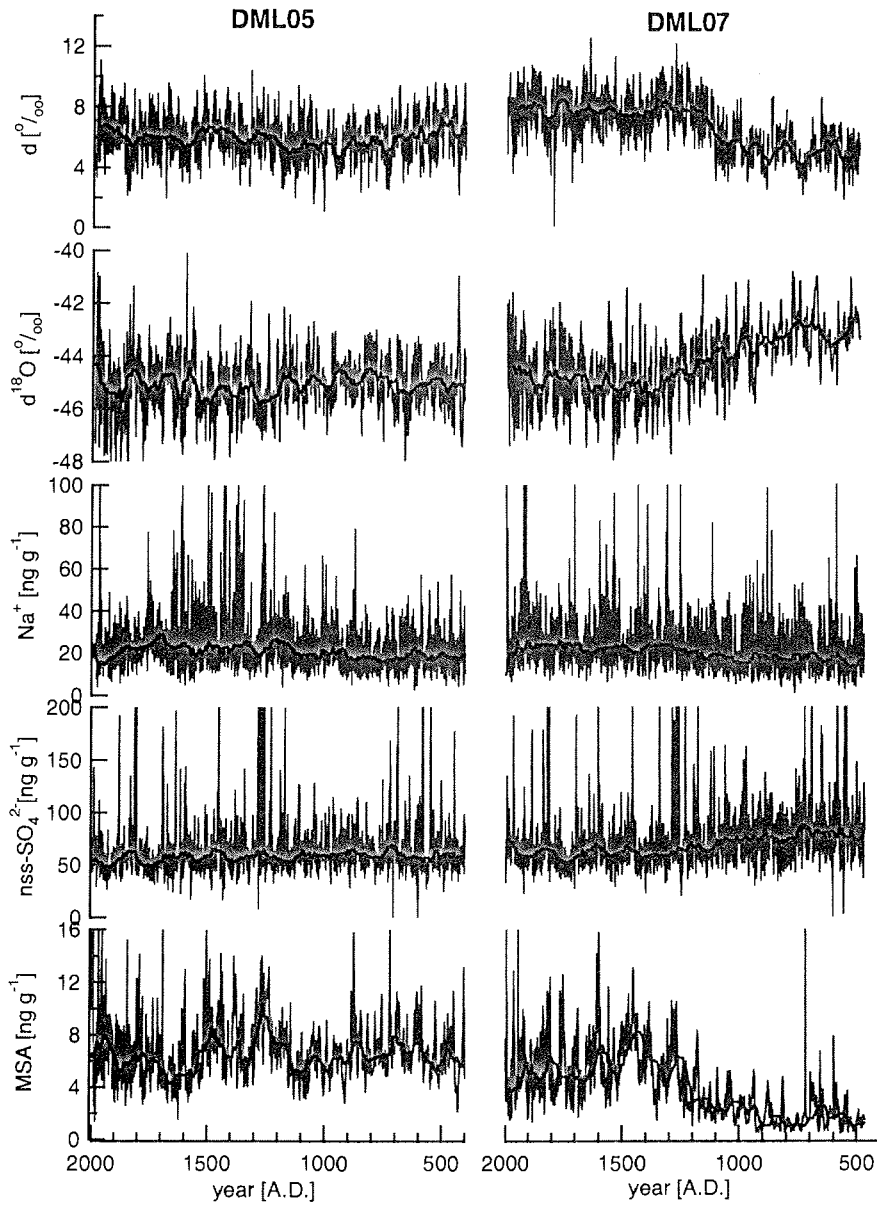


Figure 5.8: Ionic composition, $\delta^{18}\text{O}$ and deuterium excess for B31 at DML07 and B32 at DML05.

5.5 Conclusions

Our results from 13 snow pits and four intermediate deep ice cores covering the past 200 years revealed an uniform volcanic H_2SO_4 deposition pattern for Amundsenisen. With a combination of high resolution annual layer counting and volcanic H_2SO_4 deposition values we could provide a unique volcanic chronology covering the period from 165 to 1997 A.D. The dating accuracy of the corresponding volcanic eruptions could be improved to ± 1 years between 1600 to 1997 A.D., ± 5 years between 1600 to 1259 A.D., linearly increasing to ± 22 at 165 A.D. Especially beyond 1600 previous chronologies exhibited a two to ten times higher uncertainty. The presented accurate chronology of 41 volcanic eruptions in the time period between 465 and 1997 A.D. should especially improve the dating of further Antarctic ice cores.

Based on the reliability of our dating and on additional support from ionic as well as $\delta^{18}\text{O}$ and deuterium excess records, an accumulation rate discontinuity in the ice core from DML07 was ascertained. This finding points either to increased wind scouring and/or a persistent change in accumulation rate prior to 1000 A.D. confined to DML07.

In view of the present deep ice core drilling activities on Amundsenisen in the framework of EPICA, a high resolution volcanic chronology for the entire Holocene can be expected. Taking into account our results from the low accumulation site DML07, annual layer counting is most probably not feasible for the last glacial maximum for the EPICA core, which is currently drilled about 2 km east of DML05, because accumulation rate were most certainly significantly reduced during this period.

5.6 Acknowledgements

This work is a contribution to the "European Project for Ice Coring in Antarctica" (EPICA), a joint ESF (European Science Foundation)/EC scientific programme, funded by the European Commission and by national contributions from Belgium, Denmark, France, Germany, Italy, the Netherlands, Norway, Sweden, Switzerland and the United Kingdom. This is EPICA publication no. XXX. Financial support by Deutsche Forschungsgemeinschaft (project OE 130/3) is gratefully acknowledged.

Chapter 6

Seasonal and Spatial Variation

6.1 Abstract

In the framework of the European Project for Ice Coring in Antarctica (EPICA) a glacio-chemical pre-site survey was carried out in Dronning Maud Land (DML), Antarctica to investigate seasonal and spatial variations. All ion species show pronounced seasonal cycles with exception of nitrate, which is subject to post-depositional alterations. Sea-salt reaches maximum concentrations in late winter/spring, while sulphate being mainly of marine biogenic origin shows a double-peak with high concentrations both in autumn and late spring/summer. Methane sulphonate (MSA) shows also a strong autumn peak but only slight indications of a second peak in late spring/summer as seen for sulphate. Due to post-depositional changes the seasonal cycle of MSA vanishes further down in the firn. These changes are also reflected in the spatial distribution of MSA. While surface MSA concentrations decline with altitude and higher accumulation rates, concentrations of aged snow show a strong increase with higher accumulation rates in our ice cores. Non-sea-salt sulphate shows a 40% decrease with an increase in snow accumulation of about 80% in recent and aged snow. While the geographical variation is negligible for average nitrate concentrations, sea-salt shows an exponential decline with altitude. The outcome of this study supports that the data of the new EPICA deep drilling site in DML (0°04.07'E, 75°00.10'S) will be representative for this region and high-resolution analytical methods will allow accurate stratigraphic dating of a deep ice core.

This chapter is based on: Gøktas, F., H. Fischer, H. Oerter, R. Weller, S. Sommer, and H. Miller. A glacio-chemical characterisation of the new EPICA deep drilling site on Amundsenisen, Dronning Maud Land, Antarctica. *Ann. Glaciology* 35, 2002, in press.

6.2 Introduction

Among the various natural climate archives (such as tree rings, corals, sea and lake sediments) ice cores play a unique role since they do not only store information about temperature and precipitation but also about atmospheric composition and transport [Stauffer, 1999]. To obtain such long-term records several deep ice core drilling projects have been carried out in Greenland and Antarctica. Two new deep cores will be drilled in the framework of the European Project for Ice Coring in Antarctica (EPICA). One of those drillings will take place in Dronning Maud Land (DML), in the Atlantic sector of the East Antarctic plateau (Figure 6.1). This region is mainly influenced by air masses originating from the Southern Atlantic Ocean [Noone et al., 1999; Reijmer, 2001a]. Accordingly, the DML deep core is expected to provide the first southern Atlantic counterpart to the Greenland ice core records over the last glacial cycle and may give crucial information about the climate coupling of both hemispheres across the Atlantic.

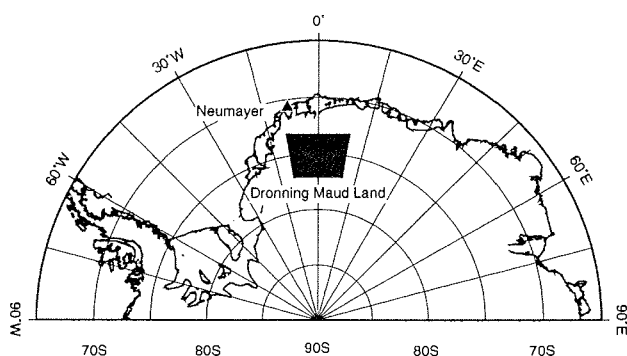


Figure 6.1: Dronning Maud Land in Antarctica.

Overview over Antarctica from 90° W to 90° E, indicating the study area.

In order to study the glacio-chemical and glacio-meteorological characteristics of DML and to corroborate the interpretation of the coming deep ice core record, a comprehensive pre-site survey has been carried out in this yet unexplored area [Oerter et al., 1999; Oerter et al., 2000]. Up to now chemical analyses were performed on samples of four intermediate deep ice cores and fourteen snow pits taken during the field campaign 1997/1998 and 1999/2000 (Figure 6.2). Table 6.1 compiles the information about geographical location and accumulation rate for each sampling site. In this paper we present seasonal variations and the spatial distribution of chemical species measured by ion chromatography (IC). We interpret these in terms of seasonally changing source conditions, transport pathways and aerosol deposition

onto DML. Special emphasis will be put on the implications of these findings for the interpretation of the EPICA deep ice core to be drilled in this region.

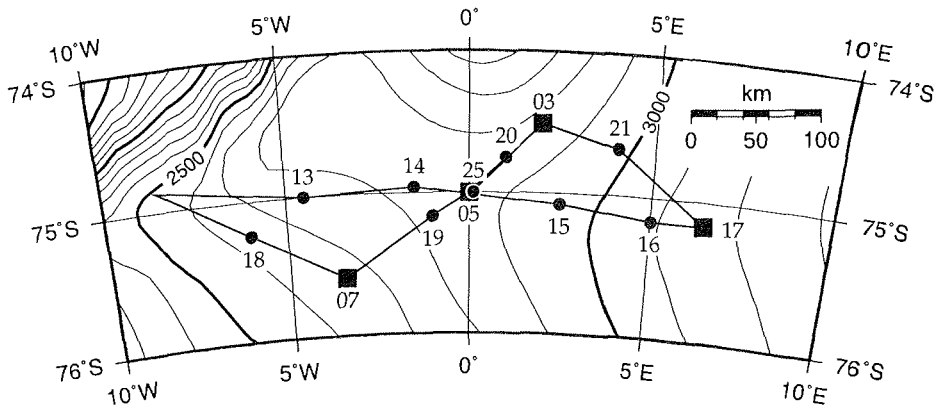


Figure 6.2: Investigated Area in DML.

Enlargement of the study area showing ice core drilling (squares) and snow pit (dots) locations [Oerter et al., 1999; Oerter et al., 2000].

6.3 Methods

6.3.1 Sampling

Intermediate deep ice cores were drilled and snow pit samples taken during the pre-site surveys in DML (Figure 6.2). The cores investigated here were drilled at the sites DML05, DML07 and DML17 are 150 m, 115 m and 130 m long, respectively, covering 1600-2000 years. At DML03 a firn core of 41 m length was drilled, covering more than 200 years. Because of the poor core quality of the uppermost metres of the cores, data for these depth intervals were taken from snow pits taken at the drill sites. Unfortunately, the snow pit at DML03 was too shallow, causing a gap of four years (1990-1993). Additionally, one snow pit (SS9908) located at the new EPICA deep drilling site in Dronning Maud Land was sampled with high resolution in the 1999/2000 field season.

Snow pits were sampled using 60 ml polyethylene (PE) beakers. All beakers were rinsed with ultra-pure water ($\sigma > 18 \text{ M}\Omega \text{ cm}$) until the electrical conductivity of water stored in the beakers dropped to values lower than $0.5 \mu\text{S cm}^{-1}$. After cleaning they were sealed in PE bags and only opened immediately before use in the snow pit. The beakers, having a diameter of 44 mm, were pushed into the snow pit

wall in depth intervals of 30-40 mm, thus slightly overlapping each other. For the snow pit SS9908 snow in defined 2 cm increments was collected in pre-cleaned 250 ml PE beakers using a pre-cleaned spatula. The beakers were closed very carefully and sealed again in PE bags for transportation back to Germany. The snow pits from the campaign 1997/1998 cover a time period of 4-14 years back in time starting from December 1997, the two from 1999/2000 cover 10 (SS9908) and 11 years (SS9901), respectively, starting from December 1999.

Table 6.1: Tabular list of sampling sites in DML.

Summary of the sampling sites in Dronning Maud Land listing sample label, coordinates, altitude and accumulation rate [Oerter et al., 1999; Oerter et al., 2000] for the snow pit and ice core locations.

label snow pits:	location	latitude	longitude	altitude [m a.s.l.]	accumulation rate [kg m ⁻² a ⁻¹]
SS9802	DML18	75°15.02' S	06°00.00' W	2630	55
SS9803	DML07	75°34.89' S	03°25.82' W	2669	62
SS9804	DML19	75°10.04' S	00°59.70' W	2840	78
SS9805	DML05	75°00.14' S	00°00.42' E	2882	71
SS9806	DML20	74°45.04' S	00°59.99' E	2860	97
SS9807	DML03	74°29.95' S	01°57.65' E	2843	89
SS9808	DML21	74°40.03' S	04°00.10' E	2980	83
SS9810	DML17	75°10.02' S	06°29.91' E	3160	63
SS9812	DML16	75°10.04' S	05°00.20' E	3100	70
SS9814	DML15	75°05.02' S	02°30.06' E	2970	71
SS9815	DML14	74°56.95' S	01°29.67' W	2840	81
SS9817	DML13	75°00.00' S	04°29.78' W	2740	80
SS9901	DML25	75°00,14' S	00°00,42' E	2882	72
SS9908	DML25	75°00,14' S	00°00,42' E	2882	72
ice cores:					
FB9809	DML03	74°29.95' S	01°57.65' E	2843	89
B31	DML07	75°34.89' S	03°25.82' W	2669	59
B32	DML05	75°00.14' S	00°00.42' E	2882	62
B33	DML17	75°10.02' S	06°29.91' E	3160	47

Ice cores were packed in PE bags in the field and transported to Neumayer station. All core material and pit samples were shipped in freezer facilities to Bremerhaven. In our cold laboratory the upper 7-10 m of the cores at DML03, DML05, DML07, and DML17 were sub-sampled for chemical studies in 2 cm resolution (further on referred to as high resolution samples). With respect to the annual snow accumulation at the individual sites this corresponds to a resolution of approximately 5-9 samples per year. The high resolution samples cover the time period from 1945

to 1990. The deeper parts of the cores were subdivided into one sample per year (further on referred to as low resolution samples) according to the records measured by continuous flow analysis (CFA), which show distinct annual cycles [Sommer et al., 2000a].

All ice core samples were thoroughly de-contaminated under clean room conditions using a contamination free electromechanical plane [Fischer and Wagenbach, 1998a]. The de-contaminated samples were packed in pre-cleaned PE bags, which had been rinsed with ultra-pure water. To check contamination during handling, ultra-pure water samples (further on called process blanks) were prepared, frozen and processed like the cores in the processing routine. Additionally, IC vials were filled with ultra-pure water to quantify the remnant ion concentrations of the ultra-pure water itself and the contamination introduced during the analysis (further on called vial blanks). After decontamination all samples were melted under clean room conditions and filled in pre-cleaned PE vials for analysis and as archive material.

6.3.2 Analysis

During the field season 1997-1998 CFA measurements had been carried out on the core samples from DML03, DML05, DML07 and DML17 for Na^+ , Ca^{2+} , NH_4^{2+} , H_2O_2 and HCOH at Neumayer station [Sommer et al., 2000a; Sommer et al., 2000b]. Additionally, IC analyses for MSA , Cl^- , NO_3^- , SO_4^{2-} were performed at Neumayer station on samples taken from several of the snow pits (SS9803, SS9807, SS9805, SS9810).

All other snow pit samples and all high resolution core samples were analysed for concentrations of MSA , Cl^- , NO_3^- , SO_4^{2-} , Na^+ , NH_4^+ , K^+ , Mg^{2+} , and Ca^{2+} using IC in the laboratory at Alfred-Wegener-Institute in Bremerhaven. The low resolution core samples were measured for anions only. For those samples, sodium and calcium concentrations were taken from the CFA measurements [Sommer et al., 2000b]. IC analyses of snow pit and core samples were performed on Dionex 500 systems using an isocratic method for cations and a gradient method for anions equipped with a Dionex CS12 and a Dionex AS11 separator column, respectively. The cation system was running in the auto-suppression mode while the anion system used an external ultra-pure water supply for the regeneration chamber of the suppression unit.

Average blank concentrations for 159 process blank samples and 449 vial blanks are listed in Table 6.2. Laboratory and process blank concentrations were below the lowest calibration levels and distinctively below the sample concentrations for all anion species. Comparison of process and vial blanks shows that any additional contamination introduced by the decontamination routine in the cold laboratory is

negligible. Because of these low blank values no corresponding blank correction was necessary for the presented ion concentrations.

The analytical error of the IC measurements is better than 10% for all sample concentrations which are well above the blank level. However, despite the extremely low blank levels the lower end of the sample concentration range overlaps with the process blank values for NH_4^+ , K^+ , Mg^{2+} and Ca^{2+} increasing the analytical error of such samples significantly. In the following only anion and Na^+ concentrations will be discussed.

Table 6.2: Tabular list of process and vial blank and sample values.

Summary of ion concentrations in process blanks (PB) (n=159), vial blanks (VB) (n=449) and samples. Average concentrations and standard deviations of blank values, and for comparison the range of all sample concentrations as well as the typical concentration level found in the ice cores (time period 1865-1997) and snow pits (time period 1983-1997). The expression not det. in the Table is equal to below detection limit.

component	PB mean [ng g ⁻¹]	PB σ [ng g ⁻¹]	VB mean [ng g ⁻¹]	VB σ [ng g ⁻¹]	DML03 median [ng g ⁻¹]	DML05 median [ng g ⁻¹]	DML17 median [ng g ⁻¹]	snow pits median [ng g ⁻¹]	Value range [ng g ⁻¹]
MSA	not det.		not det.		8.74	6.80	4.49	10.73	0.6 - 65
Cl^-	2.56	1.22	2.29	1.41	44.32	48.52	46.81	42.45	7.7 - 518
NO_3^-	2.14	1.65	2.31	1.86	56.77	46.77	45.01	61.79	12.5 - 262
SO_4^{2-}	1.92	1.07	1.83	1.37	46.35	51.73	66.92	77.39	8.6 - 340
Na^+	0.47	0.47	0.59	0.60	17.47	19.24	19.13	13.58	0.5 - 151
NH_4^+	2.11	0.58	1.95	0.73	3.8	4.6	3.6	3.4	0.2 - 39
K^+	0.81	0.45	0.73	0.46	1.2	1.7	3.1	1.2	0.2 - 47
Mg^{2+}	0.23	0.10	0.25	0.12	2.0	2.3	2.0	1.7	0.1 - 40
Ca^{2+}	1.00	0.49	1.07	0.72	1.7	1.8	1.4	1.2	0.3 - 67

The sodium concentrations measured in high-resolution by IC and CFA agree very well with each other (see Figure 6.3). Average sample concentrations of both methods are equal on the 95% confidence level. Slight differences in the depth axes between the two methods can be attributed to variability in the flow velocity of the CFA and/or small losses of ice during the cutting of discrete samples. At certain depths the CFA shows gaps (Figure 6.3), where data suspect of contamination had been removed from the CFA data set [S. Sommer, pers. comm.]. However, re-measuring these intervals in high resolution using IC proved these high values to be uncontaminated ion concentrations.

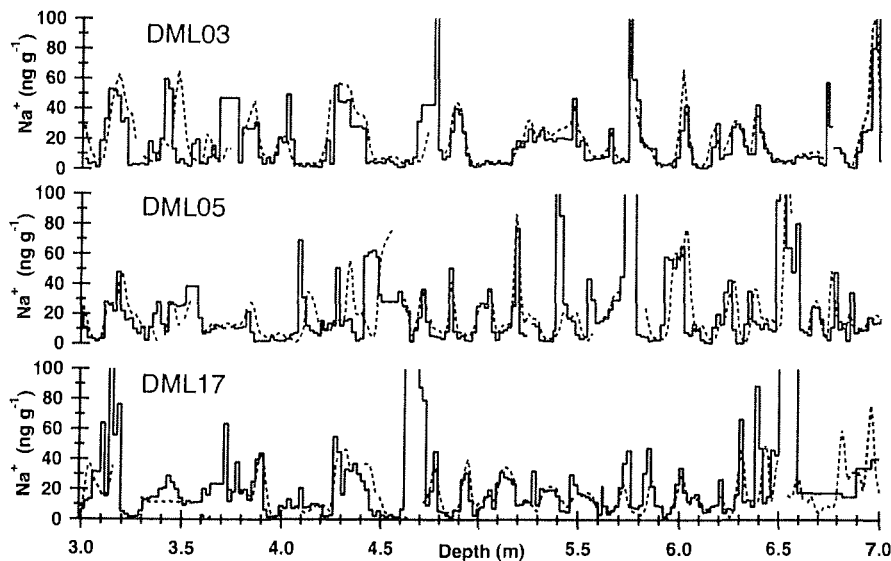


Figure 6.3: IC and CFA measurements of sodium.

Comparison of sodium concentration profiles for cores at DML03, DML05 and DML17. The solid lines represent values determined by ion chromatography, the dotted lines by CFA measurements [Sommer et al., 2000b].

6.3.3 Dating

A preliminary dating by dielectric profiling was carried out, showing that the volcanic eruption of Tambora in 1815 could be clearly detected in all cores. Accordingly, dating based on radioactive horizons of nuclear weapon tests in the 1950s and 60s, as used in an earlier study in this area [Oerter et al., 1999], was not performed here. Stratigraphic dating was accomplished by Sommer et al. [2000a] using a combination of annual layer counting in the CFA records and identification of the most prominent historic volcanic horizons in the electrolytical conductivity profile. The latter are mainly related to high concentrations of sulphuric acid in the respective snow layers. In general, this dating was adopted for this study. Only slight corrections were made according to our high resolution snow chemistry profiles: For the high resolution and snow pit samples annual markers were set at the falling flank of Na^+ and the rising flank of non-sea-salt (nss) sulphate (calculated by subtracting the sea-salt contribution from the total sulphate concentration according to $[\text{nssSO}_4^{2-}] = [\text{SO}_4^{2-}] - 0.252 [\text{Na}^+]$), indicating the spring season (Figure 6.4). Stable isotope profiles were not considered because of resolution constraints and diffusional

smoothing of the isotope record. Only in the case of snow pit SS9908, which was sampled for isotope and chemistry analyses in high resolution (2cm), dating of this snow pit was carried out by marking the summer maximum in δD for each year (Figure 6.5).

Dating of the cores using the high resolution CFA records was reliable within ± 5 years [Sommer et al., 2000a] over the last millennium. Dating of the DML05 core, however, had to be modified at one point. Sommer et al. [2000a] assigned a peak in the conductivity record at a depth of 6.12 m to the eruption of Mt. Agung, Indonesia, in the year 1963 A.D, which was also observed at other Antarctic sites [Delmas et al., 1985; Delmas et al., 1992; Isaksson, 1994]. However, the coherent increase of MSA and nss-sulphate at this depth implies that the assigned peak in the DML05 core is mainly caused by biogenic sulphate input and not by a volcanic eruption. Additionally, an utmost prominent double peak in the sea-salt components could be found in all cores as indicated in Figure 6.4. This feature could only be aligned for all cores within the dating accuracy by shifting the eruption of Mount Agung in DML05 to another peak in the sulphate and conductivity profiles at a depth of 6.77 m.

Based on this dating and using a robust identification routine for volcanic peaks [Fischer and Wagenbach, 1998b] in the sulphate time series 102 sulphate horizons could be detected in the core at DML05 over the last 2000 years. 57 of these peaks could be assigned to documented volcanic eruptions providing further support for our core chronology.

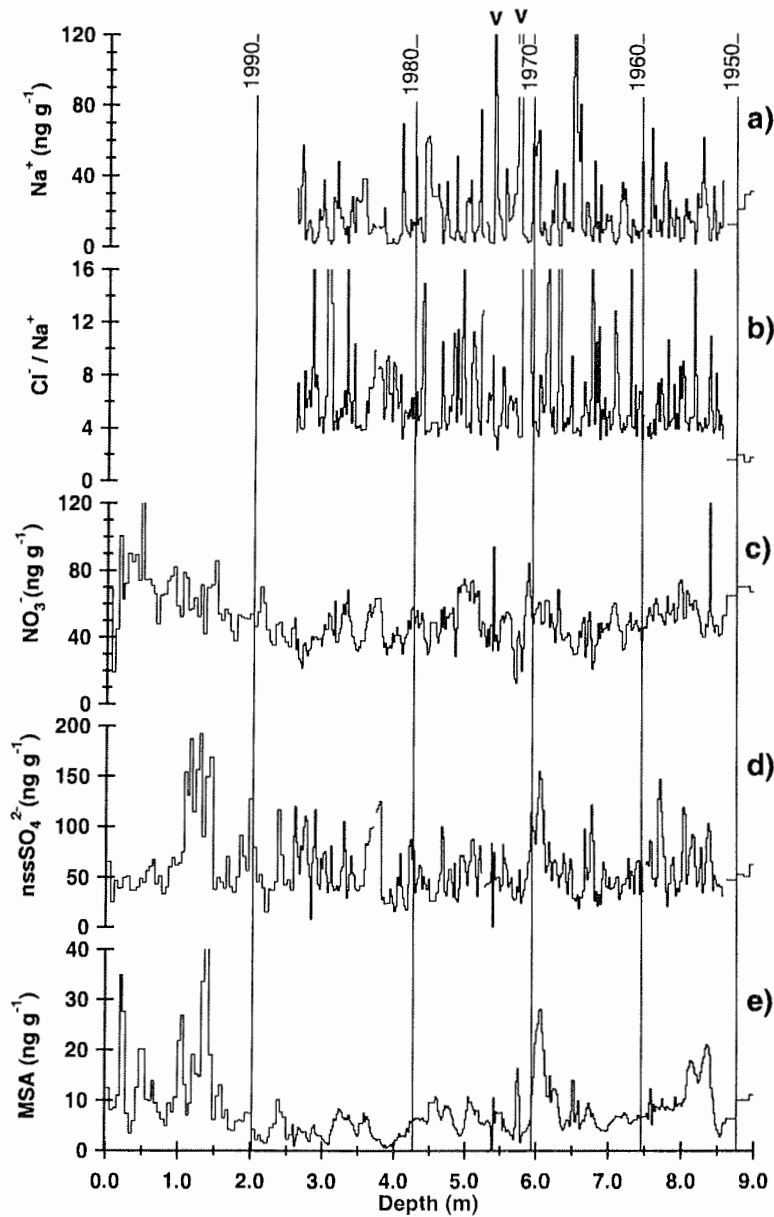


Figure 6.4: SS9905 and upper part of B32 at DML05.

a) Concentration of sodium, b) Cl^-/Na^+ ratio, concentrations of c) nitrate, d) nss-sulphate and e) MSA versus depth for the snow pit (SS9805) and core (B32) at DML05. The snow pit data cover the top 2.58 m, the high resolution sequence of core DML05 the interval from 2.58 down to 8.52 m. The arrows indicate the prominent double peak in sea-salt concentration occurring in all three cores. The vertical lines mark the time between the falling flank of Na^+ and the rising flank of nssSO_4^{2-} indicating the spring season.

6.4 Results and discussion

6.4.1 Seasonal variation

The high resolution records of the chemical components in snow and ice show consistent seasonal variations in all three cores and snow pits. An example of these seasonal cycles is shown in Figure 6.5 for the high resolution snow pit SS9908 and in Figure 6.4 for the snow pit SS9805 (depth from 0-2.58 m) and the core B32 (2.58-9 m) at DML05. Figure 6.5 also shows the results for the isotopic signature of the ice acting as proxy thermometer. Automatic weather stations (AWS) deployed in central DML [Reijmer and van den Broeke, 2001b] reveal a strong temperature maximum in December/January and very cold conditions ranging from May to October. AWS snow height measurements indicate that a few major precipitation events were responsible for most of the annual snow accumulation. For instance in 1998 only four snow fall events contributed about 80% of the annual snow accumulation [Reijmer et al., 2001c]. In principle, this is also supported by modelling studies [Reijmer and van den Broeke, 2001b; Noone et al., 1999]. Despite this event-like precipitation characteristic, δD shows a well developed seasonal cycle with maxima corresponding to the temperature maxima in summer and minima in winter. Due to the diffusional smoothing of the isotope record in the firn single precipitation events, however, cannot be distinguished in the δD record and dating of the seasonal cycles in ion concentrations relative to the isotope record is only accurate to a few months. In the following we only distinguish between 4 major seasons not referring to specific months.

In Figure 6.5a sodium, which together with chloride is mainly derived from sea-salt aerosol, shows maximum ion concentrations on the rising flank of the δD record indicating a sea-salt maximum in late winter/spring. This points to enhanced cyclonic activity over the Southern Atlantic region connected to higher transport of sea-salt aerosol onto DML during late winter/spring, despite the larger sea-ice coverage during this time of the year. Higher storminess in this season is also indicated by faster air mass transport in trajectory studies by Reijmer and van den Broeke [2001b].

MSA and nss-sulphate, which in Antarctica are essentially derived from the marine biogenic production of dimethylsulphide (DMS) [Legrand, 1995; Stenberg et al., 1998], show a prominent maximum on the declining flank of the δD (Figure 6.5d and Figure 6.5c) record equivalent to maximum concentrations in autumn. This is significantly later than the distinct biogenic sulphur maximum observed at the coastal Antarctic station Neumayer [Minikin et al., 1998] in summer when sea ice

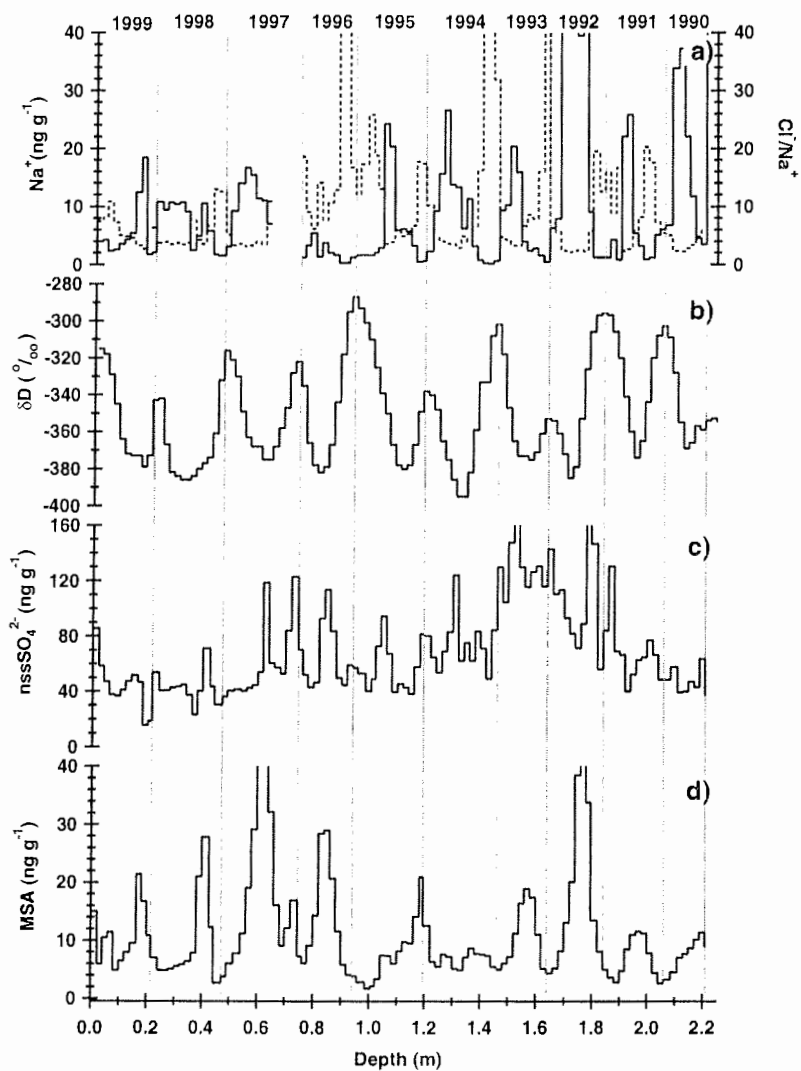


Figure 6.5: Snow pit SS9908.

a) Concentration of sodium and Cl^-/Na^+ ratio (dotted line), b) δD [W. Graf pers. comm.], c) concentrations of nss-sulphate and d) MSA versus depth for snow pit SS9908. In accordance to other high altitude Antarctic sites [Isaksson, 1994; Stenberg et al., 1998; ?; Kirchner and Delmas, 1988], sea-salt-sulphate explains only around 7% to 12% of the total sulphate concentration. The vertical lines mark the summer maximum in δD for each year.

retreats for a short time. Such a phase shift may be attributed to the different source areas of biogenic sulphur relevant for DML compared to Neumayer (NM). While NM is more influenced by DMS production in high latitude ocean areas relatively close to NM, trajectory studies for DML show that air masses originate as far as 55°S five days back in time [Reijmer, 2001a]. In this area biogenic productivity is extended to March/April [Minikin et al., 1998] in line with our MSA and nss-sulphate peak during that time of the year.

However, nss-sulphate shows also a second peak during late spring/summer in the high-resolution snow pit record (Figure 6.5c) which is only occasionally connected to elevated MSA levels. Due to the lower resolution of the core data compared to data from snow pit SS9908, the double peak in nss-sulphate concentrations is not always resolved in the cores. Based on aerosol measurements of the cosmogenic radioisotopes ^{10}Be and ^7Be performed at NM by Wagenbach et al. [1998a] a stratospheric input of sulphate during summer seems to be very unlikely. Therefore, only biogenic sources appear to be able to explain such a sulphate input. A post-depositional migration of the MSA peak away from high acidity layers (e.g. high sulphuric acid concentrations), which has been observed in ice cores from other Antarctic sites [Minikin et al., 1994; Ivey et al., 1986; Pasteur and Mulvaney, 2000], cannot be clearly seen in Figure 6.5d. However, post-depositional smoothing of the MSA record is observed below a few metres depth in Figure 6.4e.

Post-depositional effects were also observed for nitrate which originates from lightning induced NO formation and intrusions of stratospheric air masses [Wolff, 1995; Wagenbach et al., 1998b]. In contrast to results from firn cores retrieved at high accumulation sites showing maximum nitrate concentrations in summer [Minikin et al., 1994; Hou et al., 1999] it was not possible to detect any seasonality in our measured nitrate profiles. This can be attributed to a substantial post-depositional nitrate loss, which degrades any initially existing seasonal signal. The nitrate loss is up to 40%, which is estimated from the 40% lower mean nitrate concentration in the core B32 compared with the mean concentration in the snow pit SS9805 (upper 2.58 m).

6.4.2 Spatial distribution

The dependence of average ion concentrations on the major geographical and glacio-meteorological parameters in the DML region is shown in Figure 6.6. To distinguish surface snow and older firn strata, which might have been subject to post-depositional alterations, and to improve the spatial resolution both average ion concentrations in the snow pits (for the common time period 1997-1994) and the

ice cores (over the time period 1950-1865) are plotted in Figure 6.6. Additionally, data for the same period (1950-1865) from a DML ice core investigated by Isaksson [1994] are added to Figure (6.5).

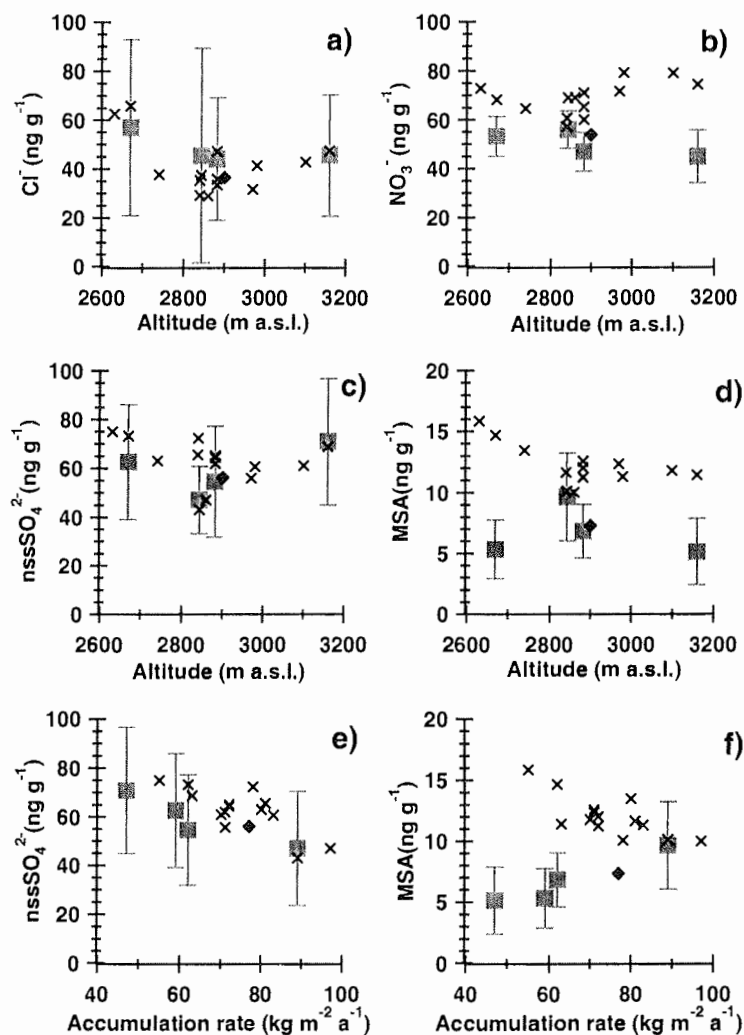


Figure 6.6: Spatial distribution of chemical species.

Spatial variation of average ion concentrations with altitude (a-d) and average annual snow accumulation (e-f) in the DML region. Crosses refer to snow pits (1997-1994 A.D.), while squares indicate ice core (1950-1865 A.D.) averages. The standard deviation of the mean annual values for the ice cores are given by error bars. Also plotted are data for an DML ice core (rhombus) investigated by Isaksson [1994] covering the time period 1950-1865.

All our drill sites are located on the Antarctic plateau and cover an altitude range between 2669m (DML07) and 3160m (DML17) (Figure 6.2). At the same time the average annual snow accumulation covers a range from 89 kg m⁻² a⁻¹ (DML03) to 47 kg m⁻² a⁻¹ (DML17) (Table 6.1) with generally lower accumulation rates found at higher altitudes. Also lower accumulation rates were found on the lee-side of the main ice divide (DML07 in Figure 6.2). Note that the snow pits cover an altitude range between 2630 m (SS9802) and 3160 m (SS9810) (Figure 6.2) but are limited in the time span shared by all snow pits to only four years. Thus, the temporal representativeness of the pit averages (Figure 6.6) is limited.

The long-term core averages in nss-sulphate show no clear relationship with altitude but a strong decline with higher accumulation rates (Figure 6.6e). The recent snow pit data essentially show the same feature, however with a somewhat higher concentration level reflecting the different time periods covered. Such a spatial decrease of sulphate concentration with higher snow accumulation can be expected from the dilution of dry deposited sulphate aerosol by higher precipitation rates. Using the linear dependence of sulphate concentration on inverse snow accumulation as given by Fischer and Wagenbach a total dry deposition flux of app. 240 ng cm⁻² a⁻¹ can be formally deduced. This implies that about three quarters of the total sulphate flux are due to dry deposition at the future EPICA drill site in DML 0°04.07' E, 75°00.10' S) with a long-term accumulation rate of 62 kg m⁻² a⁻¹.

In Figure 6.6d and Figure 6.6f MSA shows an exponential decrease with higher altitude and higher snow accumulation for the snow pit data. However, in Figure 6.6f for the long-term core averages reflecting older firn the opposite relationship with snow accumulation is found. While the snow pit data of MSA and nss-sulphate show a similar dependence on a change in accumulation rate, the opposite relationship was observed in the core data. Considering that the source of both MSA and the main part of nss-sulphate is the photo-oxidation of DMS [Legrand, 1995; Saltzman, 1995] similar transport and deposition mechanisms, thus, a similar geographical distribution is expected. One reason which may contribute to a difference in the spatial distribution of MSA and sulphate in the ice core averages could be related to the different atmospheric residence times of MSA and nss-sulphate with their gaseous precursors in the atmosphere. The photo-oxidation mechanism of DMS is highly complex [Yin et al., 1990]. In short, MSA is produced via short-lived transient intermediates, while formation of sulphate occurs via the more stable SO₂, which enlarges the effective atmospheric residence time of this branch of DMS oxidation considerably. Thus, MSA concentrations may be subject to stronger depletion along an air mass trajectory over the DML region. However, a 50% decline in the MSA

ice core averages appears to be far too big to be accounted for by this effect. Even more important seems to be that a difference in atmospheric residence time can not explain the different spatial distribution of snow pit and ice core MSA data.

In view of the inconsistency between snow pit and ice core averages and considering the very large size of the spatial MSA decrease in the ice core data in this geographically rather uniform area, only an accumulation rate dependent post-depositional loss of MSA could readily explain a net decrease of up to 50%. Such a loss of MSA has been reported from the low-accumulation site Vostok, East Antarctica, by Wagnon et al. [1999], who however, pointed out that a re-evaporation of particulate MSA from the snow pack is difficult to achieve. Additionally, such a loss cannot be unambiguously detected in our pit profiles. There are somewhat higher MSA concentrations in the uppermost metre, from year 1992 to 1997 (see Figure 6.5d and Figure 6.6d). However, higher MSA concentrations in these years may also be attributed to extraordinarily high DMS concentrations possibly connected to El Niño events as proposed by Legrand and Feniet-Saigne [1991] for South Pole snow and by Isaksson et al. [2001] for Amundsenisen. Taking into account that intervals with higher MSA concentrations are also repeatedly found in deeper layers, the question of the existence of a post-depositional net loss of MSA remains open.

The sea-salt derived components chloride (Figure 6.6a) and sodium show an exponential decline with altitude with an e-folding height of app. 1800 m and 1300 m, respectively. The larger scaling height of chloride compared to sodium may reflect the additional transport of gaseous HCl onto the ice sheet, produced by an acid induced release of HCl from sea-salt aerosol [Legrand and Delmas, 1988]. Such an HCl contribution is also supported by the existence of significant nss-chloride concentrations in the upper snow layers on the plateau. This effect is most prominent during summer when biogenic sulphur species lead to a substantial acidification of the atmospheric aerosol as reflected in summer peaks in the Cl^-/Na^+ ratio in our high-resolution records (Figure 6.4a). The geographical decline in sea-salt aerosol essentially levels out on top of the DML region (Figure 6.6a). Sea-salt concentrations in a core investigated by Isaksson [1994], covering the same time period as the cores studied here, are somewhat lower than our ice core data. Note however, that the concentrations of all other ion species agree well between DML cores studied here and the one studied by Isaksson [1994]. The lower sea-salt concentrations in the core studied by Isaksson [1994] can most likely be explained by the removal of very large concentration values in that core which were suspected to be contaminated [E. Isaksson, pers. comm., 2000].

Nitrate shows a rather uniform spatial distribution in Figure 6.6b, with significantly higher nitrate concentrations in recent snow pits compared to the older ice core data. We attribute this finding to post-depositional nitrate loss [Mulvaney et al., 1998; Wolff, 1995; Legrand and Kirchner, 1990], which level the ion concentrations. A detailed discussion of the post-depositional loss in nitrate is the subject of a paper by Röthlisberger et al. [2002]. A post-depositional nitrate loss of the size observed by Röthlisberger et al. [2002] at ultra low accumulation sites like Dome Concordia (from 1000 ppm at the surface down to 15 ppm), however, is not observed in our cores. Nitrate concentrations in surface snow samples taken during the 2000/2001 season at DML05 reach 263 ppb (C. Piel, pers. comm., 2000), whereas average concentrations of about 56 ppb (at DML03), 47 ppb (at DML05), 53 ppb (at DML07) and 45 ppb (DML17) were found in the DML cores. The average nitrate concentrations at Dome C [Legrand and Delmas, 1986] after post-depositional alteration are less than a third of the values found in DML. Even taking into account a higher post-depositional loss of nitrate at Dome C, where the accumulation rate is a factor 2-3 smaller than in DML, the size of this decrease is extremely large. Accordingly other factors in addition to snow accumulation rate such as temperature, snow formation and re-crystallisation in the snow pack or wind speed may additionally affect the post-depositional nitrate loss.

6.5 Conclusions

Seasonal and spatial variations of chemical snow parameters in Dronning Maud Land have been discussed based on ion chromatographic analyses of four intermediate deep ice cores covering the last 140 years and fourteen snow pits covering the time period 1994 - 1997 A.D.

The seasonal and spatial variations show that the area under investigation in DML is well suited for the reconstruction of long-term chemical records from the new EPICA ice core. The snow accumulation rate is sufficiently large to ensure seasonal information while at the same time enabling to reach far into the past. The seasonal signal is well archived for sulphate and sea-salt components allowing for an accurate stratigraphic dating of the new deep core at least for the Holocene period.

The variation in the spatial distribution of most chemical species on the DML plateau is mainly linked to the change in snow accumulation rate and altitude. The ice velocity at the future EPICA drill site and upstream along the ice divide is on the order of 1 m a^{-1} which is lower as shown by balance velocity calculations

[Huybrechts et al., 2000]. This means that for a time span of 150 000 years the horizontal displacement from the original location, where the precipitation had been deposited, to the drill site is approximately 150 km or less. This means the catchment area for the deep ice core is roughly the area in between DML17 and DML05, with a rather uniform accumulation pattern [Oerter et al., 2000]. Thus, assuming a similar dependence of ion concentrations with altitude and snow accumulation as shown in Figure 6.5 in the past, it is in principle possible to correct for minor spatial changes of ion concentrations. In any case, for the Holocene time interval the catchment area decreases to 10 km around the future deep drilling site, where spatial corrections are unnecessary. For nitrate and potentially MSA a post-depositional loss is found, which, however, is not as severe as the one found at Dome Concordia. Nevertheless, the interpretation of these species in terms of atmospheric changes needs further studies to understand and quantify such re-evaporation effects.

6.6 Acknowledgements

This work is a contribution to the "European Project for Ice Coring in Antarctica" (EPICA), a joint ESF (European Science Foundation)/EC scientific programme, funded by the European Commission and by national contributions from Belgium, Denmark, France, Germany, Italy, the Netherlands, Norway, Sweden, Switzerland and the United Kingdom. This is EPICA publication no. 40. Financial support by Deutsche Forschungsgemeinschaft (project OE 130/3) is grate fully acknowledged. We thank Thaddäus Bluszcz, Michaela Lelke and Thomas Max for the excellent assistance in the laboratory. We also thank E. Isaksson and an unknown reviewer as well as K. Goto-Azuma and E. Wolff for helpful comments to improve this manuscript.

Chapter 7

Impact of climate parameters on Amundsenisen

7.1 Abstract

In the framework of the European Project for Ice Coring in Antarctica (EPICA) four intermediate deep ice cores were recovered by the Alfred Wegener Institute for Polar and Marine Research on Amundsenisen, Dronning Maud Land (DML), Antarctica, in the 1997/1998 field campaign. The dominant ion species and sampling sites are determined by EOF analyses and principal components (PC) are calculated. Correlation of the PCs and the sea-surface temperature is performed and associated pattern in the SST anomaly detected. This resulting pattern looks similar to the SST pattern associated to El Niño events, and gives a first indication of recorded El Niño signature in the ice core records. In addition, wavelet and coherence spectra have been computed, detecting periodicities between 2-4 years in the PC of the nss-sulphate component and Nino Index 3. Furthermore, it is shown that MSA records from DML do not provide information about relationships to El Niño event phenomenon, because of post-depositional effects. The hypothesis of migration of MSA from summer to winter layers is supported by this results.

The signature of an El Niño event in the nss-sulphate records is not archived on highest order, overlaid by local or regional processes, but is present in the records still at a significant level.

This chapter is based on a publication in preparation: Göktas, F. et al. Evidence of El Niño signature in glacio-chemical ice core records from Amundsenisen, Dronning Maud Land, Antarctica.

7.2 Introduction

Along with the cycles of nitrogen and carbon, the sulphur cycle is one of the major biogeochemical cycles of interest for the chemical composition of earth's atmosphere [Schlesinger, 1997]. The sulphur cycle is involved in a number of ecological issues of importance on local, regional, and global scales. These issues include the formation and transport of acid precipitation [Rohde, 1999], the impact of aerosols on human and environmental health and the effect of aerosols on cloud generation and their radiative properties [Charlson et al., 1987; Menon et al., 2002]. Sulphuric acid (H_2SO_4) is a major oxidation product of reduced sulphur gases (H_2S , CS_2 , CH_3SH , $(\text{CH}_3)_2\text{S}$) and of SO_2 . These sulphur gases are emitted into the atmosphere by various sources, e.g. terrestrial, volcanic, biomass burning, oceanic. While for the Northern Hemisphere (North America, Europe, and Greenland) more than 50% of the sulphate budget can account to emissions of man-made sources [Rohde, 1999], the oceanic source dominates on the global scale [Saltzman, 1995; Bates et al., 1992]. In particular for high latitudes in the Southern Hemisphere, as observed from Antarctic ice core records [Legrand, 1995; Legrand and Mayewski, 1997].

The oceanic source is classified into sea-salt and non-sea-salt (nss) sulphate. Man-made sources, volcanic eruptions and oceanic marine biota contribute to nss-sulphate. As observed in ice cores from other Antarctic sites and the longterm nss-sulphate records studied here (Appendix B) the anthropogenic influence is negligible (Figure A.4). The volcanic input can be determined as shown in Chapter 5 and subtracted from the nss-sulphate concentration, and thus the oceanic part is relevant.

While the sea-salt sulphur oxidises to sulphuric acid via the SO_2 oxidation pathway, the atmospheric sulphate derived from gaseous emissions from marine biota is produced via complex pathways. Most species of phytoplankton, ubiquitous in the oceans, excrete dimethyl-sulphide (DMS, CH_3SCH_3) which escapes to the air where it reacts to form sulphate (SO_4^{2-}) and methane sulphononic acid (MSA, CH_3SO_3^-) aerosol [Yin et al., 1990]. By global atmospheric transport (Chapter 2) both aerosol reach high latitudes, where they are deposited on the vast ice sheets of Greenland and Antarctica. Thus, incorporated in the snow and ice layer an unique climate archive develops.

Several studies have been carried out to investigate these biogenic sulphur components, MSA and nss-sulphate, in ice cores from Greenland [Legrand et al., 1997; Saltzman et al., 1997] and Antarctica [Pasteur et al., 1995; Legrand and Feniet-Saigne, 1991; Isaksson et al., 2001]. These previous studies provided a biogenic sulphur record and two of them relate peaks in the MSA record to events of the

El Niño phenomenon. However, no study has examined the relationship between the phytoplankton (responsible for DMS production) and sea-surface temperature (SST), whose largest anomaly is caused by the El Niño phenomenon.

In this work, we present the MSA and nss-sulphate records revealed from four intermediate deep ice cores from Amundsenisen, Dronning Maud Land, Antarctica. After introducing the source for the biogenic sulphur components and the methods used, Empirical Orthogonal Function (EOF) analysis is applied to compute the common signal in four ice core records to investigate how far both components are related to SST, as well as to find the associated source regions. The source region is discussed in its phytoplankton content, temperature pattern and teleconnection characteristics. The common signal is also investigated on its temporal structure by wavelet analysis and compared to NINO indices. The SST data from the NCEP/NCAR Reanalysis project was used in the analysis.

7.2.1 Source of biogenic sulphur

In the marine environment the major volatile sulphur compound is in the form of DMS excreted by living planktonic algae, e.g. coccolithophore *Emiliana huxleyi*, prymnesiophyte *Phaeocystis*, and dinoflagellate *Gymnodinium*, the major species in an algae bloom [Andreae, 1990; Saltzman, 1995]. Its biochemical precursor is dimethyl-sulfoniopropionate (DMSP), a globally distributed, intra-cellular constituent in marine phytoplankton. The production of DMS is an order of magnitude higher for polar *Phaeocystis* than for diatoms [Matrai et al., 1995], but Jones et al. [1998], and Matrai and Vernet [1997] showed that the contribution of diatoms to the sub-polar and polar water column budget of DMS and DMSP was significant and cannot be overlooked. DMSP has an osmoregulating function in marine algae, from which DMS is an inevitable product of metabolism [Saltzman, 1995]. Recent work has revealed that DMS formation could represent almost 90% of sea to air transfer of sulphur [Simó et al., 2000].

Attempts to identify the variables which control the oceanic production of DMS have shown that DMS and DMSP concentration in ocean water and marine air is about four times higher in sub-polar latitudes than in equatorial regions [Davison and Allen, 1994; Davison et al., 1996]. The First Aerosol Characterization Experiment (ACE 1) revealed that DMSP concentration were lowest in polar water [Jones et al., 1998]. This is consistent with results from Schultes et al. [2000], showing that variations in the net DMS production appear to be controlled by changes in water temperature and type and age of the plankton community. In general, lower water temperatures require higher DMSP concentrations to stimulate DMS production.

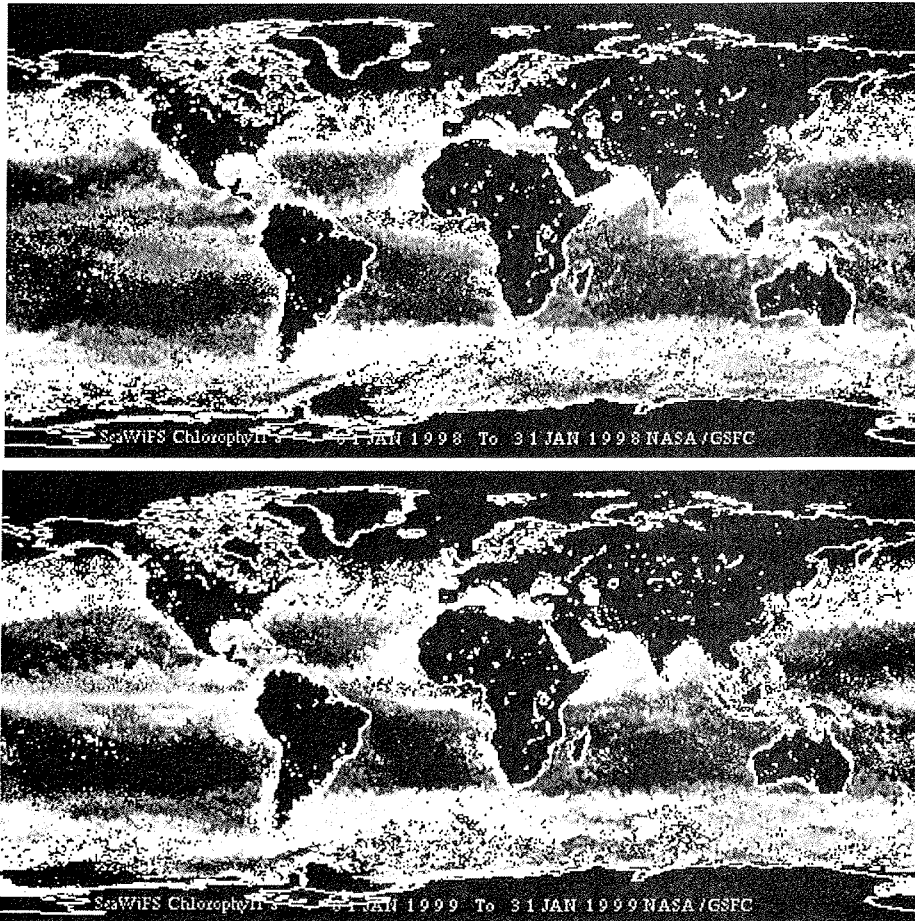


Figure 7.1: Map of biogenic activity of the Ocean in December 1997 and July 1998. A map demonstrating the biogenic activity via chlorophyll content in the ocean in January 1997 and 1998 is shown. In the case of Dronning Maud the south-west South Atlantic Ocean is of particular interest, as trajectory studies by Reijmer [2001a] have pointed out.

For the purpose of studying the biogenic activity of the oceans the project Sea-viewing Wide Field-of-view Sensor (SeaWiFS) has been started in September 1997 [SeaWiFS, n.d.]. The purpose of SeaWiFS data is to examine oceanic factors, e.g. the magnitude and variability of chlorophyll and primary production by marine phytoplankton, and determine the distribution and timing of spring blooms, i.e., the time of highly abundant growth. Chlorophyll is the primary photo-synthetic pigment and is contained in almost all plants [Götting et al., 1982]. In the oceans most of the chlorophyll is contained in the members of the phytoplankton. Chlorophyll captures the energy of sunlight. Therefore, as the concentration of phytoplankton increases, ocean colour shifts from blue to green [SeaWiFS, n.d.]. Hence, the measurement of ocean colour from space gives information about the chlorophyll content of the ocean and therewith about the phytoplankton distribution. In Figure 7.1 the chlorophyll maps from January 1997 and 1998 are presented.

The South Atlantic region shows high chlorophyll content, indicating high concentrations of phytoplankton. Considering the results of the trajectory study by Reijmer [2001a], most of the trajectories start in this area. Thus, it is expected that most of the biogenic sulphur in our ice cores originates from the Southern Atlantic Ocean and Southern Ocean.

The knowledge of the oxidation pathways of DMSP to DMS, and from DMS to sulphate and MSA (both in Figure 7.2) are well established [Saltzman, 1995; Yin et al., 1990; Simó and Pedrós-Alió, 1999].

Sources of nss-sulphate are volcanic eruptions, anthropogenic emissions (negligible here), and atmospheric oxidation of dimethyl-sulphide (DMS). Volcanic eruptions and the corresponding peak detection have been discussed in Chapter 5. The sporadically occurring events could be identified with the introduced sensitive peak detection algorithm. One method to minimise the influence of those eruptions is to substitute the identified peak values in the nss-sulphate concentration by the 30 year mean value around. That is expected to be a good approximation of the background sulphate loading of the atmosphere. An anthropogenic influence of man-made sulphate emissions as observed on Greenland for the past century in the nss-sulphate record could not be confirmed by either our or other ice core records from Antarctica (Appendix B).

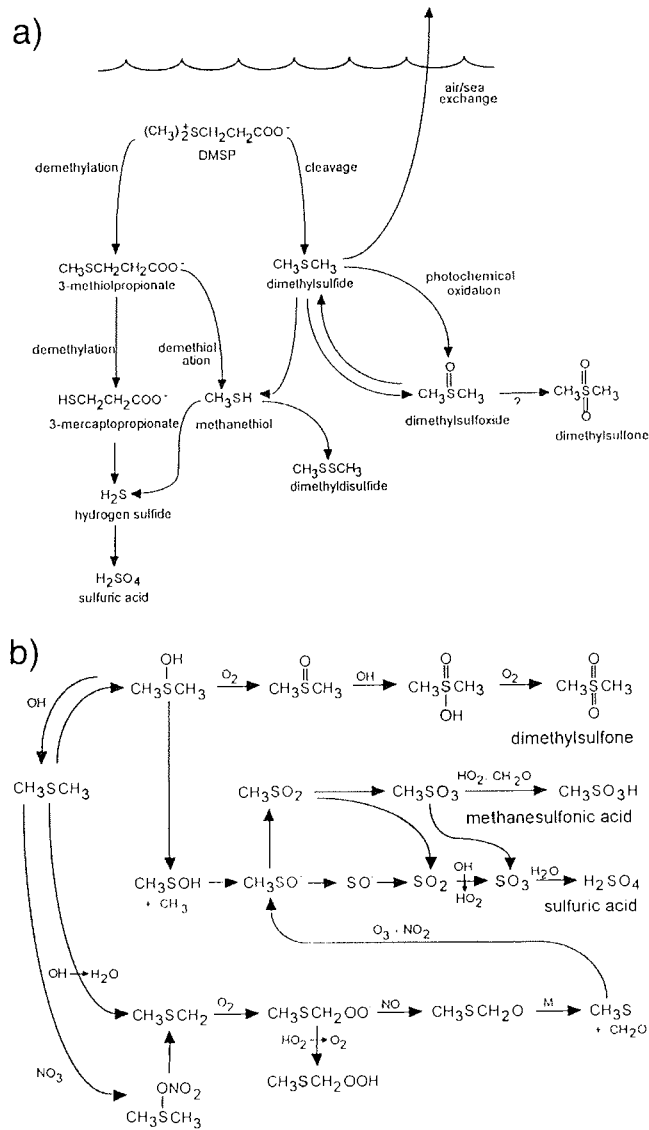


Figure 7.2: Oxidation pathways of DMSP and DMS.

The oxidation pathways of dimethyl-sulphoniopropionate (DMSP) and dimethyl-sulphide (DMS) are presented. The oxidation from DMS to MSA occurs in less steps than for nss-sulphate.

7.3 Methods

7.3.1 Site Selection, sampling, analyses and dating

In the framework of the European Project for Ice Coring in Antarctica (EPICA) several comprehensive pre-site surveys have been carried out by the Alfred Wegener Institute on Amundsenisen, Dronning Maud Land (DML) [Oerter et al., 1999; Oerter et al., 2000]. Data from four intermediate deep ice cores and corresponding snow pits, recovered during the field campaigns 1997/1998 and 1999/2000 (Figure 7.3), are presented.

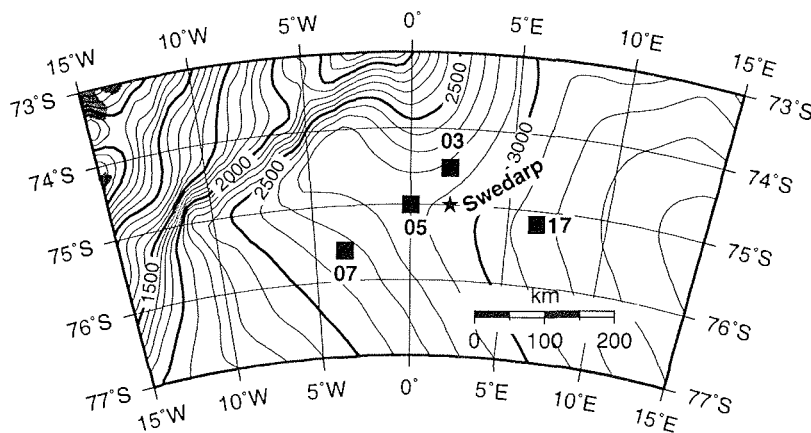


Figure 7.3: Area under investigation in DML.

Location of the four intermediate deep ice cores (squares), where also snow pits have been recovered. The star marks the other ice core from DML, which has been analysed for the major ion species by Isaksson [1994]. The present EPICA deep drilling site is located at $0^{\circ}04.07'E$, $75^{\circ}00.10'S$.

The sampling procedure of the snow pits and ice cores and the handling procedure in the cold room facilities in Bremerhaven have been described in detail in Chapter 3. The analyses of the snow pit and ice core samples by Ion Chromatograph and the dating of the glacio-chemical records are presented in Göktaş et al. [2002].

The focus of this work is on the ion species methane-sulphonic acid (MSA), nss-sulphate, sodium and chloride, where nss-sulphate was computed as the fraction of total sulphate (with 0.252 representing the ratio of sulphate to sodium in bulk sea water and using Na^+ as sea-salt reference ion) according to :

$$[\text{nss} - \text{sulphate}] = [\text{sulphate}_{\text{total}}] - 0.252 \cdot [\text{Na}^+]. \quad (7.1)$$

7.3.2 Reanalysis Data

To study the imprint of climate parameters in the ice core records, the data provided from the Reanalysis project of the National Centers for Environmental Prediction (NCEP) and National Center for Atmospheric Research (NCAR) was used. These two organisations have cooperated in a project denoted as "Reanalysis", to produce a retroactive record of more than 50 years analyses of atmospheric fields in support of the needs of the research and climate monitoring communities. Data from measurements carried out on land, ships, rawinsondes, aircrafts, satellites and other sources were involved for this computation.

Figure 7.4 shows the network of the ocean data, indicating the areas of measurements and as well as areas with missing data. Apparently, not all over the globe are instrumental observations feasible. For sites missing observational data the NCEP/NCAR Reanalysis project has applied spectral statistical interpolation.

From this Reanalysis project we used the sea-surface temperature (SST) data. For grid points over the land surface in the SST data set the air temperature is included. Therefore, these grid points have a number, but are not used.

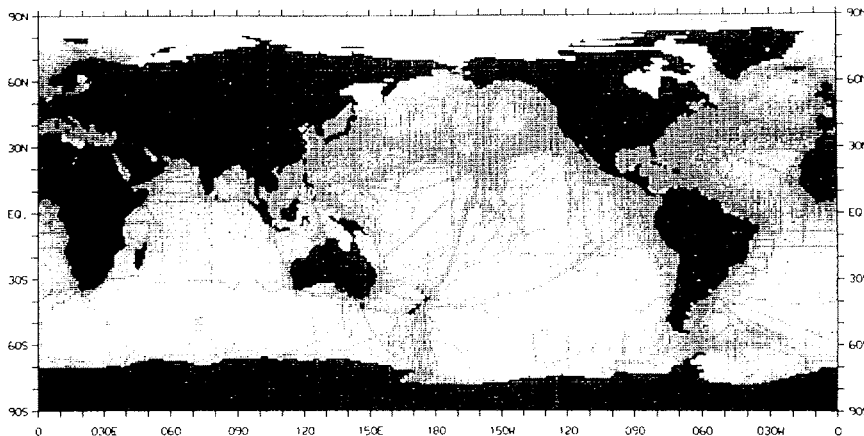


Figure 7.4: Network of measurements taken by oceanographic research vessels.

Network of historical ocean data taken by oceanographic research vessels. The standard oceanographic data obtained by research vessels are temperature, salinity, oxygen content, and concentrations of various nutrients (picture taken from Peizoto and Oort [1992]).

7.3.3 Analyses Methods

Several statistical methods have been introduced into climate research in the last decades [Storch and Zwiers, 1999], among others the Eigentechnique methods. These techniques aim to discriminate the signal of interest from that part of the signal, which represents unrelated processes. Furthermore, they provide tools to describe dominant spatial and/or temporal patterns in the signal of interest.

A method to discover the spatial patterns of multivariate (varying in space and time) data sets is the *Empirical Orthogonal Functions* (EOFs) analysis (also called Principal Component Analysis (PCA)) [Storch and Zwiers, 1999]. EOF analysis provides information about the dominant spatial patterns, its temporal variations, and the related importance of each variable (here sampling site or ion species).

To detect and isolate the temporal signature of data, both *singular spectrum analysis* (SSA) as well as *wavelet analysis* (WA) can be applied [Storch and Zwiers, 1999]. While the SSA is in fact a variation of the classical EOF analysis performed in the time domain [Storch and Zwiers, 1999], the WA provides two dimensional power spectra, revealing the evolution of periods over the time interval [Daubechies, 1990]. Moreover, the identification of spectral features by the SSA technique is controversial because of problems in handling trends in the data and of quasi-periodicities in climate processes [Baliunas et al., 1997]. In this work EOF and WA analysis were used and will be briefly introduced.

7.3.3.1 Empirical Orthogonal Function (EOF) analysis

The EOF analysis method has been explained and applied in several applications in climate and ice core research [Peixoto and Oort, 1992; Storch and Zwiers, 1999; Yiou et al., 1997; Mayewski, 1997; Meeker et al., 1997]. Therefore, it will be presented briefly in its most important aspects.

The time series (hereafter referred as variable) are represented by the multivariate vector $\vec{x}(t)$. This vector ($\vec{x}(t)$) is decomposed into the signal ($\sum_{k=1}^K \alpha_k(t) \cdot \vec{p}^k$), and the non-signal (\vec{n}_t) subspaces, expressed by:

$$\vec{x}(t) - \mu = \sum_{k=1}^K \alpha_k(t) \cdot \vec{p}^k + \vec{n}_t \quad (7.2)$$

with μ being the expectation of $\vec{x}(t)$, which is in fact the mean value of the time series. This is a projection of a signal into the signal subspace, which allows the identification of an orthogonal subspace with a series of orthogonal patterns \vec{p}^k . This orthogonal subspace, with dimension of k , is formed by the covariance matrix, which has the property $C^t C = C C^t = 1$ (with 1 the identity matrix), and

which provides a set of eigenvectors \vec{p}^k uncorrelated over space, i.e. orthogonal to each other. These eigenvectors are the *Empirical Orthogonal Functions* (EOFs). The corresponding temporal evolution of the EOFs are the "EOF coefficients" or "principal components" (PCs). The PCs are computed by using the dot product of:

$$\alpha_k(t) = \langle \vec{p}^k, \vec{x} \rangle \quad (7.3)$$

In general, the EOF associated with the highest eigenvalue is defined as EOF1. It explains most of the variance in the signal. To measure the explained variance by each of the EOFs the fraction of the total variance of the covariance matrix is calculated by:

$$var_{exp}(\vec{p}^k) = \lambda^k / \sum_{k=1}^K \lambda^k \quad \lambda, \text{ eigenvalue} \quad (7.4)$$

The contribution of each variable, here the sampling site or ion specie, in the multivariate vector \vec{x} to the explained variance by each EOF is computed by:

$$var_{exp}(x_i) = 1 - \frac{var(x_i - \alpha_k p_i^k)}{var(x_i)} \quad (7.5)$$

7.3.3.2 Wavelet analysis

The wavelet transform was introduced into geophysics in the early 1980s for analysis of seismic signals [Kumar and Foufoula-Georgiou, 1997]. The power of this method is in the analysis of the temporal structure of non-stationary processes and mathematical advances have enabled the application of this method also to other fields [Wang and Wang, 1996; Baliunas et al., 1997].

A wavelet transform resembles a local Fourier transform within a finite moving window with a width W , is proportional to the major period of interest, and is varied to explore a broad range of such periods [Perrier et al., 1995]. Thus, the varying dominant periodicities over time can be identified.

To decode a continuous non-stationary time series $x(t)$ in a frequency-time domain, the signal $x(t)$ has to be decomposed in terms of some elementary functions $\Psi_{b,a}(t)$ derived from an "analysing wavelet" by dilatation (a) and translation (b) [Lau and Weng, 1995]:

$$\Psi_{b,a}(t) = \frac{1}{(a)^{1/2}} \Psi\left(\frac{t-b}{a}\right) \quad (7.6)$$

where a denotes the period (scale) and b the position (time). The wavelet transform of a real signal $x(t)$ with respect to the analysing wavelet $\Psi_{b,a}(t)$ can be defined as a convolution integral:

$$W(b, a) = \frac{1}{(a)^{1/2}} \int \Psi^*\left(\frac{t-b}{a}\right) \cdot x(t) dt \quad (7.7)$$

where Ψ^* is the complex conjugate of Ψ and W is the continuous wavelet transformation. As "analysing wavelet" in this work the Morlet wavelet was used [Lau and Weng, 1995].

7.4 Results and discussion

7.4.1 Sample data

The annual mean ion concentration records revealed from the four ice cores are presented in Figure A.4. For the sea-salt records see the Appendix A.

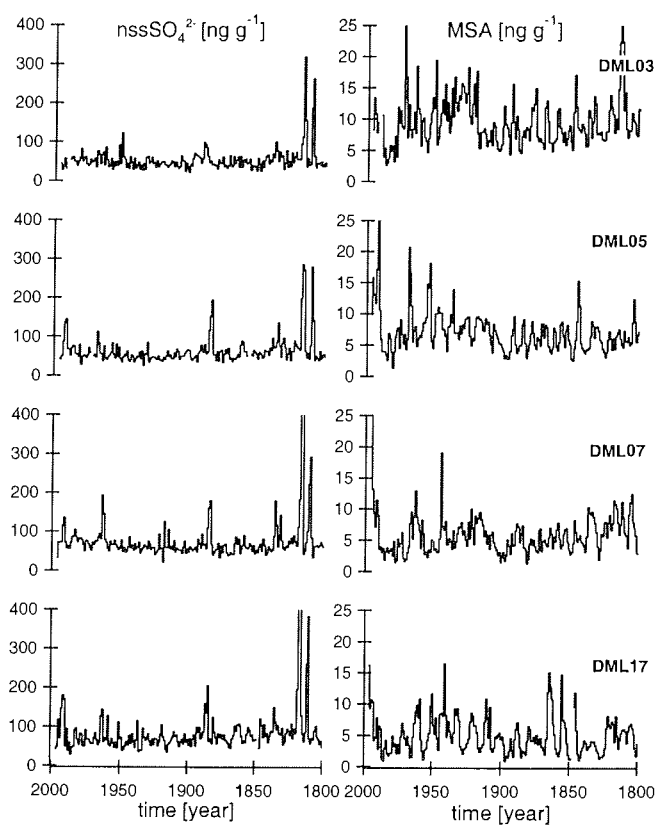


Figure 7.5: Annual ion concentrations of MSA and nss-sulphate.

Annual mean ion concentration records of MSA and nss-sulphate at DML03, DML05, DML07 and DML17 plotted versus assigned year.

7.4.2 Inter-site correlation and spatio-temporal distribution

Calculation of the cross-correlation coefficients of two ice core records for the same ionic component gives a first insight into the spatial variability and is a test for the similarity in multi-site records. The cross-correlation coefficient indicates how far the two parameters are linearly related to each other [Storch and Zwiers, 1999].

However, slight differences in dating can add disturbing noise to the pre-existing spatial variability and decrease the correlation coefficient. Therefore, low correlation coefficients do not necessarily mean that no relationship between the correlated parameters exists. In Table 7.1 the computed cross-correlation coefficients are presented.

Table 7.1: Inter-site cross-correlation coefficients.

Calculated inter-site cross-correlation coefficients between the four different sites DML03, DML05, DML07 and DML17 for MSA, nss-sulphate, chloride and sodium (bold font) for the time interval 1800 to 1900 A.D. Correlation coefficients higher than 0.117 are statistically significant on the 95% level. The values in italic font listed in the upper triangle of the subtables are correlation coefficients of the time series, where peaks determined by the peak detection algorithm (Chapter 5) have been replaced by the 30 years median values.

	DML03	DML05	DML07	DML17	Cl ⁻	DML03	DML05	DML07	DML17
MSA									
DML03	1	<i>0.20</i>	<i>0.18</i>	<i>0.30</i>	DML03	1	<i>0.32</i>	<i>0.12</i>	<i>0.32</i>
DML05	-0.04	1	<i>0.12</i>	<i>0.12</i>	DML05	0.40	1	<i>0.02</i>	<i>0.36</i>
DML07	0.13	0.22	1	<i>0.26</i>	DML07	-0.05	0.03	1	<i>0.04</i>
DML17	0.09	0.07	0.38	1	DML17	0.33	0.10	0.00	1
nssSO ₄ ²⁻	DML03	DML05	DML07	DML17	Na ⁺	DML03	DML05	DML07	DML17
DML03	1	<i>0.21</i>	<i>0.17</i>	<i>0.18</i>	DML03	1	<i>0.22</i>	<i>0.08</i>	<i>0.01</i>
DML05	0.61	1	<i>0.15</i>	<i>0.32</i>	DML05	0.38	1	<i>0.09</i>	<i>0.01</i>
DML07	0.71	0.79	1	<i>0.09</i>	DML07	-0.07	0.02	1	<i>0.07</i>
DML17	0.59	0.54	0.65	1	DML17	0.21	0.04	-0.01	1

The calculation revealed that 13 of the 24 coefficients are significant on the 95% level. The lack of similarity is most pronounced in the sea-salt compounds of the ice core at DML07, indicating that DML07 has different glacio-chemical characteristics. These low cross-correlation coefficients are in contrast to the observed uniform spatial variability from the snow pit samples in Chapter 6 and the uniform spatio-temporal distribution pattern shown in the Appendix B. Thus changes in atmospheric circulation patterns or deposition mechanisms can be excluded as being responsible for this observed discrepancy, but an alternative explanation can not be provided.

7.4.3 Single site, multiple component EOF analysis

One way to study the similarity of the ionic signature between the sampling sites is to compute multi-species EOFs, as performed in other studies [Meeker et al., 1997; Mayewski, 1997; Yiou et al., 1997]. The EOF analysis on the normalised records from each sampling site for the same time interval (1800 to 1997 A.D.) was also performed. To enable comparison, the ion records were normalised by subtracting the mean values and divided by the standard deviation for each record, so that the standard deviation for each ion specie is 1.

The dominant EOF modes (EOF1) express 30 to 43% of the variance, and together with EOF2 explain more than 60 % of the variance at all sampling sites. EOF1 is dominated at all sites by the sea-salt components, accounting at least 60% of the variance, with a similar contribution of chloride and sodium. This result implies, that variance in sea-salt content would effect all sites. It is indicating that atmospheric transport of marine air masses occurs homogeneously over the area under investigation.

The biogenic sulphur compounds, nss-sulphate and MSA, dominate EOF2. Higher contribution of nss-sulphate at sites with lower accumulation rates and vice versa supports, as in Chapter 6, the increasing influence of dry deposition at sites with low snow accumulation. This can be explained due to increase of nss-sulphate concentration the standard deviation rises also leading to higher variance. In the case of MSA no change dependent on variation in accumulation rate is observed, except for DML03 where higher MSA concentration leads to higher variance in the signal. The other sampling sites show similar variance contribution of MSA to EOF2.

Regarding the contribution to the variability of the sea-salt components at DML07, which is in same range as other, and the low correlation coefficients found in the section above for sea-salt at DML07, a lack of similarity cannot be observed in the EOF analysis.

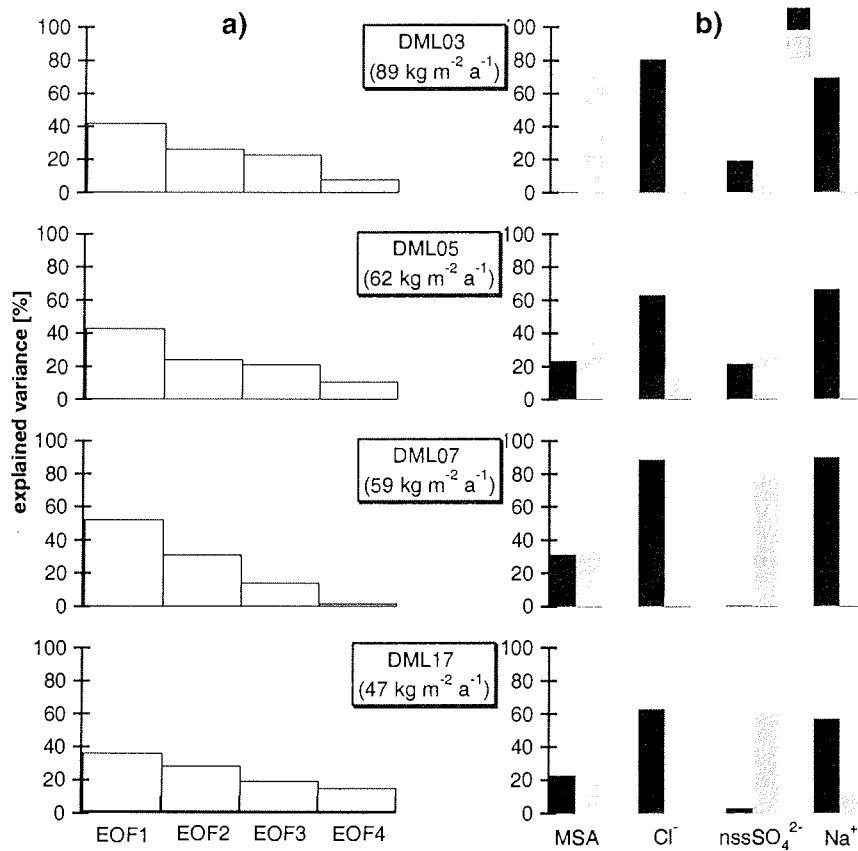


Figure 7.6: Explained variance of EOF1-EOF4 at each sampling site, and of each ion specie to EOF1 and EOF2.

Explained variance for EOF1-EOF4 of normalised data records at each sampling site (a), and the contribution of each ion component to the variance of EOF1 and EOF2 (b). While sea-salt components dominate EOF1 over the area under investigation, EOF2 is mainly explained by the biogenic sulphur components.

7.4.4 Multiple site, single component EOF analysis

In the previous section the dominant ionic species at each sampling site were presented. Moreover, it is interesting which sampling site does a certain ionic component dominate or do all sites have a similar contribution?

In Figure 7.7 the explained variances of the computed EOF's for each component are presented. For all components the first two EOF's explain about 60% of the variance. The contribution of each sampling site to EOF1 and EOF2 are also shown in Figure 7.7. In the case of MSA, all four sampling sites have a similar contribution to EOF1.

For nss-sulphate again all four sampling sites have a similar contribution to EOF1. The explained variance in the EOF2 is lower at sampling sites with high snow accumulation sites, i.e. DML03 and DML05, than that of lower accumulation, i.e. DML07 and DML17 (Figure 7.7).

For the sea-salt components sodium and chloride, all sampling sites contribute by a similar amount to EOF1, except the case of chloride at DML07. The lack of explained variance in chloride at DML07 indicates a different temporal evolution at DML07. While all other sampling sites are located either on or north of the main ice divide of Amundsenisen, DML07 is located on the lee-side. Comparing the chloride record at DML07 to the others, it shows no exception in the spatial variability (Chapter 6) and the spatio-temporal distribution (Appendix B), provides no explanation for this exception.

Altogether, all ionic components, in particular MSA, nss-sulphate, and sodium are well represented over the area under investigation. Chloride shows at DML07 an extraordinary performance, where no reason could be determined from transportation or deposition mechanisms. The mainly similar contribution of the records from each side to the variance imply that related climate parameters on Amundsenisen should be detectable in the time series (PC1), at least for MSA, nss-sulphate and sodium.

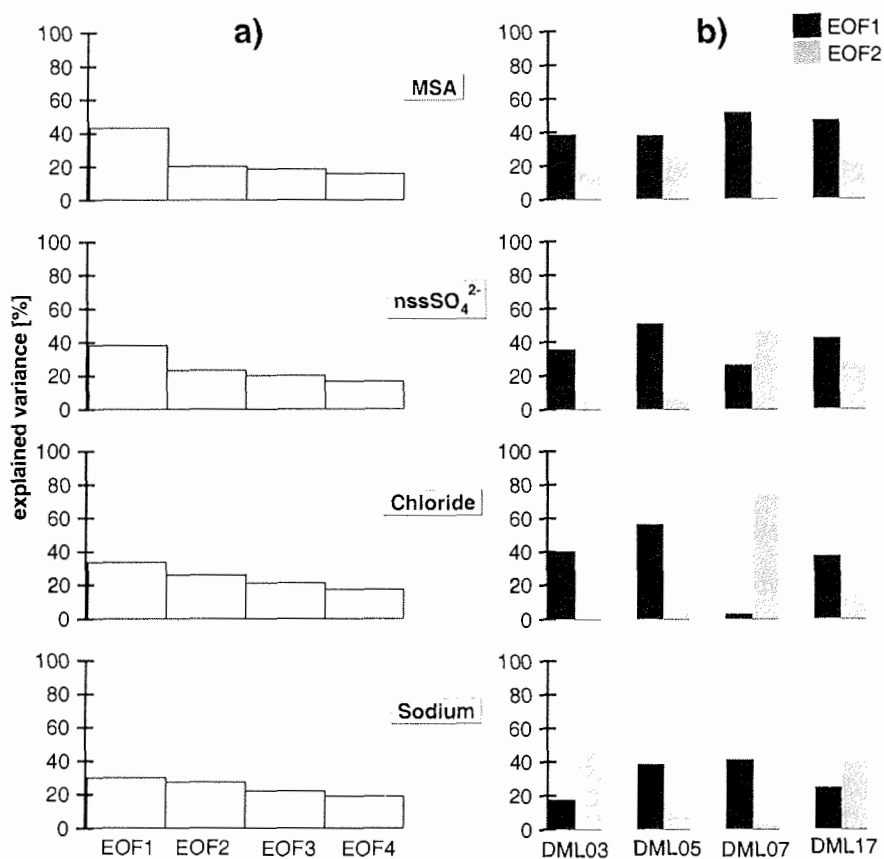


Figure 7.7: Explained variance of EOF1-EOF4 for each ionic component, and of each sampling site to EOF1 and EOF2.

Explained variance for EOF1-EOF4 of normalised data records for each ion specie (a), and the contribution of each sampling site to the variance of EOF1 and EOF2 (b).

7.4.5 Potential effect of El Niño on ice core records

7.4.5.1 Anatomy of an El Niño event and its global effects

The nature of the El Niño phenomenon has been described in numerous publications and will be described here briefly [Arntz and Fahrback, 1991; Tomczak and Godfrey, 1994; Covey and Hastenrath, 1978; Philander, 1990]. The evolution can be classified in five "phases". The first phase is called **antecedent phase**, assigned to the August-October period preceding an El Niño event in the following year. This phase is characterised by the Southwest Monsoon, which is active at this time of the year. This implies slightly higher SST values near Indonesia and Papua New Guinea (Figure 7.8), accompanied with high rainfall anomalies at these sites and an absolute SST maximum near Indonesia around 130°E.

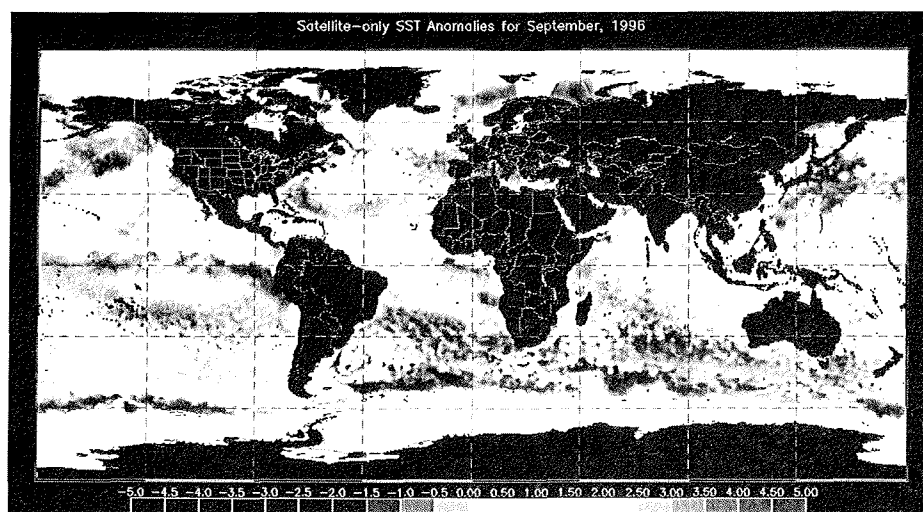


Figure 7.8: Global SST anomaly pattern in September 1996.

Between November and January the **onset phase** is observed, when the sun has crossed the equator, the Australian monsoon has started and the Southwest Monsoon died. Then, a slight cooling of SST by about 0.4°K for the Indonesian region and warming at 170°E, near Tahiti is observed (Figure 7.9). At this point it is decided whether an El Niño event develops or not. The event develops, if the usual convection centre at 130°E moves eastward to 170°E. This depends on the effects of wind speed on evaporative heat loss, the formation of wind stress, the temperature of up-welling water masses, the geostrophic flow and finally from wind

stress providing the mechanical energy for stirring deeper water in the surface water layer (so called mixed layer).

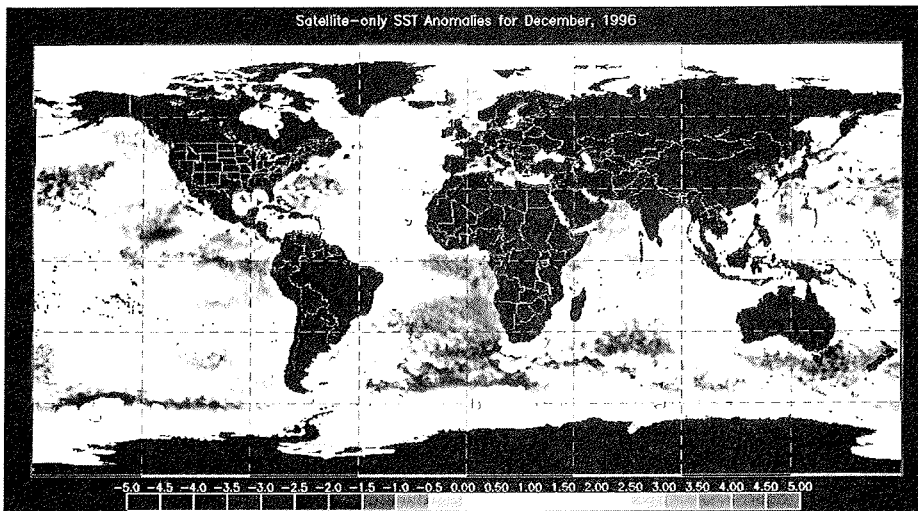


Figure 7.9: Global SST anomaly pattern in December 1996.

If the decision is made for evolving an El Niño event the **peak phase** is observed between March-May, characterised by westerly wind anomalies in the western Pacific region responsible for down-welling of cold and nutrient-rich deeper water layers and warm SST anomalies developing near South America. However, during the **transition phase** of an El-Niño year (May-June) the Southern Hemispheric convection starts to die and a new Southwest Monsoon develops, causing drastic changes in Pacific circulation. A significant SST anomaly develops in the South China Sea and the Indonesian waters, attracting winds from the far western Pacific Ocean which begins to blow eastward. The east Pacific SST anomalies dies shortly thereafter, which is called the **mature phase**, between December and January (Figure 7.10). Thus, an El Niño event lasts between 12 to 18 months and appeared in the last century with periodicities between 2-20 years.

The El Niño phenomenon is a natural climate variation, which changes the hydrospheric-atmospheric dynamics of the Pacific Ocean dramatically. The movement of the convergence zone causes dry conditions in the South Asian region. This exceptional drought at tropical rain forests leads to fires and devastates huge areas [Siegert et al., 2001]. On the east side of the Pacific Ocean heavy rainfall at Peru/Ecuador and northeast Brazil floods vast areas. The movement of warm water from the western to east Pacific region has biological consequences. This effects one

of the richest fishing areas of the globe, the coast of Peru/Ecuador. It decreases the fish content and starts the migration of a different species of fish into this area [Arntz and Fahrbach, 1991; Barber and Chavez, 1983]. The impacts of an El Niño event on India cause higher SST at the Bengalen coast and has important social consequences [Bouma and Pascual, 2001].

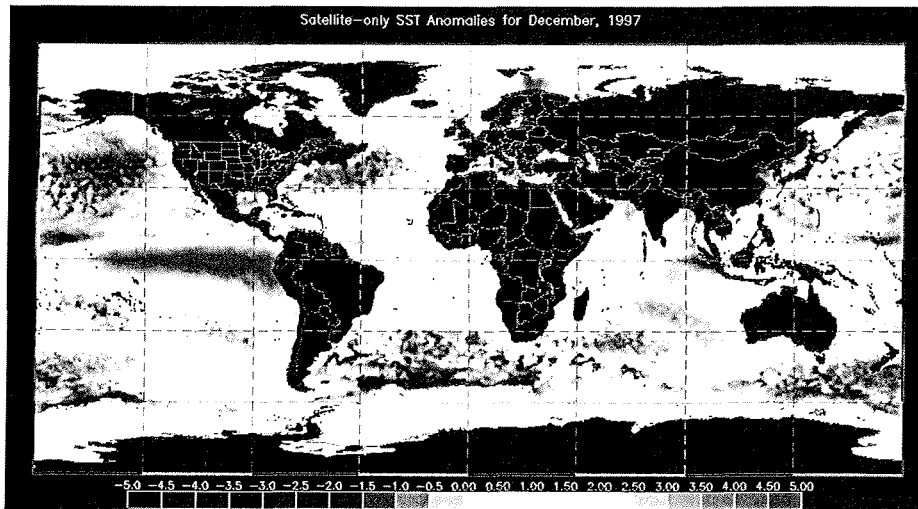


Figure 7.10: Global SST anomaly pattern in December 1997.

The study of impacts of El Niño on polar sites were limited by sparse data [Simmonds and Jacka, 1995], but Kwok and Comiso [2002] show that sea level pressure, sea-surface temperature and surface air temperature from Amundsen, Bellinghausen, and the Weddell Sea are related to El Niño associated activities in the equatorial Pacific. Sterl and Hazeleger [2001] found evidence of teleconnection between South Atlantic Ocean and the El Niño event via the Antarctic Circumpolar Current (ACC).

Legrand and Feniet-Saigne [1991] and Isaksson et al. [2001] have studied ice core records on El Niño signature, but without evidence of any relation between MSA concentration and sea-surface temperature in the associated source region, the phytoplankton content and a connection to El Niño.

7.4.5.2 EOF1 and PC1 of nss-sulphate and MSA

We have investigated four ice core records on their MSA and nss-sulphate concentrations. In case of nss-sulphate the nss-sulphate contribution of volcanic events were detected by the peak detection algorithm, presented in Chapter 5, replaced the peaks by the median values of a 30 year window around. This extraction of the volcanic part of nss-sulphate can be expected to be a good approximation of the loading of the background sulphate atmospheric aerosol.

The computed EOF1 explains 49% of MSA and 31% of nss-sulphate variance, while by EOF2 about 19% of the MSA and 21% of the nss-sulphate variance is described. Thus, the first two EOFs account more than 50% of the total variance of the signal. The contribution of each sampling sites to the EOFs is listed in Table 7.2.

Table 7.2: Contribution of MSA and nss-sulphate to EOF1.

Contribution of each sampling site to EOF1 of MSA and nss-sulphate for the time interval 1948 to 1997. All four sampling sites have similar contribution to EOF1 of MSA. Different contributions of each sampling site is observed to EOF1 for nss-sulphate. The largest contribution is from the sampling site DML03, followed by DML05. All four ice cores from our measurements explain altogether 87 % of the variance in EOF1 of nss-sulphate.

location	explained variance for EOF1 of MSA	explained variance for EOF1 of nss-sulphate
DML03	55	52
DML05	51	34
DML07	52	30
DML17	40	18
Swedarp	not available	20

The application of the sensitive peak detection algorithm on the MSA and nss-sulphate concentration records gave no significant match with the documented El Niño events compiled by Quinn and Neal [1987]. The approach taken by Isaksson et al. [2001] and Legrand and Feniet-Saigne [1991], without determining concentration limits for peak detection would not provide information about the relation of biogenic sulphur in ice cores to SST. Therefore, here an statistical argumentation is used to find a relationship and to quantify significance levels.

The corresponding principal components of EOF1 for MSA and nss-sulphate are presented in Figure 7.11. The asterisks in this plot mark years with strong to very strong El Niño events. The PC1 of the records are thought to be the common signal in all four ice core records, but no striking peaks can be observed coincidentally with El Niño events in the PC1s.

For the time evolution of EOF1 for MSA rather a post-depositional process can be detected than an El Niño signature. In the first ten years a sharp decrease, most probably due to post-depositional loss from the snow pack to air as discussed in Chapter 5 and 6, is observed, which even out for the older parts in the ice core. The correlation charts between MSA and SST, with associated SST anomalies and the wavelet spectrum were computed, supporting that the MSA signal is overlaid by post-depositional processes. Therefore, it is not further discussed.

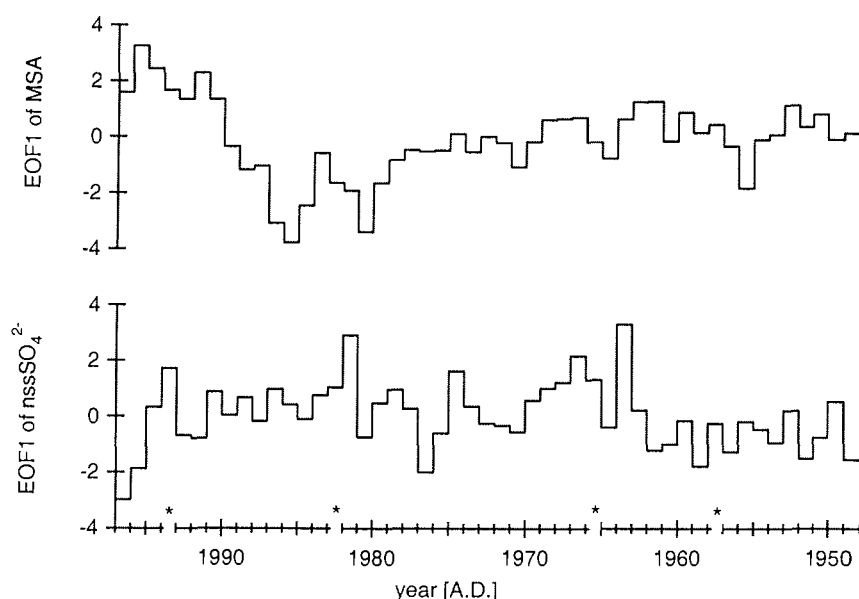


Figure 7.11: Principal components of EOF1 for MSA and nss-sulphate.

The principal components associated to EOF1 of MSA and nss-sulphate records versus year. The range is between -4 and 4 (without dimension) because the EOF's were computed from the normalised ion records. The asterisks indicate years with strong to very strong El Niño events.

7.4.5.3 Relation of MSA and nss-sulphate to SST

The computed PC1s of the ion species were correlated with the NCEP/NCAR SST data for the time period 1948 to 1991 A.D. The associated anomalies in the SST (the correlation charts) were derived. To be able to find evolutionary patterns in the correlation charts and the associated SST anomalies, lag regression for the PC1s was performed. The lag correlation was made by shifting the PC1 in that way, that the value in PC1 at year x is assigned to one year later, i.e. $x+1$, though PC1 is lagging the SST record [Storch and Zwiers, 1999]. Lag regression is done to

find an evolutionary pattern in a signal. For processes in the ocean on longer time scales than one year the oceans' memory should be considered: For example, during and El Niño event warm water masses are moved eastward (from Indonesia to the coast of Peru) in several month. The transport of these warm water masses north and south along the American coast until they Circumpolar Current, takes another couple of months [Tomczak and Godfrey, 1994].

Between nss-sulphate and SST correlation charts were calculated and are presented together with the associated SST anomalies in Figure 7.12 to Figure 7.13. The correlations charts show significant positive correlation at the 95% level (indicated with red lines in the plots) between 40°S and 60°S in the South Atlantic region. This means that increased nss-sulphate concentrations are observed in the ice cores when the SST rises in this area. The region, with correlation coefficients significant on the 95 % significance level in our result is in good agreement with the result of the trajectory studies by Reijmer [2001a].

Positive correlation coefficients found in other areas of the globe, e.g. from the low latitudes, do not mean, that those areas are interconnected with the ice core records from DML. Areas with positive correlation coefficients are related to each other due to teleconnection patterns of the SST, i.e. an increase in the SST observed in the south-west Atlantic Ocean is coincident with an increase in the SST at the equatorial Atlantic or Pacific Ocean.

Corresponding to this correlation charts it is possible to calculate the associated amplitude in the SST, i.e. the associated SST anomaly [Storch and Zwiers, 1999], which is presented in the lower plots in Figure 7.12 to Figure 7.13. This is done by calculating the standard deviation at each grid point of SST over the whole time interval covered by the NCEP/NCAR Reanalysis Project. This global SST anomaly map is multiplied with the correlation map, providing a SST anomaly pattern associated to the ice core records.

The observed SST anomaly shows little higher temperatures in the equatorial Pacific Ocean. The anomaly is reaches largest values for lag +1. This SST anomaly pattern for lag +1 looks similar to documented SST anomaly patterns during an El Niño event, in particular in the equatorial Pacific Ocean. Certainly, the maximum amplitudes here (0.3 K) are less pronounced than the observed (of 1.6 K observed between year 1950 to 1973 by Philander [1990]). Most probably this could be due to the low but nevertheless significant correlation coefficients.

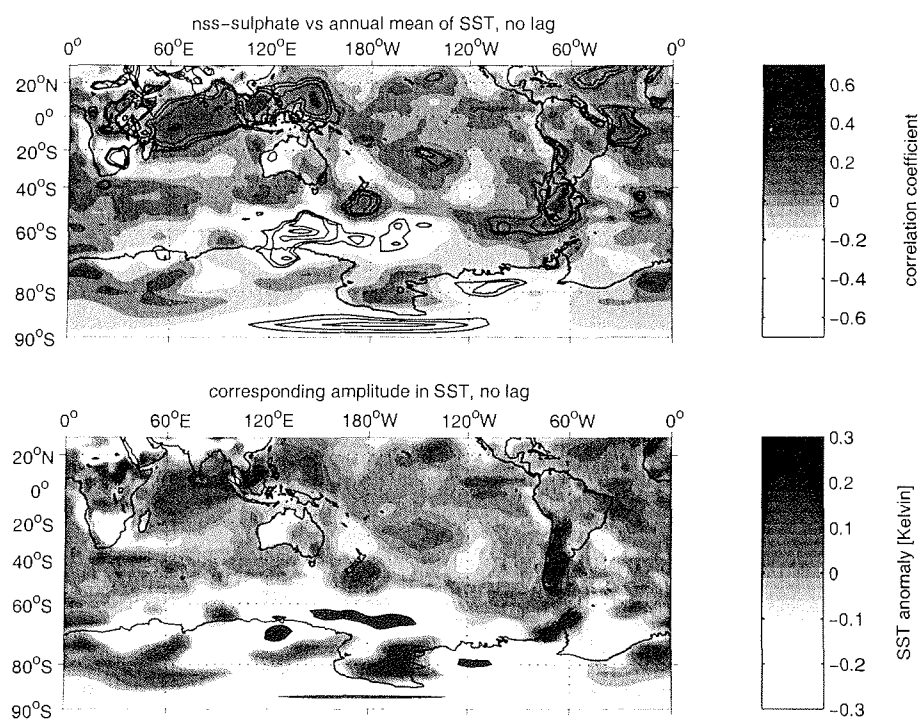


Figure 7.12: Correlation chart between PC1 of nss-sulphate and annual SST with zero lag, and associated SST anomaly.

The upper plot presents the correlation chart between PC1 of nss-sulphate and annual SST from NCEP/NCAR Reanalysis project over the time interval 1948 to 1991. The lower plot shows the associated amplitude to in the SST. The area between 40°S and 60°S in the Southern Atlantic Ocean shows again significant correlation between the two parameters.

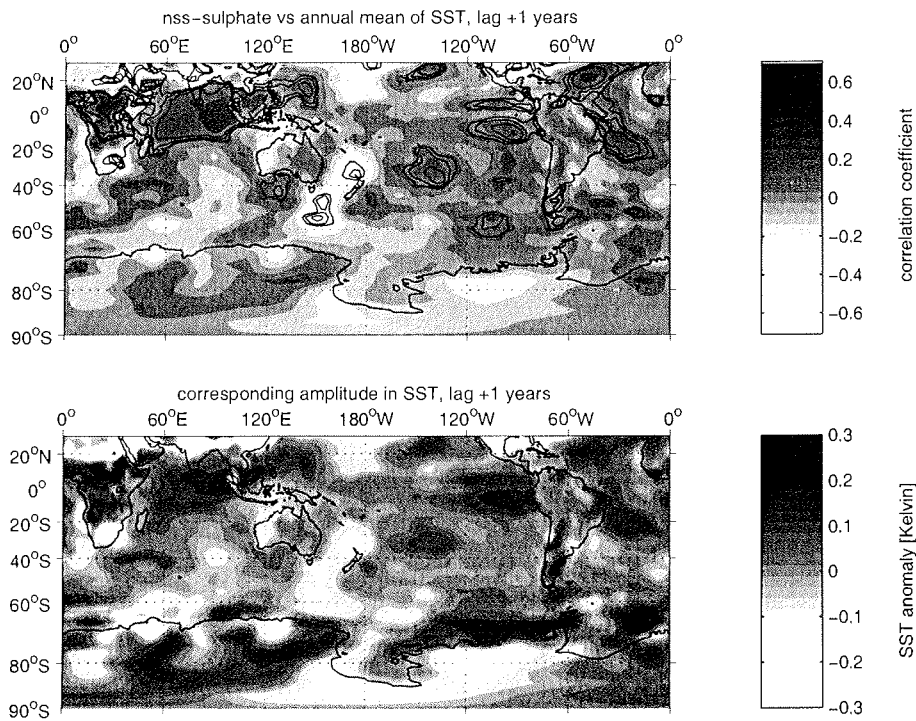


Figure 7.13: Correlation chart between PC1 of nss-sulphate and annual SST with lag +1, and associated SST anomaly.

The upper plot presents the correlation chart between PC1 of nss-sulphate and annual SST from NCEP/NCAR Reanalysis project over the time interval 1948 to 1991. The lower plot shows the associated amplitude to in the SST. The area between 40°S and 60°S in the Southern Atlantic Ocean shows significant correlation. This SST anomaly pattern is similar to pattern due to an El Niño event.

In conclusion, The highest nss-sulphate concentrations are observed when SST increase in the South Atlantic Ocean is observed. Application of lag regression result in maximum amplitude in the SST anomaly, similar to that caused by an El Niño event one year later. This do not mean, that nss-sulphate concentration for the year before have knowledge about the SST one year later, but this lag regression give the opportunity to investigate the oceans' memory on what SST anomaly pattern follows on a the calculated one with zero lag. For the 43 years investigated we found highest nss-sulphate concentrations coincident with increase of SST in the Southern Atlantic ocean. In the following year an El Niño event develops. This region drives not the El Niño event, but seems to be affected by its impact.

Sterl and Hazeleger [2001] and Venegas et al. [1998] found teleconnections between the South Atlantic Ocean and tropical Pacific regions, where the driving mechanisms for an El Niño event are located. The chlorophyll maps (Figure 7.1), reflecting the spatial distribution of phytoplankton, show in the South Atlantic Ocean higher concentrations for January 1999 (not an El Niño year) than for January 1998 (during the marture phase of an El Niño event). Altogether, indication of El Niño signature seems to be archived in the ice core records.

7.4.5.4 Wavelet power spectra of MSA, nss-sulphate, and SST

The analysis of the temporal signature of the data gives information about periods in the signal. In comparison to classical Fast Fourier Transformation giving information about the overall period, but nothing about its temporal evolution, the wavelet analysis detects change of periods over the observation time. With the assumption, that the source region of nss-sulphate is teleconnected to regions driving the El Niño phenomenon, wavelet power spectra were calculated of Niño Index 3, covering the area 5°S to 5°N and 90°W to 150°W and the time period 1871 to 1991 A.D. Wavelet analysis has been applied on the PC1 of nss-sulphate for the same time interval.

The wavelet power spectrum of the PC1 of nss-sulphate is presented in Figure 7.14. The black lines indicate the 95% significance level. The cone-of-influence is the concave black line over the plot, where variance is reduced due to computational reasons, and therefore no valuable information can be obtained outside of it.

The spectrum of the PC1 of nss-sulphate shows significant periodicities between 2 and 20 years over the whole plot, the time interval from 1875 to 1991. From 1890 to 1920, significant period is observed of 16 ± 4 years. This periodicity is split into a second one of 10 ± 2 years in the 1890s, lasting until the 1950s. The significance of the period is lost between 1950 and 1970, but evolved again in the 1970s, where the cone-of-influence is reached. Shorter periodicities of 2-4 years are observed between 1880 and 1900, missing until 1915 and evolved again with periodicities from 2-8 years until year 1960. After a short time interval of 10 years, significant periods around 4 years emerge, reaching scales between 2-8 years from 1970 to 1991.

The wavelet power spectrum of the Niño Index 3, covering the region 5°S to 5°N and 90°W to 150°W [Torrence and Webster, 1999], is shown in Figure 7.15. In this region the highest SST anomalies are observed. Again the 95% significance level is plotted. This spectrum shows in the time interval 1890 to 1940 significant periodicities between 12-20 years (missing until 1970s, where they evolved again). Significant periodicities of 2-8 years are observed in this spectrum from 1880 to 1960, with changing dominance. A shift from a 6 year to a 2-3 year periodicity is clearly detected around 1970, which evolves to periodicities between 2-8 years in the 1980s.

Altogether, an exact match between the both wavelet power spectra over the whole time period can not be stated, but could not be expected due to the found low correlation coefficients. An overlap of the 12-16 years periodicity is observed for the time interval 1890-1910. For the 3-4 years periodicity an overlap could be observed for the years 1880 to 1900, in the 1930s, and since 1970.

Even if a little agreement in the wavelet power spectra could be found, these

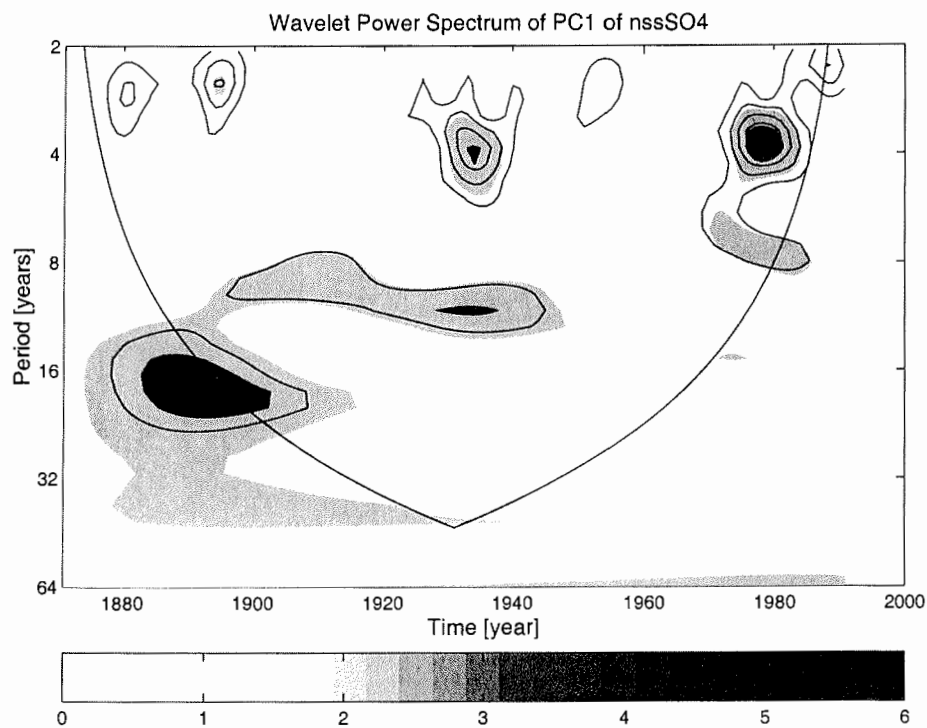


Figure 7.14: Wavelet power spectrum of PC1 of nss-sulphate.

The wavelet power spectrum of the principal component associated to the first EOF of nss-sulphate, computed by using the Morlet wavelet is presented. Significant periodicities inside of the cone-of-influence (the concave black line) are around 15 ± 5 years and 2 to 8 years.

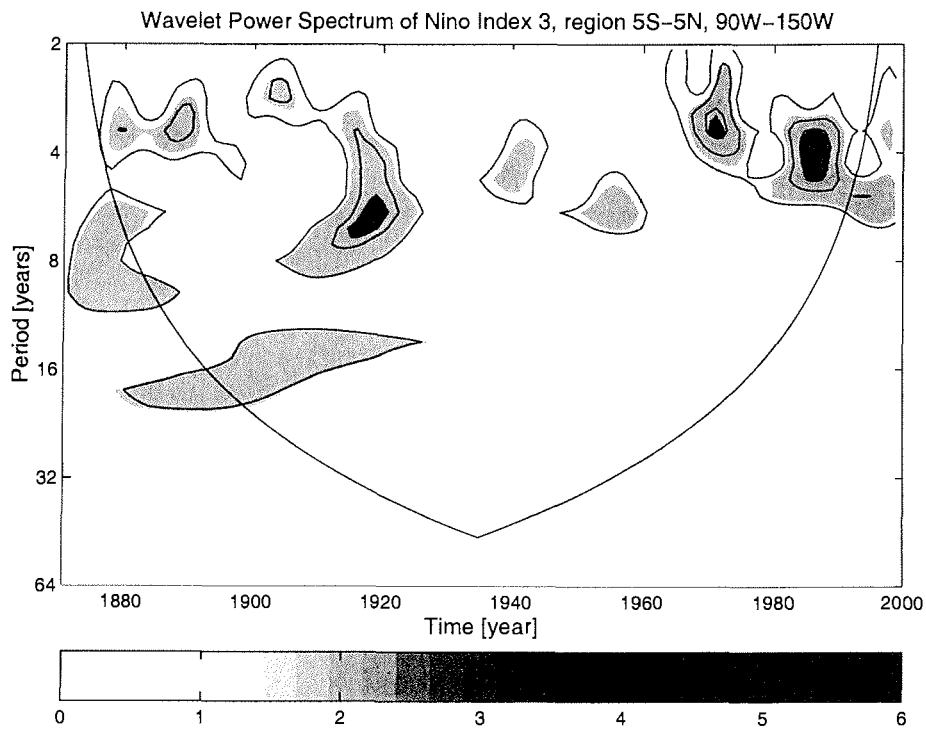


Figure 7.15: Wavelet power spectrum of the Nino 3 Index.

The wavelet power spectrum of the Nino 3 Index, computed by using the Morlet wavelet is presented. Significant periodicities inside of the cone-of-influence (the concave black line) are around 16 ± 4 years and 2-8 years.

periodicities do not have to be connected with each other. The coherence spectrum of the two records were computed to distinguish the correlation between the two periodicities (Figure 7.16). The variance of both records is plotted in Figure 7.16a) showing in both graphs a peak between the period of 3-4 years. In the coherence spectrum of these both records (Figure 7.16b), periods at 2.1, 3.3 and 4.3 years, are observed over the 95% significance level. That means, in both spectra, the wavelet power spectra and the coherence spectrum of the PC1 of nss-sulphate and the Nino Index 3, the periodicity of 2-4 years is coherently present.

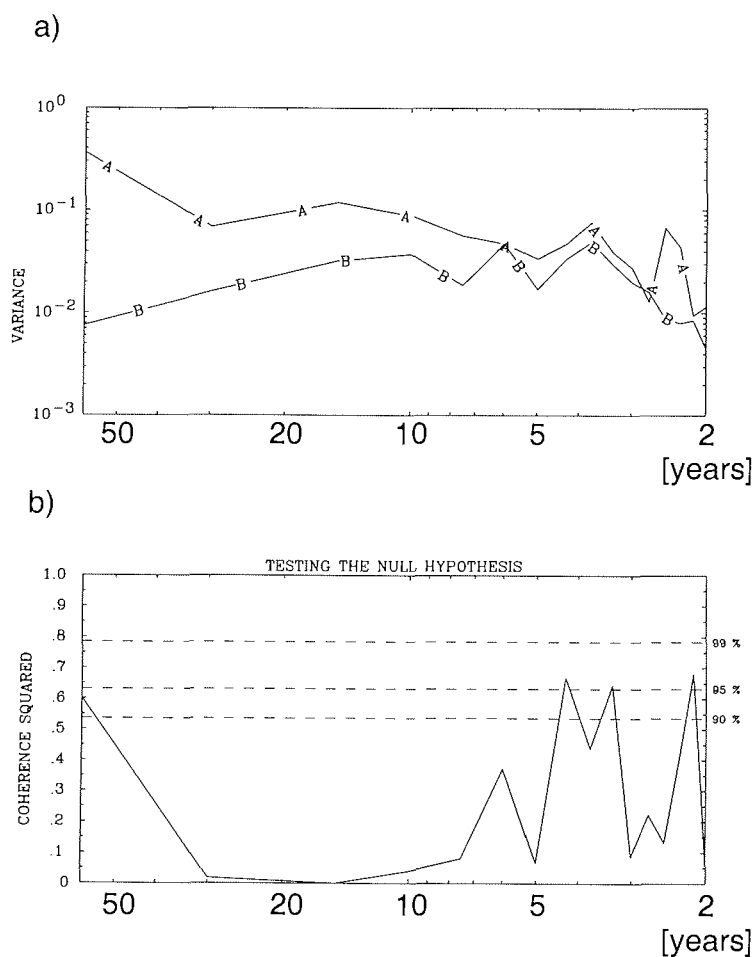


Figure 7.16: Coherence spectrum of PC1 of nss-sulphate with the Nino 3 Index.
The coherence spectrum of PC1 of nss-sulphate and the Nino 3 Index shows significant periods at 2.1 3.3. and 4.3 years.

7.5 Conclusions

The low inter-site correlation coefficients support the results from Sommer et al. [2000a], that local processes impede an obvious relationship between the ice core records. Application of signal decomposition by EOF analyses provided a common signal observed in all four intermediate deep ice cores.

In the PC1 of MSA effects of post-depositional loss could be observed. The correlation and regression analyses between the PC1 of nss-sulphate and NCEP/NCAR Reanalysis SST data led to positive correlation coefficients, giving evidence that increase in nss-sulphate concentrations are related to increasing temperature of the ocean surface. As result of the correlation charts the South Atlantic region between 40°S and 60°S showed with significant coefficients at 95% level, indicating that this is the source region for the biogenic sulphur deposited in the area under investigation. Besides that, the associated SST anomaly pattern looks similar to El Niño associated SST anomaly pattern, with lower anomaly values due to the relatively low correlation coefficients.

The wavelet power spectra of the PC1 of nss-sulphate and the Niño index 3 do not exactly match. An agreement of periods over observed time could be obtained with Niño Index 3, with significant periodicities between 2-8 years and 12-16 years. The computed coherence spectrum of both records showed significant coherent periodicities between 2-4 years.

In conclusion, the observed pattern in the associated SST anomaly and the detected periodicities imply that the El Niño signature is archived in the nss-sulphate records of the ice cores.

To extract the implicated El Niño signal, whether from the ion concentration records itself or on the principal component, it would be insightful to apply other analysis techniques, like the usage of a time filter or the computation of wavelet coherency.

Note, that also *canonical correlation analysis* (CCA) and *Redundancy analysis* (RA) was performed to study the correlation structure between an ion specie and a climate parameter. While CCA tries to maximise the correlation, RA identifies patterns which are strongly linked by maximising the correlation and the variance of the two parameters. The RA is a so called predictor-predictand method, e.g. using the ice cores as predictor and looks for its best represented pattern in the predictand, here SST. This method has been developed in the late 1970s, and has been recently introduced into climate research by [1999] Storch and Zwiers.

With both methods no significant results could be achieved. One reason could be the autocorrelation of this time series. i.e. the concentration in one year is not

totally independent of that from the year before. Another reason could be, that the turn of the year could not be exactly placed at the same time of the year, due to the discontinuous accumulation on Amundsenisen. It would be insightful to study the strength and quality of these statistical methods, at least without the last mentioned problem, on ice cores, e.g. from Greenland.

Chapter 8

Conclusions and outlook

In order to assess the representativeness of the new EPICA deep ice core, the glacio-chemical and glacio-meteorological characteristics of Amundsenisen, the plateau area of Dronning Maud Land, Antarctica, have been investigated in this study using four intermediate deep ice cores and 21 snow pits.

The spatial distribution of the ionic components showed an essentially homogeneous pattern, which in the case of sulphate deposition revealed an additional increase with decreasing snow accumulation rate. In contrast, MSA showed a systematic decrease probably related to a postdepositional MSA net loss. With regard to the deep ice core, which is located on an ice divide, no spatial corrections are necessary due to negligible upstream effects, however a quantitative interpretation of the MSA due to negligible upstream effects, however a quantitative interpretation of the MSA record requires further studies on the postdepositional loss observed.

The accumulation rates are sufficiently large to provide information about seasonal variations of the chemical records. In high resolution records the seasonal maximum of the sea-salt components could be found in the winter period, of MSA in late summer to beginning of winter and double peaks of sulphate in the summer period.

Furthermore, annual layer counting of the ice core at DML05, located 2 km west of the present deep drilling site, could be performed enabling an accurate dating at least for the past 2000 years and most probably for the complete Holocene time period.

In addition quantitative evidence for an uniform volcanic sulphate deposition could be given. This result was essential for the reliable reconstruction of a chronology of the volcanic history for the last 2000 years, in particular for the poorly documented Southern Hemispheric volcanic eruptions. With this ice core chronology the uncertainty of the assigned years to the eruptions could be reduced from up to ± 150 years to less than ± 22 years. Accordingly, the deep ice core could provide

a unique chronology of volcanic eruptions for the entire Holocene.

The spatio-temporal distribution of the ionic species revealed no change in the atmospheric transport pattern of marine air masses on the Plateau. At DML07 significant changes were monitored in the isotope content and ion concentrations. These observations can most probably be explained by effects of wind scouring and not by changes in the atmospheric circulation pattern. At DML05, i.e. close to the deep drilling site, no evidence for such effects was found.

The investigation of the imprint of the sea-surface temperature (SST) on the biogenic sulphur species nss-sulphate and MSA, showed that processes on local or regional scale overlay the influence of SST. The PC1 of MSA implied again a post-depositional loss in the first 10 years which most probably compromises the information about the relationship between MSA and SST.

Nevertheless, a low but significant correlation could be found between nss-sulphate and SST. The correlation chart indicates the region between 40°S and 60°S in the Southern Atlantic Ocean as the source region for biogenic sulphur deposited on Amundsenisen. The associated SST anomaly pattern to this correlation revealed that this region is teleconnected to the El Niño phenomenon. The associated SST anomaly pattern looks similar to the global SST anomaly pattern, indicating an El Niño signature is archived in ice cores from Amundsenisen, but is only of secondary importance compared to processes of local or regional scale.

The results of this work are valuable for the dating and interpretation of the future deep ice core from Amundsenisen, Dronning Maud Land, Antarctica, which is presently in the drilling process. The deep ice core will be representative for the area under investigation. Under the assumption, the glacio-chemical record at DML05 is not changed, it can be expected that annual layer counting of the ice core will be feasible for the Holocene time period, allowing as well to obtain an unique volcanic chronology for the Southern Hemisphere.

Interpretation of MSA requires further studies of the post-depositional migration process in the snow pack while the nss-sulphate record potentially enables to detect a long-term El Niño signature. At this point, further application of statistical and mathematical analyses would be insightful, e.g. wavelet-coherence analysis, filter analysis, fingerprint method, etc.

The sodium record, which is a conservative sea-salt tracer, should be investigated on its relation to wind speed over the ocean. This would be insightful to evaluate, whether systematic effects of climate periods (such as the Little Ice Age) on sea salt concentrations are observed as stated in other studies. First statistical analyses of sodium and wind speed records in this work revealed positive correlation, but could

not followed further on.

The presented ice core records represent an important validation data set for other climatological analyses and climate models trying to detect teleconnection patterns on regional and global scales, e.g. the Antarctic Circumpolar Wave, the El Niño phenomenon, etc. Furthermore, the comparison of this data set with data from other climate archives could broaden the knowledge about recent and past climate changes and the processes teleconnecting various sites on the Southern Hemisphere.

Bibliography

- Allison, I., G. Wendler and U. Radock (1993). A climatology of the East Antarctic ice sheet (100°E to 140°E) derived from automatic weather stations, *J. Geophys. Res.* **98**(D5), 8815–8823.
- Andreae, M. O. (1990). Ocean-atmosphere interactions in the global biogeochemical sulfur cycle, *Marine Chem.* **30**, 1–29.
- Arntz, W. A. and E. Fahrbach (1991). *El Niño - Klimaexperiment der Natur*, 1 edition, Birkhäuser Verlag.
- Baliunas, S., P. Frick, D. Sokoloff and W. Soon (1997). Time scales and trends in the Central England temperature data (1659-1990): A wavelet analysis, *Geophys. Res. Lett.* **24**(11), 1351–1354.
- Barber, R. T. and F. P. Chavez (1983). Biological consequences of El Niño, *Science* **222**, 1203–1210.
- Barrodale, L., D. Skea, M. Berkley, R. Kuwahara and R. Poeckert (1993). Warping digital images using thin plate splines, *Pattern Recognition* **26**(2), 375–376.
- Barry, R. G. and R. J. Chorley (1992). *Atmosphere, Weather and Climate*, 1 edition, Routledge.
- Bates, T. S., B. K. Lamb, A. Guenther, J. Dignon and R. E. Stoiber (1992). Sulfur emissions to the atmosphere from natural sources, *J. Atmos. Chem.* **14**, 315–337.
- Bluth, G. J. S., C. C. Schnetzler, A. J. Krueger and L. S. Walter (1993). The contribution of explosive volcanism to global atmospheric sulphur dioxide concentrations, *Nature* **366**, 327–329.
- Bouma, M. J. and M. Pascual (2001). Seasonal and interannual cycles of endemic cholera in bengal 1891-1940, *Hydrobiologia* **460**(1-3), 147–156.

- Broeke, M. v. d. (2000). The semiannual oscillation and the Antarctic climate, part 5: impact on the annual temperature cycle as derived from NCEP/NCAR re-analysis, *Climate Dynamics* **16**, 369–377.
- Broeke, M. v. d., J.-G. Winther, E. Isaksson, J. F. Pinglot, L. Karlöf, T. Eiken and L. Conrads (1999). Climate variables along a traverse line in Dronning Maud Land, East Antarctica, *J. Glaciol.* **45**(150), 295–302.
- Bromwich, D. H. (1988). Snowfall in high southern latitudes, *Rev. Geophys.* **26**(1), 149–168.
- Carey, S. and H. Sigurdsson (1982). Influence of particle aggregation on deposition of distal tephra from May 18, 1980 eruption of Mount St. Helens volcano, *J. Geophys. Res.* **87**, 7061–7072.
- Charlson, R. J., J. E. Lovelock, M. O. Andreae and S. G. Warren (1987). Oceanic phytoplankton, atmospheric sulphur, cloud albedo and climate, *Nature* **326**, 655–661.
- Cole-Dai, J., E. Mosley-Thompson and L. G. Thompson (1997). Annually resolved southern hemisphere volcanic history from two Antarctic ice cores, *J. Geophys. Res.* **102**(D14), 16,761–16,771.
- Cole-Dai, J., L. G. Thompson and E. Mosley-Thompson (1995). A 485 year record of atmospheric chloride, nitrate and sulfate: results of chemical analysis of ice cores from Dyer Plateau, Antarctic Peninsula, *Ann. Glaciol.* **21**, 182–188.
- Covey, D. L. and S. Hastenrath (1978). The pacific El Niño phenomenon and the Atlantic circulation, *Monthly Weather Rev.* **106**, 1280–1281.
- Dansgaard, W. et al. (1993). Evidence for general instability of past climate from a 250-kyr ice-core record, *Nature* **364**, 218–220.
- Daubechies, I. (1990). The wavelet transform, time-frequency localization and signal analysis, *IEEE T. Inform. Theory* **36**(5), 961–1005.
- Davidson, C. I., M. H. Bergin and H. D. Kuhns (1996). The deposition of particles and gases to ice sheets, in Wolff, E. W. and R. C. Bales (ed.), *Chemical Exchange Between the Atmosphere and Polar Snow*, Vol. I 43 of *NATO ASI Series*, Springer-Verlag, Berlin, Heidelberg, pp. 275–306.
- Davison, B. M. and A. G. Allen (1994). A method for sampling dimethylsulfide in polluted and remote marine atmospheres, *Atmos. Environ.* **28**(10), 1721–1729.

- Davison, B. M., C. N. Hewitt, C. D. O'Dowd, J. A. Lowe, M. H. Smith, M. Schikowski, U. Baltensperger and R. M. Harrison (1996). Dimethyl sulfide, methane sulfonic acid and physicochemical aerosol properties in Atlantic air from the United Kingdom to Halley Bay utilities, *J. Geophys. Res.* **101**(D17), 22,855–22,867.
- De Angelis, M., J. P. Steffensen, H. Clausen and C. U. Hammer (1997). Primary aerosol (sea salt and soil dust) deposited in Greenland ice during the last climate cycle: Comparison with East Antarctic records, *J. Geophys. Res.* **102**(C12), 26,681–26,698.
- Delmas, R. J. (1982). Antarctic sulphate budget, *Nature* **299**, 677–678.
- Delmas, R. J., M. Legrand, A. J. Aristarain and F. Zanolini (1985). Volcanic deposits in Antarctic snow and ice, *J. Geophys. Res.* **D7**, 12,901–12,920.
- Delmas, R. J., S. Kirchner, J. M. Palais and J.-R. Petit (1992). 1000 years of explosive volcanism recorded at the South Pole, *Tellus* **44B**, 335–350.
- DIONEX (1997). *Installation instructions and troubleshooting guide for the anion self-regenerating Suppressor-II (4mm)*, DIONEX Corporation, California, USA. No. 031141.
- DomeF (1998). Deep ice-core drilling at dome fuji and glaciological studies in east Dronning Maud Land, Antarctica, *Ann. Glaciol.* **29**, 215–219.
- Drewry, D. J., S. R. Jordan and E. Jankowski (1982). Measured properties of the Antarctic ice sheet: surface configuration, ice thickness, volume and bedrock, characteristics, *Ann. Glaciol.* **3**, 83–91.
- Fischer, H. (1997). *Räumliche Variabilität in Eiskernzeitreihen Nordostgrönland (Rekonstruktion klimatischer und luftchemischer Langzeittrends seit 1500 A.D.)*, PhD thesis, University of Heidelberg, Germany.
- Fischer, H. and D. Wagenbach (1998a). Sulfate and nitrate firn concentrations on the Greenland ice sheet: 1. Large-scale geographical deposition changes, *J. Geophys. Res.* **103**(D17), 21,927–21,934.
- Fischer, H. and D. Wagenbach (1998b). Sulfate and nitrate firn concentrations on the Greenland ice sheet 2: Temporal anthropogenic deposition changes, *J. Geophys. Res.* **103**(D17), 21,935–21,942.

- Friend, J. P., A. R. Bandy, J. L. Moyers, W. H. Zoller, R. E. Stoiber, A. Torres, W. I. jr. Rose, M. P. McCormick and D. C. Woods (1982). Research on atmospheric volcanic emissions: an overview, *Geophys. Res. Lett.* **9**(9), 1101–1104.
- Genthon, C. (1992). Simulations of desert dust and sea-salt aerosols in Antarctica with a general circulation model of the atmosphere, *Tellus* **44**(B), 371–389.
- Gerland, S., H. Oerter, J. Kipfstuhl, F. Wilhelms, H. Miller and W. Miners (1999). Density log of a 181 m long ice core from Berkner Island, Antarctica, *Ann. Glaciol.* **29**, 215–219.
- Glen, J. W. and J. G. Paren (1975). The electrical properties of snow and ice, *J. Glaciol.* **15**(73), 15–38.
- Göktaş, F. (2002). *Characterisation of glacio-chemical and glacio-meteorological parameters on Amundsenisen, Dronning Maud Land, Antarctica*, submitted, University of Bremen.
- Göktaş, F., H. Fischer, H. Oerter, R. Weller, S. Sommer and H. Miller (2002). A glacio-chemical characterisation of the new deep drilling site on Amundsenisen, Dronning Maud Land, Antarctica, *Ann. Glaciol.*
- Göktaş, F., H. Oerter, H. Fischer, R. Weller, W. Graf and H. Miller (2002). High resolution chronology of earth's volcanic history: implications for changes in small scale climate condition, *J. Geophys. Res.*
- Götting, K.-J., E. F. Kilian and R. Schnetter (1982). *Einführung in die Meeres - biologie 1*, 1 edition, Friedr. Vieweg & Sohn.
- Graedel, T. E. and P. J. Crutzen (1994). *Chemie der Atmosphäre*, 1 edition, Spektrum Akademischer Verlag, Heidelberg, Berlin, Oxford.
- Graf, W., O. Reinwarth, H. Oerter, C. Mayer and A. Lambrecht (1999). Surface accumulation on Foundation Ice Stream, *Ann. Glaciol.* **29**, 23–28.
- Gross, G. W., I. C. Hayslip and R. N. Hoy (1978). Electrical conductivity and relaxation in ice crystals with known impurity content, *J. Glaciol.* **21**, 143–160.
- Guelle, W., M. Schulz, Y. Balkanski and F. Dentener (2001). Influence of the source formulation on modeling the atmospheric global distribution of sea salt aerosol, *J. Geophys. Res.* **106**(D21), 27,509–27,524.

- Hammer, C. U. (1977). Past volcanism revealed by Greenland ice sheet impurities, *Nature* **270**, 482–486.
- Hammer, C. U. (1980). Acidity of polar ice cores in relation to absolute dating, past volcanism, and radio-echoes, *J. Glaciol.* **25**, 359–372.
- Herterich, K. (1993). *Role of ice sheets and sea level*, John Wiley and Sons Ltd., pp. 189–197.
- Hou, S., Q. Dahe and R. Jiawen (1999). Different post-depositional processes of NO_3^- in snow layers in East Antarctica and on the northern Qinghai-Tibetan Plateau, *Ann. Glaciol.* **29**, 73–76.
- Huybrechts, P., D. Steinhage, F. Wilhelms and J. Bamber (2000). Balance velocities and measured properties of the Antarctic ice sheet from a new compilation of gridded data for modelling, *Ann. Glaciol.* **30**, 52–60.
- Isaksson, E. (1994). *Climate records from shallow firn cores, Dronning Maud Land, Antarctica*, PhD thesis, Department of Physical Geography, University of Stockholm, Sweden.
- Isaksson, E., E. Karlen, P. Mayewski, M. Twickler and S. Whitlow (2001). A high-altitude snow chemistry record from Amundsenisen, Dronning Maud Land, Antarctica, *J. Glaciol.* **47**(158), 489–496.
- Isaksson, E., M. R. van den Broeke, J.-G. Winther, L. Karlöf, J. F. Pinglot and N. Gundestrup (1999). Accumulation and proxy-temperature variability in Dronning Maud Land, Antarctica, determined from shallow firn cores, *Ann. Glaciol.* **29**, 17–22.
- Isaksson, E., N. G. W. Karlén, P. Mayewski, S. Whitlow and M. Twickler (1996). A century of accumulation and temperature changes in Dronning Maud Land, Antarctica, *J. Geophys. Res.* **101**(D3), 7085–7094.
- Ito, T. (1995). Nature and Origin of Antarctic Submicron Aerosols, in Delmas, R. (ed.), *Ice Core Studies of Global Biogeochemical Cycles*, Vol. I 30 of *NATO ASI Series*, Springer-Verlag, Berlin Heidelberg, pp. 23–38.
- Ivey, J. P., D. M. Davies, V. Morgan and G. P. Ayers (1986). Methanesulphonate in Antarctic ice, *Tellus* **38B**, 375–379.
- Jaenicke, R. and L. Schütz (1988). Aerosol Physics and Chemistry, in Fischer, G. (ed.), *Landolt-Börnstein: Numerical Data and Functional Relationship in*

- Science and Technology*, Vol. 4: Meteorology, Subvol. b: Physical and Chemical Properties of the Air of *New Series, Group V: Geophysics and Space Research*, Springer, New York, pp. 391–457.
- Jones, G., M. A. J. Curran, H. B. Swan, R. M. Greene, F. B. Griffiths and L. A. Clementson (1998). Influence of different water masses and biological activity on dimethylsulphide and dimethylsulphoniopropionate in the subantarctic zone of the Southern Ocean during ACE 1, *J. Geophys. Res.* **103**(D13), 16,691–16,701.
- Jones, P. D. and D. W. S. Limbert (2001). A data base of Antarctic surface temperature and pressure data, *technical report*, U.S. Department of Energy, Washington, D.C.
- Karlöf, L. et al. (2000). A 1500 year record of accumulation at Amundsenisen western Dronning Maud Land, Antarctica, derived from electrical and radioactive measurements on a 120 m ice core, *J. Geophys. Res.* **105**(D10), 12,471–12,483.
- Kirchner, S. and R. J. Delmas (1988). A 1000 year glaciochemical study at the South Pole, *Ann. Glaciol.* **10**, 80–84.
- König-Langlo, G., J. C. King and P. Pettre (1998). Climatology of the three coastal Antarctic stations Dumont d'Urville, Neumayer, and Halley, *J. Geophys. Res.* **103**(D9), 10,935–10,946.
- Kreutz, K. J., P. A. Mayewski, L. D. Meeker, M. S. Twickler and S. I. Whitlow (1997). Bipolar changes in atmospheric circulation during the Little Ice Age, *Science* **277**(5330), 1294–1296.
- Kumar, P. and E. Foufoula-Georgiou (1997). Wavelet analysis for geophysical applications, *Rev. Geophys.* **35**(4), 385–412.
- Kwok, R. and J. C. Comiso (2002). Southern ocean climate and sea ice anomalies associated with the Southern Oscillation, *J. Climate*.
- Langway, C. C. j., H. B. Clausen and C. U. Hammer (1988). An interhemispheric volcanic time-marker in ice cores from Greenland and Antarctica, *Ann. Glaciol.* **10**, 102–108.
- Langway, C. C. j., K. Osada, H. B. Clausen, C. U. Hammer and H. Shoji (1995). A 10-century comparison of prominent bipolar volcanic events in ice cores, *J. Geophys. Res.* **100**(D8), 16,241–26,247.

- Langway, C. C. j., K. Osada, H. B. Clausen, C. U. Hammer, H. Shoji and A. Mitani (1994). New chemical stratigraphy over the last millenium for Byrd Station, Antarctica, *Tellus* **46B**(1), 40–51.
- Langway, C. C. j., M. M. Herron and J. H. Cragin (1974). Chemical profile of the Ross ice sheet at Little America, *J. Glaciol.* **13**, 431–435.
- Lau, K.-M. and H. Weng (1995). Climate signal detection using wavelet transform: how to make a time series sing, *B. Am. Meteorol. Soc.* **76**(12), 2391–2402.
- Legrand, M. (1995). Sulphur-derived species in polar ice: A review, in Delmas, R. (ed.), *Ice Core Studies of Global Biogeochemical Cycles*, Vol. I 30 of *NATO ASI Series*, Springer-Verlag, Berlin Heidelberg, pp. 91–119.
- Legrand, M. and C. Feniet-Saigne (1991). Methanesulfonic acid in south polar snow layers: A record of strong El Nino, *Geophys. Res. Lett.* **18**(2), 187–190.
- Legrand, M. and D. Wagenbach (1999). Impact of the Cerro Hudson and Pinatubo volcanic eruptions on the Antarctic air and snow chemistry, *J. Geophys. Res.* **104**(D1), 1581–1596.
- Legrand, M. and P. A. Mayewski (1997). Glaciochemistry of polar ice cores: a review, *Rev. Geophys.* **35**(3), 219–243.
- Legrand, M. and R. J. Delmas (1987). A 220-year continuous record of volcanic H₂SO₄ in the Antarctic ice sheet, *Nature* **327**, 671–676.
- Legrand, M., C. U. Hammer, M. de Angelis, J. Savarino, R. Delmas, H. B. Clausen and S. J. Johnsen (1997). Sulfur-containing species (methanesulfonate and SO₄) over the last climatic cycle in the Greenland Ice Core Project (central Greenland) ice core, *J. Geophys. Res.* **102**(C12), 26,663–26,679.
- Legrand, M. R. and R. J. Delmas (1986). Relative contributions of tropospheric and stratospheric sources to nitrate in Antarctic snow, *Tellus* **38B**, 236–249.
- Legrand, M. R. and R. J. Delmas (1988). Formation of HCl in the Antarctic atmosphere, *J. Geophys. Res.* **93**(D6), 7153–7168.
- Legrand, M. R. and S. Kirchner (1990). Origins and variations of nitrate in south polar precipitation, *J. Geophys. Res.* **95**(D4), 3493–3507.
- Looyenga, H. (1965). Dielectric constants of heterogeneous mixture, *Physica* **31**(3), 401–406.

- Matrai, P. A. and M. Vernet (1997). Dynamics of the vernal bloom in the marginal ice zone of the Barents Sea: Dimethyl sulfide and dimethylsulfoniopropionate budgets, *J. Geophys. Res.* **102**(C10), 22,965–22,979.
- Matrai, P., M. Vernet, R. Hood, A. Jennings, E. Brody and S. Saemundsdottir (1995). Light-dependence of carbon and sulfur production by polar clones of the genus *phaeocystis*, *Marine Biology* **124**(1), 157–167.
- Mayewski, P. (1997). Major features and forcing of high-latitude northern hemisphere atmospheric circulation using a 110,000-year long glaciochemical series, *J. Geophys. Res.* **102**(C12), 26,345–26,366.
- McCormick, M. P., L. W. Thomassen and C. R. Trepte (1995). Atmospheric effects of the Mt. Pinatubo eruption, *Nature* **373**, 399–404.
- Meeker, L. D., P. A. Mayewski, M. S. Twickler, S. I. Whitlow and D. Meese (1997). A 110,000-year history of change in continental biogenic emissions and related atmospheric circulation inferred from the Greenland Ice Sheet Project ice core, *J. Geophys. Res.* **102**(C12), 26,489–26,504.
- Menon, S., V. K. Saxena, P. Durkee, B. N. Wenny and K. Nielsen (2002). Role of sulfate aerosols in modifying the cloud albedo: a closure experiment, *Atmos. Res.* **61**, 169–187.
- Minikin, A., D. Wagenbach, W. Graf and J. Kipfstuhl (1994). Spatial and seasonal variations of the snow chemistry at the central Filchner-Ronne Ice Shelf, Antarctica, *Ann. Glaciol.* **20**, 283–290.
- Minikin, A., M. Legrand, J. Hall, D. Wagenbach, C. Kleefeld, E. Wolff, E. Pasteur and F. Ducroz (1998). Sulfur-containing species (sulfate and methane-sulfonate) in coastal Antarctic aerosol and precipitation, *J. Geophys. Res.* **103**(D9), 10,975–10,990.
- Moore, J. and J. Paren (1987). New technique for dielectric logging of Antarctic ice cores, *J. Phys. (Colloque C1)* **48**(3), 155–160.
- Moore, J. C. and S. Fujita (1993). Dielectric properties of ice containing acid and salt impurity at microwave and low frequencies, *J. Geophys. Res.* **98**(B6), 9769–9780.
- Moore, J. C., E. W. Wolff, H. B. Clausen and C. U. Hammer (1992). The chemical basis for the electrical stratigraphy of ice, *J. Geophys. Res.* **97**(B2), 1887–1896.

- Moore, J. C., H. Narita and N. Maeno (1991). A continuous 770-year record of volcanic activity from East Antarctica, *J. Geophys. Res.* **96**(D9), 17,353–17,359.
- Mulvaney, R., D. Wagenbach and E. W. Wolff (1998). Postdepositional change in snowpack nitrate from observation of year-round near-surface snow in coastal Antarctica, *J. Geophys. Res.* **103**(D9), 11,201–11,031.
- Newhall, C. G. and S. Self (1982). The Volcanic Explosivity Index VEI: An Estimate of Explosive Magnitude for Historical Volcanism, *J. Geophys. Res.* **87**(C2), 1231–1238.
- Noone, D., J. Turner and R. Mulvaney (1999). Atmospheric signals and characteristics of accumulation in Dronning Maud Land, Antarctica, *J. Geophys. Res.* **104**(D16), 19,191–19,211.
- Oerter, H., F. Wilhelms, F. Jung-Rothenhäusler, F. Göktas, H. Miller, W. Graf and S. Sommer (2000). Accumulation rates in Dronning Maud Land, Antarctica, as revealed by dielectric-profiling measurements of shallow firn cores, *Ann. Glaciol.* **30**, 27–34.
- Oerter, H., W. Graf, F. Wilhelms, A. Minikin and H. Miller (1999). Accumulation studies on Amundsenisen, Dronning Maud Land, Antarctica, by means of tritium, dielectric profiling and stable-isotope measurements: first results from the 1995-96 and 1996-97 field seasons, *Ann. Glaciol.* **29**, 1–9.
- Palais, J. M., S. Germani and G. A. Zielinski (1992). Inter-hemispheric transport of volcanic ash from a 1259 A.D. volcanic eruption to the Greenland and Antarctic ice sheets, *Geophys. Res. Lett.* **19**(8), 801–804.
- Palais, J. M., S. Kirchner and R. J. Delmas (1990). Identification of some global volcanic horizons by major elements analysis of fine ash in Antarctic ice, *Ann. Glaciol.* **14**, 216–220.
- Palmer, A. S., T. D. van Ommen, M. J. Curran, V. Morgan, J. M. Souney and P. A. Mayewski (2001). High-precision dating of volcanic events (A.D. 1301-1995) using ice cores from Law Dome, Antarctica, *J. Geophys. Res.* **106**(D22), 28,089–28,095.
- Pasteur, E. C. and R. Mulvaney (2000). Migration of methane sulphonate in Antarctic firn and ice, *J. Geophys. Res.* **105**(D9), 11,525–11,534.

- Pasteur, E. C., R. Mulvaney, D. A. Peel, E. S. Saltzman and P.-Y. Whung (1995). A 340 year record of biogenic sulphur from the Wedell Sea area, Antarctica, *Ann. Glaciol.* **21**, 169–174.
- Paterson, W. S. B. (1998). *The physics of glaciers*, 4th edition, Butterworth-Heinemann, Oxford, Great Britain.
- Peixoto, J. P. and A. H. Oort (1992). *Physics of climate*, 4th edition, American Institute of Physics.
- Perrier, V., T. Philipovitch and C. Basdevant (1995). Wavelet spectra compared to fourier spectra, *J. Math. Phys.* **36**(3), 1506–1519.
- Petit, J. R. et al. (1999). Climate and atmospheric history of the past 420,000 years from the Vostok ice core, Antarctica, *Nature* **399**, 429 – 436.
- Petit, J. R., J. W. C. White, N. W. Young, J. Jouzel and Y. S. Korotkevich (1982). Deuterium excess in recent Antarctic snow, *J. Geophys. Res.* **96**(D3), 5113–5122.
- Philander, S. G. (1990). *El Niño, La Niña, and the Suthern Oscillation*, 1 edition, Academic Press, London, United Kingdom.
- Picciotto, E., G. Crozaz and W. de Breuck (1971). Accumulation on the South Pole-Queen Maud Land traverse, 1964-1968, in Crary, A. (ed.), *Antarctic snow and ice studies II*, Antarctic Research Series 16, American Geophysical Union, Washington, D.C., pp. 257–315.
- Quinn, W. and V. T. Neal (1987). El Niño occurrences over the past four and half centuries, *J. Geophys. Res.* **92**(C13), 14,449–14,461.
- Raisbeck, G. M., F. Yiou, M. Furneau, J. M. Loiseaux, M. Lieuvin and J. C. Ravel (1981). Cosmogenic $^{10}\text{Be}/^7\text{Be}$ as a probe of atmospheric transport process, *Geophys. Res. Lett.* **8**, 1015–1018.
- Rampino, M. R. and S. Self (1982). Historic eruptions of Tambora (1815), Krakatau (1883), and Agung (1963), their stratospheric aerosols, and climate impact, *Quaternary Res.* **18**, 127–143.
- Rankin, A. M., V. Auld and E. W. Wolff (2000). Frost flowers as a source of fractionated sea salt aerosol in the polar regions, *Geophys. Res. Lett.* **27**(21), 3469–3472.

- Reijmer, C. H. (2001a). *Antarctic Meteorology - A study with automatic weather stations*, PhD thesis, University of Utrecht, Netherlands.
- Reijmer, C. H. and M. van den Broeke (2001b). Moisture sources of precipitation in Western Dronning Land, Antarctica, *Antarct. Sci.* **13**(2), 210–220.
- Reijmer, C. H., M. R. van den Broeke and M. P. Scheele (2001c). Air parcel trajectories to five deep drilling locations on Antarctica, based on the ERA-15 data set, *J. Climate*.
- Robock, A. (2000). Volcanic eruptions and climate, *Rev. Geophys.* **38**, 191–219.
- Rohde, H. (1999). Human impact on the atmospheric sulfur balance, *Tellus* **51 A-B**, 110–122.
- Röthlisberger, R. et al. (2002). Nitrate in Greenland and Antarctic ice cores: a detailed description of post-depositional processes, *Ann. Glaciol.*
- Saltzman, E. (1995). Ocean/atmosphere cycling of dimethylsulfide, in Delmas, R. J. (ed.), *Ice Core Studies of Global Biogeochemical Cycles*, Vol. I 30 of *NATO ASI Series*, Springer-Verlag, Berlin, Heidelberg, pp. 65–89.
- Saltzman, E., P.-Y. Whung and P. Mayewski (1997). Methanesulfonate in the Greenland Ice Sheet Project 2 ice core, *J. Geophys. Res.* **102**(C12), 26,649–26,657.
- SCAR (2002). Scientific Committee on Antarctic Research, <http://www.scar.org>.
- Schäfer, J. M., S. Ivy-Ochs, R. Wieler, I. Leya, H. Baur, G. H. Denton and C. Schlüchter (1999). Cosmogenic noble gas studies in the oldest landscape on earth: surface exposure ages of the Dry Valleys, Antarctica, *Earth Planet. Sc. Lett.* **167**(3-4), 215–226.
- Schlesinger, W. H. (1997). *Biogeochemistry: an analysis of global change*, 1 edition, Academic Press.
- Schminke, H.-U. (1993). Transfer von festen, flüssigen und gasförmigen Stoffen aus Vulkanen in die Atmosphäre, *Z. Umweltchem. Ökotox.* **5**(1), 27–40.
- Schultes, S., M. Levasseur, S. Michaud, G. Cantin, G. Wolfe, M. Gosselin and S. de Mora (2000). Dynamics of dimethylsulfide production from dissolved dimethylsulfoniopropionate in the Labrador Sea, *Mar. Ecol. Prog. Ser.* **202**, 27–40.

- SeaWiFS (n.d.). Sea-viewing Wide Field-of-view Sensor (SeaWiFS), <http://seawifs.gsfc.nasa.gov>.
- Siegert, F., G. Rucker, A. Hinrichs and A. A. Hoffmann (2001). Increased damage from fires in logged forests during droughts caused by El Niño, *Nature* **414**, 437–440.
- Sigg, A., K. Fuhrer, M. Anklin, T. Staffelbach and D. Zurmühle (1994). A continuous analysis technique for trace species in ice cores, *Environ. Sci. Technol.* **28**(2), 204–209.
- Simkin, T. and L. Siebert (1993). *Volcanoes of the World*, Geoscience Press, Tucson, Arizona.
- Simmonds, I. and T. H. Jacka (1995). Relationship between the interannual variability of Antarctic sea ice and the Southern Oscillation, *J. Climate* **8**, 637–647.
- Simó, R. and C. Pedrós-Alió (1999). Role of vertical mixing in controlling the oceanic production of dimethyl sulphide, *Nature* **402**, 396–398.
- Simó, R., C. Pedrós-Alió, G. Malin and J. O. Grimalt (2000). Biological turnover of DMS, DMSP and DMSO in contrasting open-sea waters, *Mar. Ecol. Prog. Ser.* **203**, 1–11.
- Sommer, S., D. Wagenbach, R. Mulvaney and H. Fischer (2000a). Glacio-chemical study spanning the past 2 kyr on three ice cores from Dronning Maud Land, Antarctica: 2. Seasonally resolved chemical records, *J. Geophys. Res.* **105**(D24), 29,423–29,433.
- Sommer, S. et al. (2000b). Glacio-chemical study spanning the past 2kyr on three ice cores from Dronning Maud Land, Antarctica: 1. Annually resolved accumulation rates, *J. Geophys. Res.* **105**(D24), 29,411–29,421.
- Stauffer, B. (1999). Cornucopia of ice core results, *Nature* **399**, 412 – 413.
- Steinhage, D. (2000). *Beiträge aus geophysikalischen Messungen in Dronning Maud Land, Antarktis, zur Auffindung eines optimalen Bohrpunktes für eine Eiskerntiefbohrung*, PhD thesis, University of Bremen, Germany.
- Stenberg, M., E. Isaksson, M. Hansson, W. Karlén, P. M. Mayewski, M. S. Twickler, S. I. Whitlow and N. Gundestrup (1998). Spatial variability of snow chemistry in western Dronning Maud Land, Antarctica, *Ann. Glaciol.* **27**, 378–384.

- Sterl, A. and W. Hazeleger (2001). Patterns and mechanisms of air-sea interaction in the South Atlantic Ocean, *J. Climate*.
- Stocker, T. F. (1998). The seasaw effect, *Science* **282**(5386), 61–62.
- Stocker, T. F. (2000). Past and future reorganizations in the climate system, *Quaternary Sci. Rev.* **19**, 301–319.
- Storch, H. v. and F. Zwiers (1999). *Statistical analyses in climate research*, 1 edition, Cambridge University Press.
- Tabacco, I. E., A. Passerini, F. Corbelli and M. Gorman (1998). Determination of the surface and bed topography at Dome C, East Antarctica, *J. Glaciol.* **44**(146), 185–191.
- Tabazadeh, A. and R. P. Turco (1993). Stratospheric chlorine injections by volcanic eruptions: HCl scavenging and implications for ozone, *Science* **260**, 1082–1086.
- Takahashi, S., T. Kameda, H. Enomoto, T. Shiraiwa, Y. Kodama, S. Fujita, H. Motoyama and O. Watanabe (1998). Automatic weather station program during Dome Fuji Project by JARE in East Dronning Maud Land, Antarctica, *Ann. Glaciol.* **27**, 528–534.
- Tomczak, M. and J. S. Godfrey (1994). *Regional oceanography: an introduction*, 1 edition, Pergamon Press, Elsevier Science Ltd., Frome and London, Great Britain.
- Torrence, C. and P. J. Webster (1999). *J. Climate* **12**, 2679–2690.
- Venegas, S. A., L. A. Mysak and D. N. Straub (1998). An interdecadal climate cycle in the South Atlantic and its links to other ocean basins, *J. Geophys. Res.* **103**(C11), 24,723–24,736.
- Wagenbach, D., F. Ducroz, R. Mulvaney, L. Keck, A. Minikin, M. Legrand, J. S. Hall and E. W. Wolff (1998a). Sea-salt aerosol in coastal Antarctic regions, *J. Geophys. Res.* **103**(D9), 10,961–10,974.
- Wagenbach, D., M. Legrand, H. Fischer, F. Pichlmayer and E. W. Wolff (1998b). Atmospheric near-surface nitrate at coastal Antarctic sites, *J. Geophys. Res.* **103**(D9), 11,007–11,020.
- Wagnon, P., R. J. Delmas and M. Legrand (1999). Loss of volatile acid species from upper firn layers at Vostock, Antarctica, *J. Geophys. Res.* **104**(D3), 3423–3431.

- Wang, B. and Y. Wang (1996). Temporal structure of the Southern Oscillation as revealed by waveform and wavelet analysis, *J. Climate* **9**, 1586–1598.
- Weiss, J. (1985). *Handbuch der Ionenchromatographie*, 1 edition, VCH Verlagsgesellschaft, Weinheim.
- Wilhelms, F. (1996). *Leitfähigkeits- und Dichtemessung an Eisbohrkernen*, Master's thesis, University of Bonn.
- Wilhelms, F., J. Kipfstuhl, H. Miller, K. Heinloth and J. Firestone (1998). Precise dielectric profiling of ice cores: a new device with improved guarding and its theory, *J. Glaciol.* **44**(146), 171–174.
- Wolff, E. W. (1995). Nitrate in polar ice, in Delmas, R. J. (ed.), *Ice core studies of global biogeochemical cycles*, Vol. I 30 of *NATO ASI Series*, Springer-Verlag, Berlin, etc, pp. 195–224.
- Wolff, E. W., I. Basile, J. Petit and J. Schwander (1999). Comparison of Holocene electrical records from Dome C and Vostock, *Ann. Glaciol.* **29**, 89–93.
- Yin, F., D. Grosjean and J. H. Seinfeld (1990). Photo-oxidation of Dimethyl Sulfide and Dimethyl Disulfide: I: Mechanism Development, *J. Atmos. Chem.* **11**, 309–364.
- Yiou, P., K. Fuhrer, L. D. Meeker, J. Jouzel, S. J. Johnsen and P. A. Mayewski (1997). Paleoclimatic variability inferred from the spectral analysis of Greenland and Antarctic ice core data, *J. Geophys. Res.* **102**(C12), 26,441–26,454.
- Zielinski, G., P. A. Mayewski, L. D. Meeker, K. Grönvold, M. S. Germani, S. Whitlow, M. S. Twickler and K. Taylor (1997). Volcanic aerosol records and tephrochronology of the Summit, Greenland, ice cores, *J. Geophys. Res.* **102**(C12), 26,625–26,640.

List of Figures

1.1	Map of Antarctica.	11
1.2	EPICA-DML pre-site survey.	12
2.1	Map from the poles to latitude of 30°.	16
2.2	Cross sections of the surface altitude in DML.	16
2.3	Location of automatic weather stations (AWS) on Dronning Maud Land.	18
2.4	Temperature at DML05.	18
2.5	Accumulation record from AWS9.	20
2.6	Aerosol transport mechanisms to Antarctica.	23
3.1	Cold laboratory set up.	31
3.2	Core cutting scheme.	32
3.3	Setup of IC measurement.	34
3.4	Anion method for IC measurements.	35
3.5	Cation method for IC measurements.	36
3.6	Baseline of anion and cation system.	38
3.7	Accuracy of IC measurements.	40
4.1	Map of Dronning Maud Land.	45
4.2	DEP conductivity profiles of ice cores B31, B32 and B33.	47
4.3	DEP profiles of firn cores from DML.	49
4.4	DEP profile of firn core FB9810.	51
4.5	Time series of accumulation rates.	55
4.6	Map of accumulation rates.	57
4.7	Accumulation rate versus 10 m firn temperature.	58
4.8	Time series of $\delta^{18}\text{O}$	59
5.1	Area under investigation in DML.	66
5.2	Identification of nss-sulphate peaks as volcanic events.	70
5.3	Comparison of DEP with nss-sulphate record.	72
5.4	Fingerprint of two volcanic eruptions.	74

5.5	Spatial distribution of volcanic signal.	75
5.6	Age to depth relation for DML05, DML07, and CV.	84
5.7	$\delta^{18}\text{O}$ profiles from DML05, DML07 and CV.	85
5.8	Ionic composition, $\delta^{18}\text{O}$ and deuterium excess for B31 at DML07 and B32 at DML05.	86
6.1	Dronning Maud Land in Antarctica.	90
6.2	Investigated Area in DML.	91
6.3	IC and CFA measurements of sodium.	95
6.4	SS9905 and upper part of B32 at DML05.	97
6.5	Snow pit SS9908.	99
6.6	Spatial distribution of chemical species.	101
7.1	Map of biogenic activity of the Ocean in December 1997 and July 1998.	110
7.2	Oxidation pathways of DMSP and DMS.	112
7.3	Area under investigation in DML.	113
7.4	Network of measurements taken by oceanographic research vessels. . .	114
7.5	Annual ion concentrations of MSA and nss-sulphate.	117
7.6	Explained variance of EOF1-EOF4 at each sampling site, and of each ion specie to EOF1 and EOF2.	120
7.7	Explained variance of EOF1-EOF4 for each ionic component, and of each sampling site to EOF1 and EOF2.	122
7.8	Global SST anomaly pattern in September 1996.	123
7.9	Global SST anomaly pattern in December 1996.	124
7.10	Global SST anomaly pattern in December 1997.	125
7.11	Principal components of EOF1 for MSA and nss-sulphate.	127
7.12	Correlation chart between PC1 of nss-sulphate and annual SST with zero lag, and associated SST anomaly.	129
7.13	Correlation chart between PC1 of nss-sulphate and annual SST with lag +1, and associated SST anomaly.	130
7.14	Wavelet power spectrum of PC1 of nss-sulphate.	133
7.15	Wavelet power spectrum of the Nino 3 Index.	134
7.16	Coherence spectrum of PC1 of nss-sulphate with the Nino 3 Index. .	135
A.1	Annual ion concentrations of MSA and nss-sulphate covering the time period 1800 to 1997 A.D.	163
A.2	Annual ion concentrations of MSA and nss-sulphate covering the time interval 0 to 1997 A.D.	164

A.3	Annual ion concentrations of chloride and sodium covering the time period 1800 to 1997 A.D.	165
A.4	Annual ion concentrations of chloride and sodium covering the time interval 0 to 1997 A.D.	166
B.1	Spatio-temporal distribution from 1800 to 1997 A.D.	168
B.2	Spatio-temporal distribution from 1500 to 1997 A.D.	169
B.3	Spatio-temporal distribution from 500 to 1997 A.D.	170

List of Tables

3.1	Process and vial blank concentrations.	37
4.1	Coordinates for drill locations.	46
4.2	Volcanic events identified in the ice cores.	48
4.3	Long-term accumulation rates.	52
4.4	Firn cores and snow pits sampled in 1997/1998.	54
5.1	Overview of sampling sites.	67
5.2	List of ice cores considered in our study	77
5.3	Volcanic H ₂ SO ₄ deposition and assigned eruptions from 1997 to 1800.	78
5.4	Volcano chronology and H ₂ SO ₄ deposition from 1800 to 165	82
6.1	Tabular list of sampling sites in DML.	92
6.2	Tabular list of process and vial blank and sample values.	94
7.1	Inter-site cross-correlation coefficients.	118
7.2	Contribution of MSA and nss-sulphate to EOF1.	126

Appendix

Appendix A

Data

A. The biogenic sulphur components

I) Data records covering the time period 1800 to 1997 A.D.

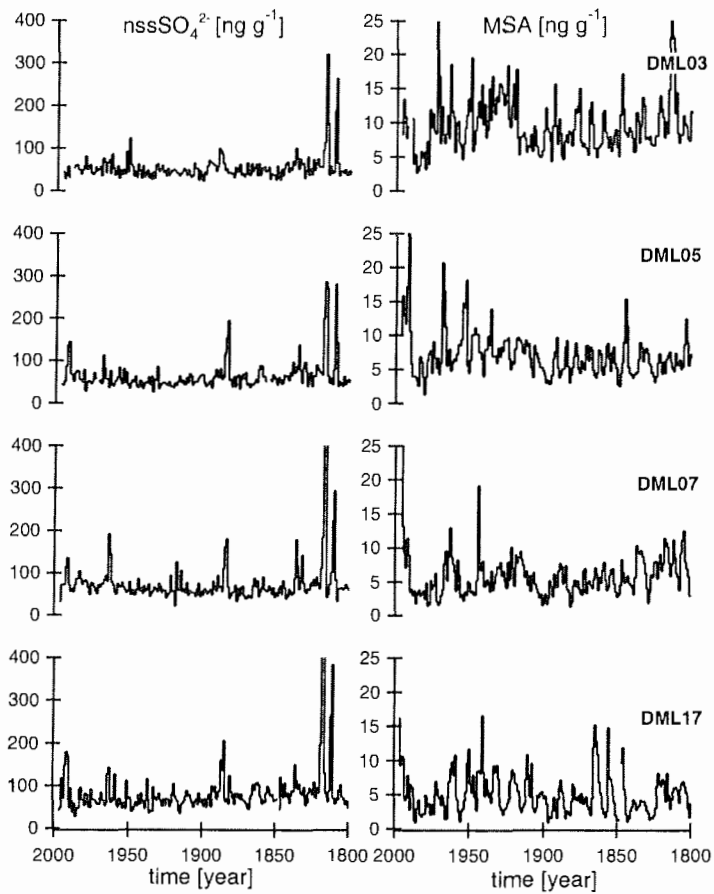


Figure A.1: Annual ion concentrations of MSA and nss-sulphate covering the time period 1800 to 1997 A.D.

Annual mean ion concentration records of MSA and nss-sulphate at DML03, DML05, DML07 and DML17 plotted versus assigned year.

II) Data records covering the time period 0 to 1997 A.D.

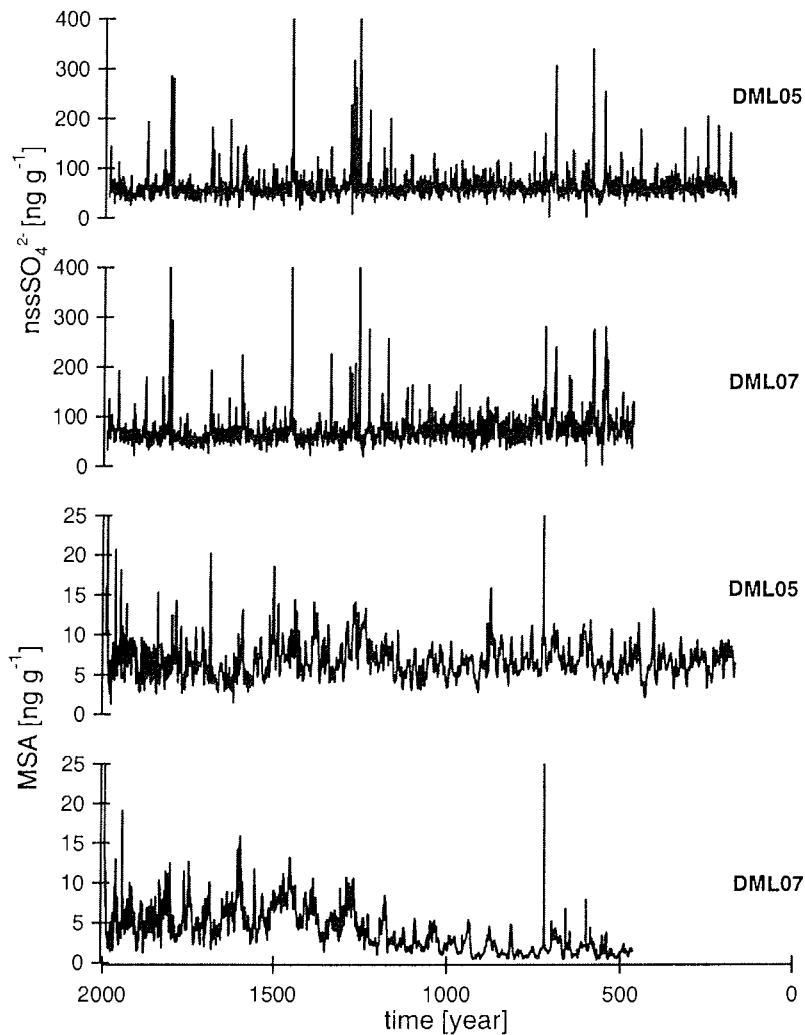


Figure A.2: Annual ion concentrations of MSA and nss-sulphate covering the time interval 0 to 1997 A.D..

Annual mean ion concentration records of MSA and nss-sulphate at DML03, DML05, DML07 and DML17 plotted versus assigned year.

B. The sea-salt components

I) Data records covering the time period 1800 to 1997 A.D.

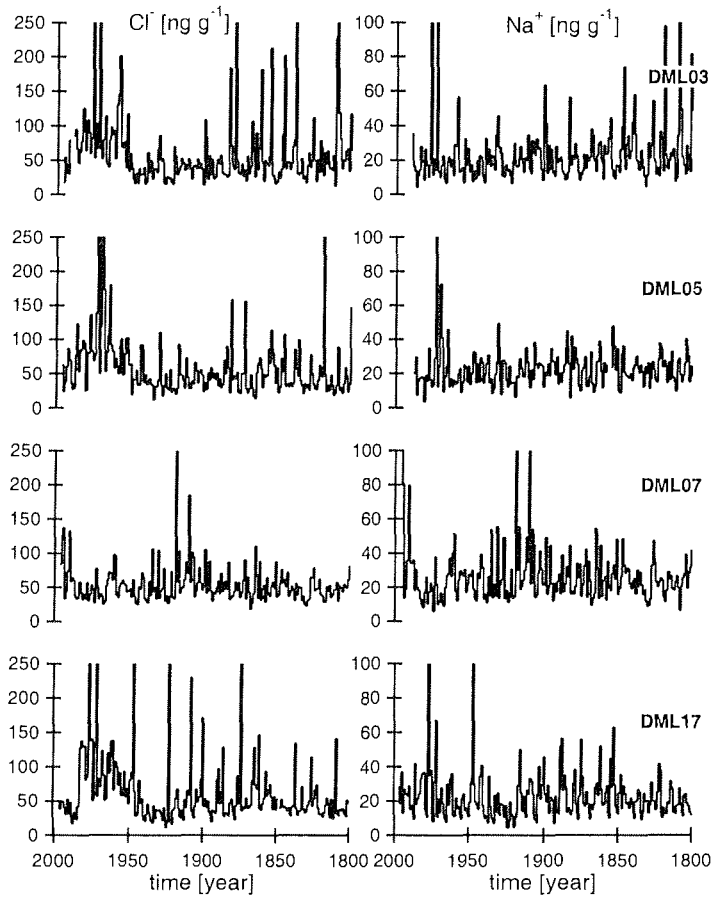


Figure A.3: Annual ion concentrations of chloride and sodium covering the time period 1800 to 1997 A.D.

Annual mean ion concentration records of chloride and sodium at DML03, DML05, DML07 and DML17 plotted versus assigned year.

II) Data records covering the time period 0 to 1997 A.D.

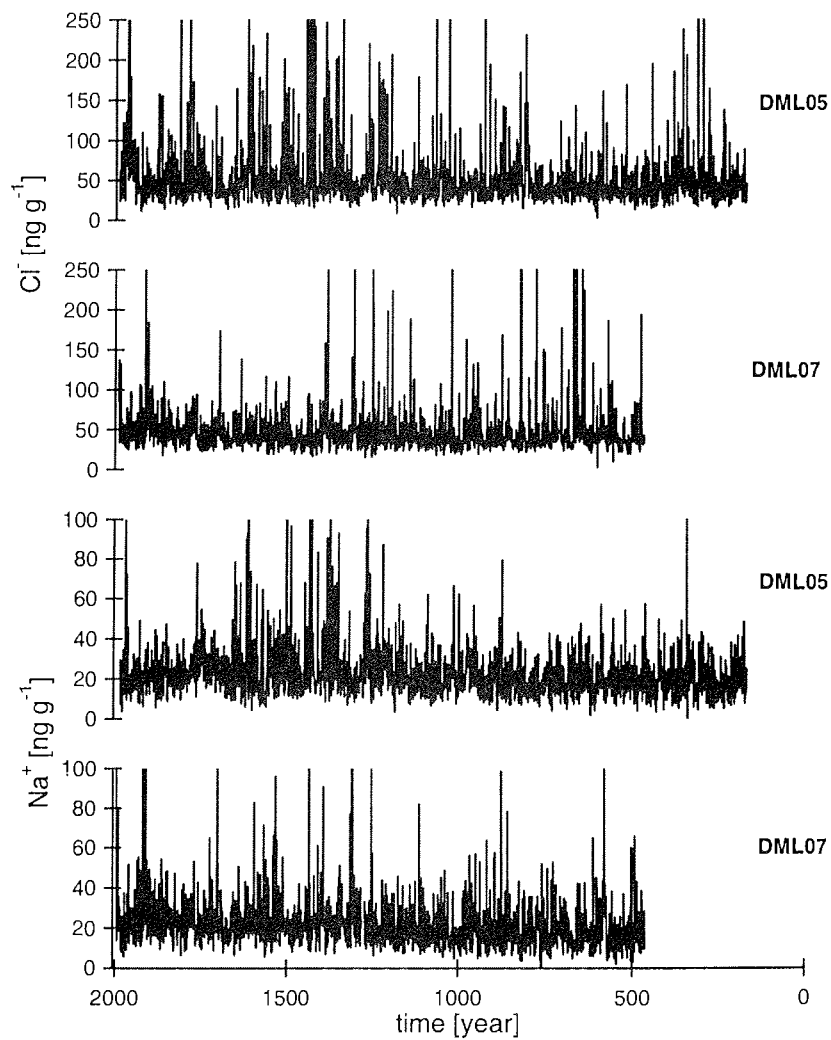


Figure A.4: Annual ion concentrations of chloride and sodium covering the time interval 0 to 1997 A.D..

Annual mean ion concentration records of chloride and sodium at DML03, DML05, DML07 and DML17 plotted versus assigned year.

Appendix B

Spatio-temporal distribution of chemical species

A. Spatio-temporal distribution from 1800 to 1997 A.D.

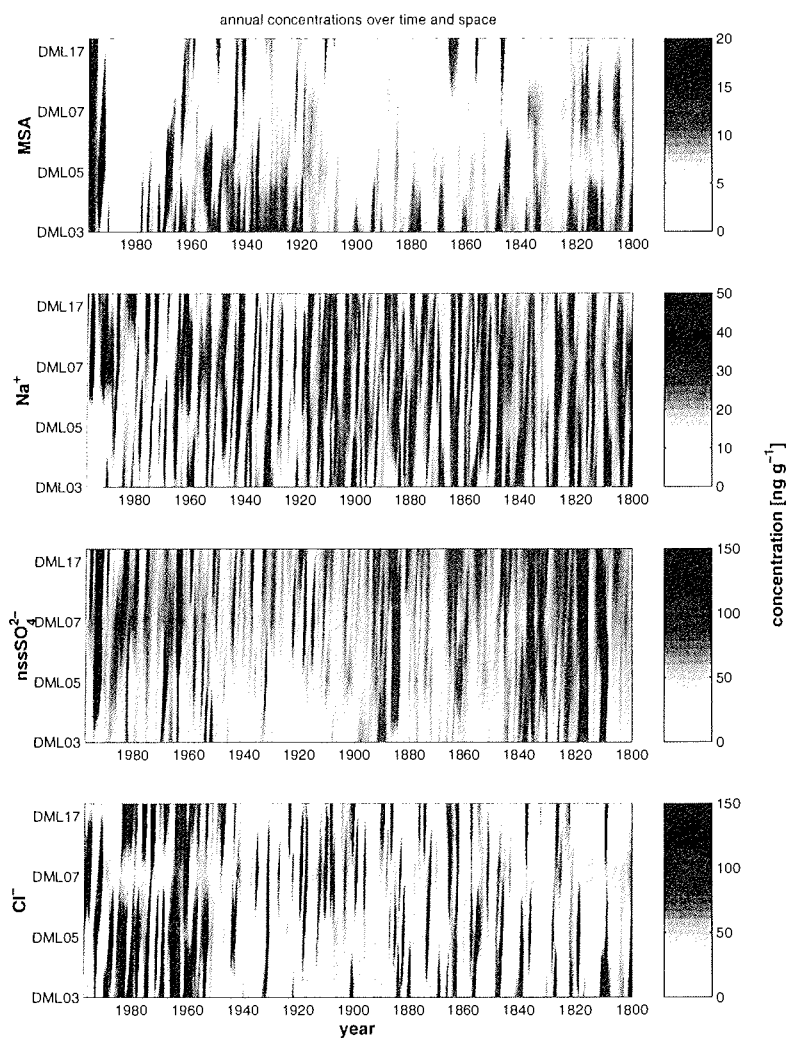


Figure B.1: Spatio-temporal distribution of MSA from 1800 to 1997 A.D.

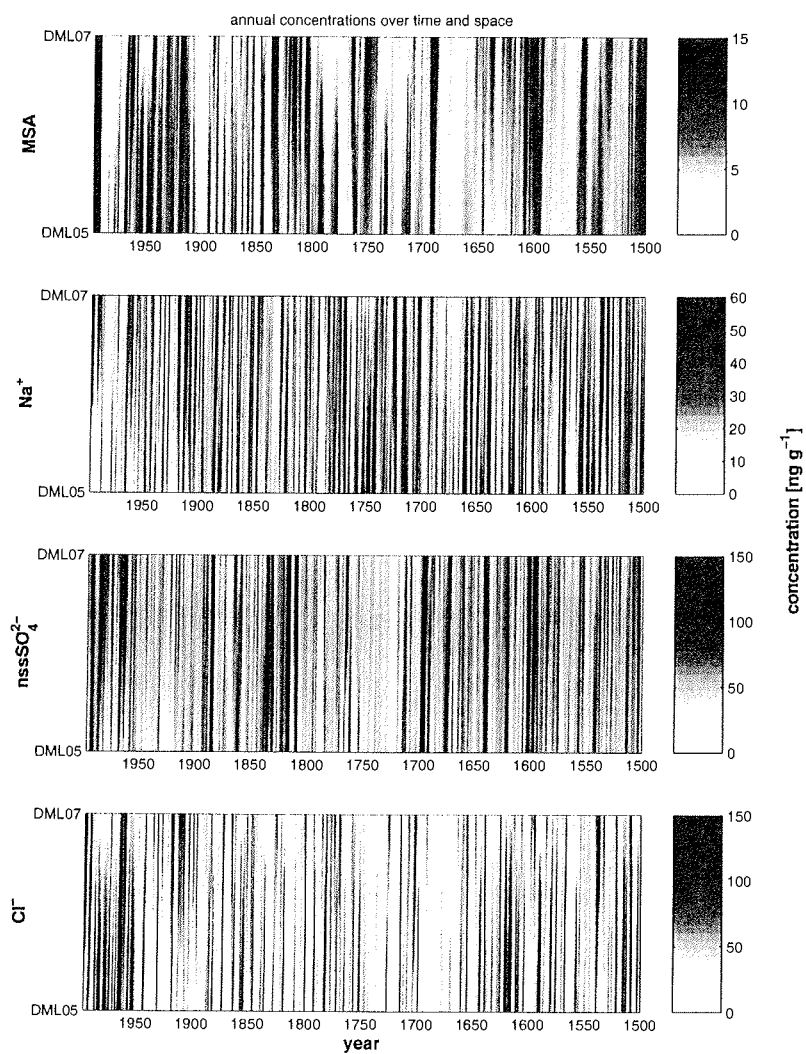
B. Spatio-temporal distribution from 1500 to 1997 A.D.

Figure B.2: Spatio-temporal distribution of MSA from 1500 to 1997 A.D.

C. Spatio-temporal distribution from 500 to 1997 A.D.

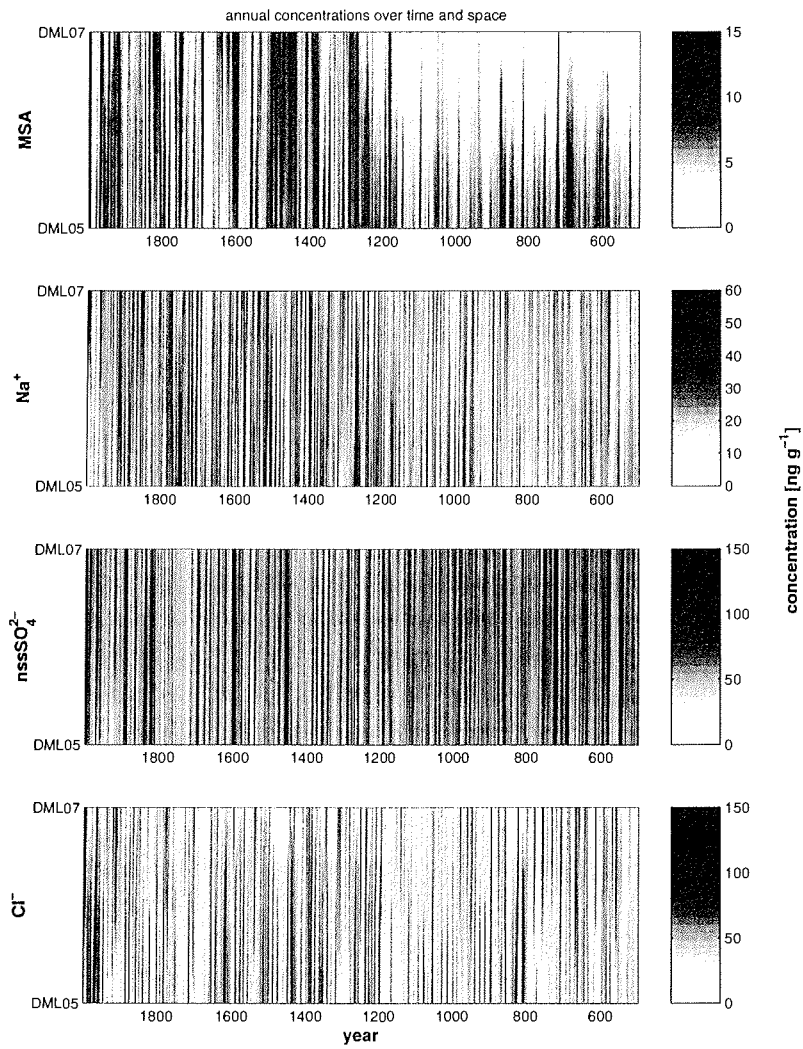


Figure B.3: Spatio-temporal distribution of 500 to 1997 A.D.

Danksagung

Herrn Prof. Miller danke ich für die Ermöglichung und Betreuung dieser Arbeit. Für die Übernahme des Co-Referats danke ich Herrn Prof. Herterich.

Für die Übernahme der Betreuung möchte ich mich bei Dr. Hans Oerter und Dr. Hubertus Fischer bedanken.

Die engagierte Unterstützung durch Hans Oerter, Hubertus Fischer und Rolf Weller hat wesentlich zum Gelingen dieser Arbeit beigetragen. Die Diskussionen mit und Kommentare von Hans Oerter, Rolf Weller, Hubertus Fischer, Frank Kauker und Christopher Zweck haben mir entscheidend weitergeholfen, ebenso die Diskussionen mit Wolfgang Graf (GSF) über stabile Isotope.

Für das Bereitstellen von diversen Skripten danke ich Hubertus Fischer, und Frank Kauker für unermüdliche Diskussionen über Statistik und robuste Ergebnisse.

Thaddäus Bluszcz, Michaela Lelke und Thomas Max danke ich für die exzellente Unterstützung im IC Labor, die zur Durchführung von über 10000 Messläufen wesentlich beitrug.

Den Teilnehmern der NGRIP Kampagne 1999 und von EPICA V in 1999/2000 danke ich für die Zusammenarbeit. Der EPICA III Feldkampagne in 1997/1998 danke ich für den einzigartigen Probensatz, der das Kernstück meiner Arbeit bildete.

Für vielfältige Unterstützung und Hilfe danke ich allen Mitarbeiterinnen und Mitarbeitern der AWI Glaziologie und Luftchemie.

Für die Aufmunterungen und Ermutigungen, sowie die Gespräche über Eis und Schnee, die Antarktis, das Leben und den Rest danke ich Hans Oerter und Rolf Weller.

Bei allen meinen Freunden, insbesondere bei meinem Freund Gerald Traufetter, möchte ich mich für ihre Unterstützung, Verständnis und Geduld bedanken, vor allem in den letzten Wochen und Monaten.

Die finanzielle Unterstützung dieser Arbeit durch die Deutsche Forschungsgemeinschaft (Projekt OE 130/3) sei ausdrücklich dankbar anerkannt.

„Berichte zur Polarforschung“

Eine Titelübersicht der Hefte 1 bis 376 (1981 - 2000) erschien zuletzt im Heft 413 der nachfolgenden Reihe „Berichte zur Polar- und Meeresforschung“. Ein Verzeichnis aller Hefte beider Reihen sowie eine Zusammenstellung der Abstracts in englischer Sprache finden Sie im Internet unter der Adresse: <http://www.awi-bremerhaven.de/Resources/publications.html>

Ab dem Heft-Nr. 377 erscheint die Reihe unter dem Namen:

„Berichte zur Polar- und Meeresforschung“

- Heft-Nr. 377/2000 – „Rekrutierungsmuster ausgewählter Wattfauna nach unterschiedlich strengen Wintern“ von Matthias Strasser
- Heft-Nr. 378/2001 – „Der Transport von Wärme, Wasser und Salz in den Arktischen Ozean“, von Boris Cisewski
- Heft-Nr. 379/2001 – „Analyse hydrographischer Schnitte mit Satellitenaltimetrie“, von Martin Losch
- Heft-Nr. 380/2001 – „Die Expeditionen ANTARKTIS XI/1-2 des Forschungsschiffes POLARSTERN 1998/1999“, herausgegeben von Eberhard Fahrbach und Saad El Naggar.
- Heft-Nr. 381/2001 – „UV-Schutz- und Reparaturmechanismen bei antarktischen Diatomeen und *Phaeocystis antarctica*“, von Lieselotte Riegger.
- Heft-Nr. 382/2001 – „Age determination in polar Crustacea using the autofluorescent pigment lipofuscin“, by Bodil Bluhm.
- Heft-Nr. 383/2001 – „Zeitliche und räumliche Verteilung, Habitatspräferenzen und Populationsdynamik benthischer Copepoda Harpacticoida in der Potter Cove (King George Island, Antarktis)“, von Gritta Veit-Köhler.
- Heft-Nr. 384/2001 – „Beiträge aus geophysikalischen Messungen in Dronning Maud Land, Antarktis, zur Auffindung eines optimalen Bohrpunktes für eine Eiskerntiefbohrung“, von Daniel Steinhage.
- Heft-Nr. 385/2001 – „Actinium-227 als Tracer für Advektion und Mischung in der Tiefsee“, von Walter Geibert.
- Heft-Nr. 386/2001 – „Messung von optischen Eigenschaften troposphärischer Aerosole in der Arktis“ von Rolf Schumacher.
- Heft-Nr. 387/2001 – „Bestimmung des Ozonabbaus in der arktischen und subarktischen Stratosphäre“, von Astrid Schulz.
- Heft-Nr. 388/2001 – „Russian-German Cooperation SYSTEM LAPTEV SEA 2000: The Expedition LENA 2000“, edited by Volker Rachold and Mikhail N. Grigoriev.
- Heft-Nr. 389/2001 – „The Expeditions ARKTIS XVI/1 and ARKTIS XVI/2 of the Research Vessel 'Polarstern' in 2000“, edited by Gunther Krause and Ursula Schauer.
- Heft-Nr. 390/2001 – „Late Quaternary climate variations recorded in North Atlantic deep-sea ostracodes“, by Claudia Didié.
- Heft-Nr. 391/2001 – „The polar and subpolar North Atlantic during the last five glacial-interglacial cycles“, by Jan. P. Helmke.
- Heft-Nr. 392/2000 – „Geochemische Untersuchungen an hydrothermal beeinflussten Sedimenten der Bransfield Straße (Antarktis)“, von Anke Dähmann.
- Heft-Nr. 393/2001 – „The German-Russian Project on Siberian River Run-off (SIRRO): Scientific Cruise Report of the Kara-Sea Expedition 'SIRRO 2000' of RV 'Boris Petrov' and first results“, edited by Ruediger Stein and Oleg Stepanets.
- Heft-Nr. 394/2001 – „Untersuchung der Photooxidantien Wasserstoffperoxid, Methylhydroperoxid und Formaldehyd in der Troposphäre der Antarktis“, von Katja Riedel.
- Heft-Nr. 395/2001 – „Role of benthic cnidarians in the energy transfer processes in the Southern Ocean marine ecosystem (Antarctica)“, by Covadonga Orejas Saco del Valle.
- Heft-Nr. 396/2001 – „Biogeochemistry of Dissolved Carbohydrates in the Arctic“, by Ralph Engbrodt.
- Heft-Nr. 397/2001 – „Seasonality of marine algae and grazers of an Antarctic rocky intertidal, with emphasis on the role of the limpet *Nacilla concinna* Strebel (Gastropoda: Patellidae)“, by Dohong Kim.
- Heft-Nr. 398/2001 – „Polare Stratosphärenwolken und mesoskalige Dynamik am Polarwirbelrand“, von Marion Müller.
- Heft-Nr. 399/2001 – „North Atlantic Deep Water and Antarctic Bottom Water: Their Interaction and Influence on Modes of the Global Ocean Circulation“, by Holger Brix.
- Heft-Nr. 400/2001 – „The Expeditions ANTARKTIS XVIII/1-2 of the Research Vessel 'Polarstern' in 2000“ edited by Victor Smetacek, Ulrich Bathmann, Saad El Naggar.
- Heft-Nr. 401/2001 – „Variabilität von CH₂O (Formaldehyd) - untersucht mit Hilfe der solaren Absorptionsspektroskopie und Modellen“ von Torsten Albrecht.
- Heft-Nr. 402/2001 – „The Expedition ANTARKTIS XVII/3 (EASIZ III) of RV 'Polarstern' in 2000“, edited by Wolf E. Arntz and Thomas Brey.
- Heft-Nr. 403/2001 – „Mikrohabitatansprüche benthischer Foraminiferen in Sedimenten des Südatlantiks“, von Stefanie Schumacher.
- Heft-Nr. 404/2002 – „Die Expedition ANTARKTIS XVII/2 des Forschungsschiffes 'Polarstern' 2000“, herausgegeben von Jörn Thiede und Hans Oerter.
- Heft-Nr. 405/2002 – „Feeding Ecology of the Arctic Ice-Amphipod *Gammarus wilkitzkii*. Physiological, Morphological and Ecological Studies“, by Carolin E. Arndt.
- Heft-Nr. 406/2002 – „Radiolarienfauna im Ochotskischen Meer - eine aktuopaläontologische Charakterisierung der Biozönose und Taphozönose“, von Anja Nimmergut.
- Heft-Nr. 407/2002 – „The Expedition ANTARKTIS XVIII/5b of the Research Vessel 'Polarstern' in 2001“, edited by Ulrich Bathmann.
- Heft-Nr. 408/2002 – „Siedlungsmuster und Wechselbeziehungen von Seepocken (Cirripedia) auf Muschelbänken

(*Mytilus edulis* L.) im Wattenmeer", von Christian Buschbaum.

Heft-Nr. 409/2002 – „Zur Ökologie von Schmelzwassertümpeln auf arktischem Meereis - Charakteristika, saisonale Dynamik und Vergleich mit anderen aquatischen Lebensräumen polarer Regionen“, von Marina Carstens.

Heft-Nr. 410/2002 – „Impuls- und Wärmeaustausch zwischen der Atmosphäre und dem eisbedeckten Ozean“, von Thomas Garbrecht.

Heft-Nr. 411/2002 – „Messung und Charakterisierung laminarer Ozonstrukturen in der polaren Stratosphäre“, von Petra Wahl.

Heft-Nr. 412/2002 – „Open Ocean Aquaculture und Offshore Windparks. Eine Machbarkeitsstudie über die multifunktionale Nutzung von Offshore-Windparks und Offshore-Markultur im Raum Nordsee“, von Bela Hieronymus Buck.

Heft-Nr. 413/2002 – „Arctic Coastal Dynamics. Report of an International Workshop. Potsdam (Germany) 26-30 November 2001“, edited by Volker Rachold, Jerry Brown and Steve Solomon.

Heft-Nr. 414/2002 – „Entwicklung und Anwendung eines Laserablations-ICP-MS-Verfahrens zur Multielementanalyse von atmosphärischen Einträgen in Eisbohrkernen“, von Heiko Reinhardt.

Heft-Nr. 415/2002 – „Gefrier- und Tauprozesse im sibirischen Permafrost – Untersuchungsmethoden und ökologische Bedeutung“, von Wiebke Müller-Lupp.

Heft-Nr. 416/2002 – „Natürliche Klimavariationen der Arktis in einem regionalen hochauflösenden Atmosphärenmodell“, von Wolfgang Dorn.

Heft-Nr. 417/2002 – „Ecological comparison of two sandy shores with different wave energy and morphodynamics in the North Sea“, by Iris Menn.

Heft-Nr. 418/2002 – „Numerische Modellierung turbulenter Umströmungen von Gebäuden“, von Simón Domingo López.

Heft-Nr. 419/2002 – „Scientific Cruise Report of the Kara-Sea Expedition 2001 of RV „Academic Petrov“: The German-Russian Project on Siberian River Run-off (SIRRO) and the Project „ESTABLISH“, edited by Ruediger Stein and Oleg Stepanets.

Heft-Nr. 420/2002 – „Vulkanologie und Geochemie pliozäner bis rezenter Vulkanite beiderseits der Bransfield-Straße / West-Antarktis“, von Andreas Veit.

Heft-Nr. 421/2002 – „POLARSTERN ARKTIS XVII/2 Cruise Report: AMORE 2001 (Arctic Mid-Ocean Ridge Expedition)“, by J. Thiede et al.

Heft-Nr. 422/2002 – „The Expedition „AWI of RV „L'Atalante“ in 2001“, edited by Michael Klages, Benoit Mesnil, Thomas Soltwedel and Alain Christophe with contributions of the participants.

Heft-Nr. 423/2002 – „Über die Tiefenwasserausbreitung im Weddellmeer und in der Scotia-Sea: Numerische Untersuchungen der Transport- und Austauschprozesse in der Weddell-Scotia-Konfluenz-Zone“, von Michael Schodlok.

Heft-Nr. 424/2002 – „Short- and Long-Term Environmental Changes in the Laptev Sea (Siberian Arctic) During the Holocene“, von Thomas Müller-Lupp.

Heft-Nr. 425/2002 – „Characterisation of glacio-chemical and glacio-meteorological parameters of Amundsenisen, Dronning Maud Land, Antarctica“, by Fidan Göktas.

* vergriffen/out of print.

** nur noch beim Autor/only from the author.

